COMPLIANT DIRECTIONAL SUSPENSIONS FOR CLIMBING WITH SPINES AND ADHESIVES

A DISSERTATION
SUBMITTED TO THE DEPARTMENT OF ELECTRICAL ENGINEERING
AND THE COMMITTEE ON GRADUATE STUDIES
OF STANFORD UNIVERSITY
IN PARTIAL FULFILLMENT OF THE REQUIREMENTS
FOR THE DEGREE OF
DOCTOR OF PHILOSOPHY

Alan T. Asbeck
March 2010

Abstract

Climbing rough vertical surfaces can be useful for applications such as search-and-rescue, surveillance, and the inspection of hard-to-reach locations. In nature, several methods of adhering to vertical surfaces can be observed. Small non-penetrating spines are used effectively by many insects to attach to rough surfaces such as rock, concrete, and similar materials. These structures hook onto surface asperities to provide adhesion.

In this thesis, we discuss synthetic arrays of microspines that can be used by robots or humans to attach to rough vertical surfaces. Microspine arrays have the advantages of requiring low preloads, functioning in wet and dusty environments, and supporting loads for extended periods of time without consuming power. Moreover, they can attach to surfaces that are too rough for current synthetic dry adhesives.

We discuss the properties of surfaces that make them suitable for use with spines, and present a spine/surface interaction model. We then discuss properties of the spine suspensions necessary for them to be used effectively. The suspensions must permit the spines to conform to the surface, share loads between them, and engage and disengage from the surface. We present spine suspensions that were constructed, and show that they have good measured performance in comparison to ideal designs. We show examples of how spines have been used on climbing robots and in human climbing aids.

We also show that the requirements for directional adhesive materials to work on any surfaces are similar to those of spines, and that the principles developed for large spine arrays can be adapted to directional dry adhesives for climbing. We discuss

requirements on suspensions for large patches of spines or dry adhesives to enable load-sharing over large areas.

Acknowledgments

I am very grateful for the help and support of a large number of people, without which this would not have been possible. First, I would like to thank my adviser Prof. Mark Cutkosky, for his assistance and guidance in innumerable ways. I have only begun to appreciate the full extent of how much I have learned from him. Many thanks are also due to the rest of my committee, Prof. Krishna Shenoy and Prof. Andrew Ng. I am so very grateful to all of my labmates in the BDML—you make lab a really fun place to be. One of the primary reasons I have had such a great time in grad school is because of you all. I also want to thank my friends from a number of groups who have made grad school a great experience outside of lab: my EE friends, my friends from CroMem, and everyone in Chi Alpha Christian Fellowship and our pastor Glen Davis. I am very grateful for your friendship and that you have been a part of my life. I want to also thank my parents and sister for their constant love and support, and for being awesome. My parents have always encouraged us to pursue whatever we wanted, provided for us the best opportunities that they could, and have been really good parents on the whole. Last but not least, I want to thank God for sustaining me and providing for me in so many ways.

Contents

List of Tables

List of Figures

Chapter 1

Introduction

1.1 Overview

In recent years, there has been considerable progress in small, legged robots that can run rapidly and stably over rough terrain [92, 16, 85, 30]. Climbing and maneuvering on vertical surfaces presents a more difficult challenge, one that robots are just beginning to address. Small robots that can climb a variety of hard and soft surfaces unobtrusively and cling for extended periods of time without high power consumption would be beneficial for applications such as surveillance or the inspection of hard-to-reach locations.

Previously developed climbing robots have generally employed suction [59, 60, 113], magnets [11, 109, 45, 108, 50, 95, 39, 40, 43] or adhesives [70, 21, 22, 24, 73, 103, 102] to cling to smooth vertical surfaces such as windows and interior walls. None of these approaches is suitable for porous or dusty exterior surfaces such as brick, concrete, stucco or stone. Other climbing robots employ hand and foot holds in the manner of a human climber [12, 14]. A controlled vortex to create negative aerodynamic lift has been demonstrated on brick and concrete walls with considerable success [104, 106, 107]. However, this approach consumes significant power (including when the robot is stationary), unavoidably generates noise and is more difficult to adapt to non-flat surfaces such as window ledges and corners. A recent development,

electroadhesion, uses high voltage to cause a flexible film to electrostatically cling to a variety of surfaces [83].

When we look at animals that exhibit agility on vertical surfaces, we find a variety of methods employed [15]. Larger animals such as cats and raccoons have strong claws that can penetrate wood and bark surfaces. Tree frogs and many insects employ sticky pads [27, 28]. Geckos and some spiders utilize large numbers of very fine hairs that achieve adhesion via *van der Waals* forces on almost any kind of surface [9, 53, 1]. Insects and arthropods that climb well on vertical surfaces often have legs equipped with large numbers of small, sharp spines [19]. At a larger scale, geckos that frequent rock surfaces such as cliffs and caves have small claws on each toe in addition to their dry adhesive structures [111]. Unlike the larger claws of a cat, spines do not need to penetrate surfaces. Instead, they engage small surface asperities.

Spines and dry adhesives are both of particular interest because, together, they work on a wide range of surfaces and they permit attachment and detachment rapidly and with low energy expenditure. Dry adhesives work best on relatively smooth surfaces, while spines can be used for adhesion on rough surfaces.

1.2 Dry adhesives

1.2.1 The gecko adhesive system

A discussion of the gecko adhesive system is warranted because it shares many similarities with the microspine arrays developed in this thesis. Geckos can cling to a wide range of surfaces, from smooth glass to sandstone. They accomplish this through a dry adhesive and hierarchical structures in their feet that accomplish load-sharing. The feet contain lamellae, flaps of skin covered with small hair-like structures called setae. The setae branch into a tree-like structure at their ends, with the smallest features around 150-175nm in diameter [86, 5]. These branched ends stick to surfaces via *van der Waals* forces, which may be supplemented by capillary forces in the presence of humidity [7, 10, 44, 101, 76].

Aside from clinging extremely well to a very wide range of surfaces, the gecko adhesive system has a number of useful properties:

- *It is directional.* The amount of adhesive force in the direction normal to the surface is proportional to the amount of applied shear force parallel to the surface. This is useful for control, because the amount of stickiness can be changed by applying different amounts of shear force. Figure 1.1 shows a plot of the force generated by gecko setae [6], in comparison with two other models which express forces between two elastic spheres (B, the Johnson-Kendall-Roberts (JKR) model [49]) and an adhesive tape (C, the Kendall Peel model [52]). The directional property can be seen with the straight line from the origin through force-space. These plots show a shaded "safe" region, in which contact will be maintained, as long as forces are kept within that region of force-space.

- *It requires zero pull-off force.* If the shear force on the setae is reduced to zero, or the setae are moved along the surface in their non-preferred direction, the setae lose their adhesion. In contrast, for example, most adhesive tapes require a peeling force to disengage from surfaces. When these adhesives detach completely, there will be a sudden jump in force as the adhesive comes un-stuck. Having zero pull-off force is extremely useful in climbing applications, because detachment can then be done smoothly, without shaking the robot from sudden force impulses. Furthermore, any force required to peel the adhesive is wasted energy.

- *It requires low preloads and can generate large forces.* A single setal stalk can hold 194 μN in adhesion, or 48 kPa (= 4.8 kg/cm^2) [8, 36]. To achieve these large forces, the setae only must be preloaded lightly into the surface: the ratio of adhesion:preload force, known as μ', is 8-16 for a single seta [8].

- *It is reusable and self-cleaning.* The gecko's setae can be used for thousands of steps before degrading, at which point the gecko must molt to expose a fresh layer of adhesive [35]. The structure of the setae is such that dirt particles naturally fall off after a few steps, because it is energetically more favorable for

them to stick to the substrate than the setae [41]. In contrast, most adhesive tapes get dirty after only a single use.

Many of these properties are also true of the microspine arrays developed in this thesis: microspines are directional, require zero or near-zero pull-off force, can generate large forces after only small preloads, and are reusable and resistant to fouling.

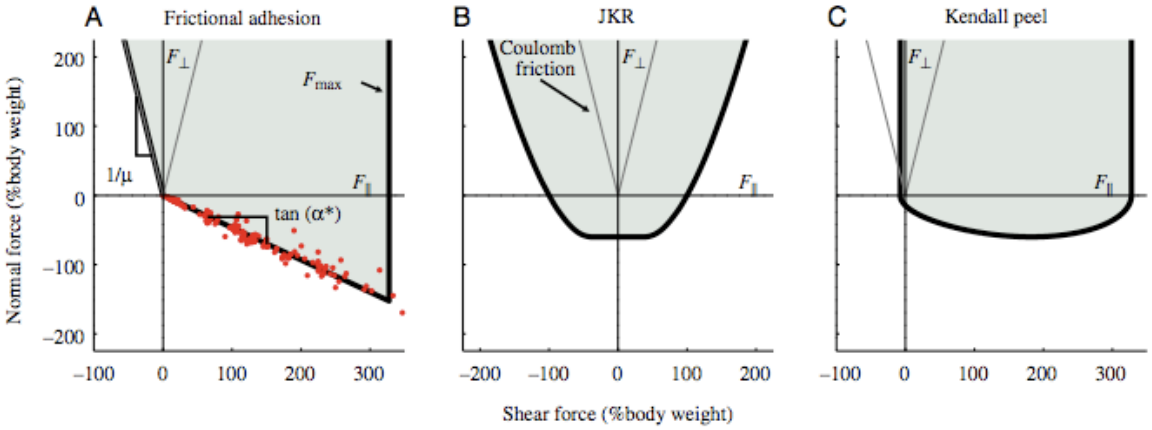

Figure 1.1: (A), the frictional adhesion model of gecko setae. Gecko setae provide adhesion normal to the surface in proportion to the applied shear force, up to a limit F_{max}. The forces pass through the origin, providing easy detachment. (B), the Johnson-Kendall-Roberts model is for contact between two elastic spheres, and includes the effects of *van der Waals* forces. (C), the Kendall Peel model describes adhesion due to peeling, e.g. adhesive tape. Both of these other models require a jump in force when detaching because the limit curves do not intersect the origin. (Fig. from Autumn et al. [6].)

1.2.2 Synthetic dry adhesives

Due to the many useful properties of the gecko setae, synthetic dry adhesives imitating gecko setae are being developed by several laboratories and there is a rapidly growing literature on the subject. Dry adhesives have been made from polyimide hairs [32], polystyrene shaped with a mold [46, 110], carbon nanotubes [112, 31, 84], polypropylene molded into hairs [67, 63, 47], polyvinylsiloxane [20, 23, 33], or polyurethane rubber [91, 54, 56, 57, 74]. These are made as patches of hairs or stalks attached to a

backing layer, with the terminal features ranging in size from sub-micron to hundreds of microns. Some groups have made hierarchical adhesives, with small hairs or stalks on the ends of larger stalks or suspensions [77, 72, 2, 62].

In general, different synthetic dry adhesives excel in different respects, though none excels in all of the ways the gecko adhesive system does [81]. Some sythetic dry adhesives have been demonstrated to hold large adhesive pressures: [72, 84, 33] have adhesive pressures of >35 kPa (compare to the gecko's 48 kPa), though with patch sizes of only 0.16 cm^2 or less. Some adhesives have a large value of μ', the ratio of adhesive pressure to preload: [33, 91, 93] have values comparable to the gecko's. A few can be used in large patch sizes [81, 2, 91, 47, 93], and these also happen to be directional.

Currently, all synthetic dry adhesives lack the self-cleaning property that allows geckos to climb dusty walls, meaning that they can only be used in environments with little dust or dirt. They also currently work only on relatively smooth surfaces, such as painted metal or interior drywall, though progress is continuing. In general, few of the synthetic adhesives are currently suitable for robotic climbing (as discussed in [81]), and, as is discussed in *this* thesis, none of them can be used for climbing without a properly designed suspension for distributing loads.

1.3 Spines

1.3.1 Spines in nature

A wide variety of animals use non-penetrating spines or claws to adhere to surfaces or provide increased traction. These range in size from small insects to large mammals.

Many insect species such as ants, bees, and beetles use small claws at the end of each leg to generate adhesion [75, 34, 65].

Roth and Willis [89] note that *P. americana* cockroaches can walk vertically and even inverted on rough filter paper and rough emery paper surfaces, using only the tarsal claws at the ends of their feet after their arolia (which stick to smooth surfaces

on *P. americana*) were removed. The cockroaches were not able to adhere to smoother grades of emery paper, however. Larsen et al. show how cockroaches actively engage and disengage their claws with each step while walking upright and while walking inverted on meshes [61, 29]. Dai et al. studied the increased frictional forces generated by beetles on rough surfaces due to the interaction of their claws with the substrate [19].

Cockroaches and spiders also use spines along the length of their legs to generate increased traction on surfaces, particularly on their rear legs [98, 89]. These spines function somewhat differently than claws for adhesion in that positive normal forces are applied during their use. Spagna et al. studied how spines on the legs significantly improve locomotion on surfaces like meshes, where footholds are sparse [98]. The study also discussed how control is simpler if the feet are not sensitive to precise placement on the surface.

Lizards also use their claws to attach to asperities on non-penetrable surfaces. Zani found that the ability of lizards to cling to rough surfaces was correlated with increased claw height and shorter toe length [111]. Mahendra found that geckos, which have both dry adhesives and claws on the end of each toe, depend on their claws to cling to very rough surfaces [66]; if the claws were removed, it was very difficult or impossible for the geckos to stay attached.

Squirrels can also climb a range of impenetrable surfaces such as brick, stucco, and surfaces with embedded rocks, as can be seen in figure 1.2(right) ([26], personal observations). Even large animals such as bears are aided by the roughness of tree bark to gain a grip. Black bear cubs have a much easier time climbing white pines than other trees, due to the white pines' furrowed and strong bark [87].

Of note, many animals have only a small number of claws on each foot. Insects generally have two on the end of each leg, while mammals have four or five. Birds may have two claws pointing in each direction, and *Dendrocopos minor* woodpeckers can rotate their toes so three of them face upwards and one to the side. The feet are used to grip a tree while the tail prevents pitchback [13]. We expect that with the relatively constant number of claws or spines per foot, that claw or spine size should

Figure 1.2: Pictures of a cockroach (left) and a squirrel (right) using spines to climb vertical surfaces (Left picture used with permission from Robert Full).

increase with the animal's mass, to withstand forces that will be proportional to the animal's body weight. (A further discussion of spine scaling is in section 2.3). In contrast, our synthetic microspine arrays decouple the spine size from the total load carried by having large numbers of small spines.

1.3.2 Synthetic spine arrays

Synthetic spine arrays for climbing are a new development by the author and colleagues [3, 4, 55]. Although spines are limited to being used on relatively rough surfaces, they are particularly attractive for hard, dusty, exterior surfaces because they are relatively unaffected by dirt and only moderately affected by moisture. They have a very low energy of attachment and negligible energy of detachment.

Spines have been used by the author and colleagues on robots to climb vertical surfaces including cinder block, concrete, brick, stucco, and surfaces with small embedded rocks. Furthermore, spines function well on penetrable surfaces such as felt and cloth.

Others, in recent work, have had some success with spines, with robots able to

climb surfaces at 60° angles [24]. Other robots have used penetrating claws [42], but these function differently than microspines, which typically do not penetrate the surface.

While limited to rough surfaces, synthetic microspine arrays are extremely useful for robotic climbing, human climbing, and airplane perching. Their analysis further aids development of dry adhesive patches to be used on smooth surfaces. In the same way that geckos need claws to engage on rough surfaces [66], spines used in conjunction with dry adhesives show great promise for attaching to a wide range of surfaces.

1.4 Thesis outline

Chapter 2 presents a model of how spines engage on surfaces. Analysis is performed on measured surfaces, determining the frequency of asperities and how the number of asperities and spine/asperity contact strength scale with spine size.

Chapter 3 presents stages of use for the spines, from engagement to disengagement. In each stage, constraints on the spine suspension stiffness matrix are presented so that spines can be practically usable. The ideal spine suspension for load-sharing is presented, subject to certain assumptions.

Chapter 4 presents several spine suspensions that have been manufactured and used in robot and human climbing applications. The spine suspensions are characterized and compared, and the performance of spines on a tarpaper (roofing paper) surface is measured. A model of a typical spine suspension is used to evaluate the effects of varying parameters in the suspension.

Chapter 5 discusses constraints on supporting structures for large patches of spines or dry adhesives.

Chapter 6 concludes the thesis and offers suggestions for future work.

1.5 Contributions

The main contributions of this thesis are as follows:

- a spine/surface interaction model that predicts when spines will find asperities and when contacts will fail,
- a formulation of constraints on spine suspensions, including ideal behavior under certain assumptions,
- analysis and empirical validation of arrays of microspines used for robot and human climbing,
- definition of requirements on dry adhesive patches to enable conformation and load-sharing.

Chapter 2

Spine-surface interactions

2.1 Overview

A few studies in the biology literature have considered the problem of spine/surface interaction. Dai et al. [19] present a planar model of spine/asperity contact and compute the maximum load per spine as a function of spine strength, relative size of the spine tip versus that of an asperity, and coefficient of friction. As expected, for rough surfaces the mechanical strengths of the spine and asperity become the limiting factors; for smoother surfaces friction is more important, and the ability to pull along the surface is much reduced.

Given the general correlation in nature between spine or claw size and animal size, we ask: for a climbing robot of a certain size, how large should the spines be? For a 0.4 Kg robot we might expect spines or claws similar to those seen in squirrels or large climbing lizards. However, this argument ignores the point that spines of hardened steel are much stronger and stiffer than their natural counterparts. If the strength of the spine/asperity contact were not a constraint, the spines should be as small as possible. This is because many natural surfaces, and some man-made surfaces such as concrete and stucco, have an approximately fractal surface topography [17, 37, 38] so that characteristic surface features (asperities) can be found over a wide range of length scales.

In the following sections we first investigate the question of spine/asperity scaling using surface profiles obtained for various materials. The results show that while surfaces do, in general, present more asperities per unit area as spine size shrinks, the details of the spine approach angle and the surface topography play an important role. We next consider the question of spine/asperity contact strength. There are several possible failure modes. In general, however, the expected maximum load increases as the square of overall spine size. We conclude with a model in force-space of the forces a spine-asperity contact can sustain.

2.2 Spine/surface modeling and scaling

Numerical simulations were performed to model the behavior of spines interacting with surfaces. In general, the simulations fitted 2-D spine cross-sections to 2-D surface profiles and determined the locations where the simulated spine could perch on the profile. This analysis gives insight into what size spines are needed to climb various surfaces and the properties of a surface that make it climbable. This is a geometric analysis, indicating trends in the number of asperities (perchable regions) per unit length of surface. Spine and surface strength are also important considerations and are addressed in section 2.3 and Appendix A.1.

Two-dimensional profiles of several stone and sandpaper surfaces were obtained using a profilometer (Taylor Hobson Talysurf Series 2), with a conical stylus (15° cone angle) terminating in a spherical tip of radius 2 μm. Profiles of rougher concrete surfaces were measured using a laser micrometer (Omron Z4M-N30V), since the profilometer could not measure very rough surfaces. The measured profiles were 5 cm long. The profilometer had a vertical resolution 0.426 μm and samples were taken every 1 μm; the laser micrometer had a spot size 64 μm, a vertical resolution of 0.977 μm, and samples were taken every 2.4 μm.

In analyzing these profiles we consider a typical spine as shown in the photograph in figure 2.1. The spine is a gently curved beam with a circular cross section that tapers to a rounded tip of radius r_s. The spine is attached to a robot limb that

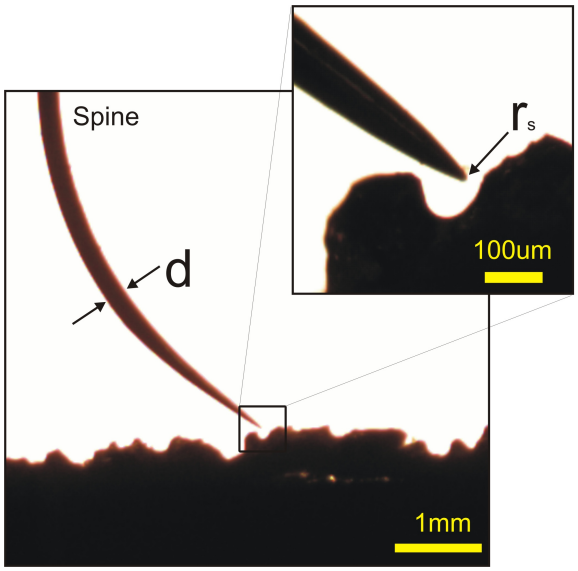

Figure 2.1: Profile photograph of typical spine, with shaft dia., $d = 270\mu m$ and tip radius $r_s = 10\mu m$, engaging a profile of a rough concrete surface.

drives it toward the surface and subsequently strokes it downward (left to right in the figure) along the surface, hoping to engage an asperity. In the simulation, we model the spine tip as a circle of radius r_s approaching the surface at an angle θ_a.

In figure 2.2, a diagram of our model, a circle of radius r_s has approached the surface in a direction indicated by the *approach vector*. The surface shown in the figure is an actual profile of a rough-cut granite surface.

We create a *spine swept volume* from the spine tip circle, bounded at the upper edge by the angle θ_a and at the lower edge by a ray perpendicular to the surface face. A *traced surface* [79, 88] is formed by moving the spine swept volume over the profile and recording the position of the center of the spine tip circle. We assume that the details of the spine, including a conical spine end and the spine curvature, fall within the swept volume. Thus, the spine swept volume accounts for the fact that an actual spine is not be able to reach all parts of the surface (e.g. the bottoms of deep pits) if it moves towards the surface at an angle or if it is oriented at an angle as it slides over the surface.

To find regions of the surface that a spine could perch on (i.e., asperities), we

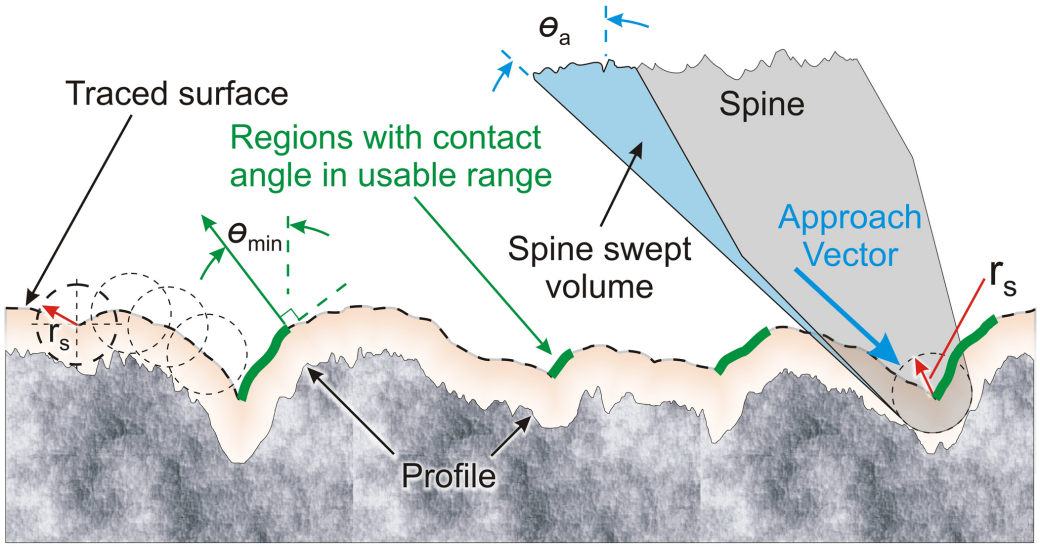

Figure 2.2: Diagram of the spine/surface interaction model. The spine is modeled by a circle of radius r_s approaching in a direction indicated by the approach vector, which creates a swept volume. The intersection of the swept volume and the original profile is found and the center of the spine tip circle is recorded to create a traced surface. Contiguous shelf-like regions, starting when θ, the normal vector to the traced surface, is larger than some critical angle θ_{min}, are available for sustaining loads.

proceed along the traced surface from right to left in figure 2.2. We search for locations in which the angle θ of the normal vector to the traced surface is above a minimum useable angle, θ_{min}, which depends on the angle at which the spines are loaded, θ_{load}, and coefficient of friction, μ, as seen in equations 2.1 and 2.2:

$$\theta_{max} = \theta_{min} - \arctan(1/\mu) \qquad \text{where} \tag{2.1}$$

$$\theta_{load} \leq \theta_{max}. \tag{2.2}$$

We consider regions between these locations and the subsequent minimum in the traced surface to be "useable asperities," as shown in figure 2.2. In essence, we find "shelves" that are terminated by an angle θ_{min} near regions of maximum projection from the wall surface. We assume that the spine slides quasi-statically along the surface from the top down. If the spine tip falls into any of the "useable asperity"

regions, it will continue to move along the surface until it reaches the point at which the normal vector to the traced surface is at the angle θ_{min}, and at that location the spine will stop and catch on the surface. The spine can then be loaded away from the wall (i.e., used to generate adhesion) at an angle up to θ_{max} before it begins to slip off the asperity. For a given Root-Mean-Square (RMS) surface roughness, R_q, the useable asperity regions can vary greatly, depending on the details of the profile. This purely geometric analysis does not account for spine bouncing or other dynamic effects; however, as discussed in the next section, it provides useful predictions of the comparative ease with which surfaces of varying roughness and asperity sharpness can be climbed.

We use the number of asperities per centimeter as a metric rather than other measures such as the effective length of the asperities because the former is a better indication of the probability that a spine will encounter an asperity during a stroke of a given length. (For example, a single long asperity would be equivalent to many short asperities in terms of effective asperity length.) A more accurate assessment would include complete information about the probability distribution of asperities and asperity lengths on the wall.

This analysis is somewhat limited, being strictly two-dimensional in the direction of motion along a surface. In practice, a spine will have the ability to move slightly sideways as it is dragged down a surface, and asperties are three dimensional features. Asperities will, in general, have a slope in the out-of-plane direction, which may cause a spine to slide off in that direction. Thus, the actual number of asperities per unit length will be somewhat less than indicated by this analysis.

A conservative estimate of the magnitude of this effect occurs if we analyze a surface with protruding right rectangular cylinders. On such a surface, the entire width of each cylinder will appear to support spines in a 2-D analysis, but in 3-D, spines landing on the edges of the cylinders will just slip off to the side. With a coefficient of friction of 0.2, only 20% of the cylinder's top face has a normal vector that can support a spine loaded vertically down the surface. This is a conservative estimate because first, the profilometer itself was able to move out-of-plane to a small

extent, so it could slide off similarly sharp features. The laser micrometer underwent some low-pass filtering due to the finite spot size, which would also reduce the effect. Second, surfaces in nature will rarely have such sharp features, and smoother surfaces will have a larger correlation between the slopes in the two directions. Finally, some surfaces will have pits instead of protrusions, and pits will tend to steer the spines into more favorable resting places.

2.2.1 Simulation results

Table 2.1: Table of Surfaces and Roughness Parameters

Surf. No.	Surface	Average Roughness R_a (μm)	RMS Roughness R_q (μm)	Fractal Dimension D
1	cobblestone	56.9	78.1	1.2
2	machined granite	6.6	10.3	1.4
3	rough cut granite	42.7	56.1	1.4
4	polished granite	13.2	21.0	1.3
5	paving stone	73.0	92.2	1.2
6	concrete cinderblock	93.0	131.9	1.1
7	concrete 2	70.1	88.4	1.0
8	Al-oxide 80	42.1	57.0	1.1
9	Al-oxide 100	35.8	49.9	1.1
10	Al-oxide 120	20.3	26.0	1.1
11	Al-oxide 150	21.7	27.8	1.1
12	Painter's 100	30.5	38.9	1.0

Profiles were taken for several stone surfaces and several types of sandpaper, listed in table 2.1. The table also shows the linear and RMS roughness measures R_a and R_q (see Appendix A.3) for these surfaces, as well as the fractal dimension measured using the power spectral density [82]. Figure 2.3 shows typical results for the number of asperities per centimeter for selected stone and sandpaper surfaces, with constant

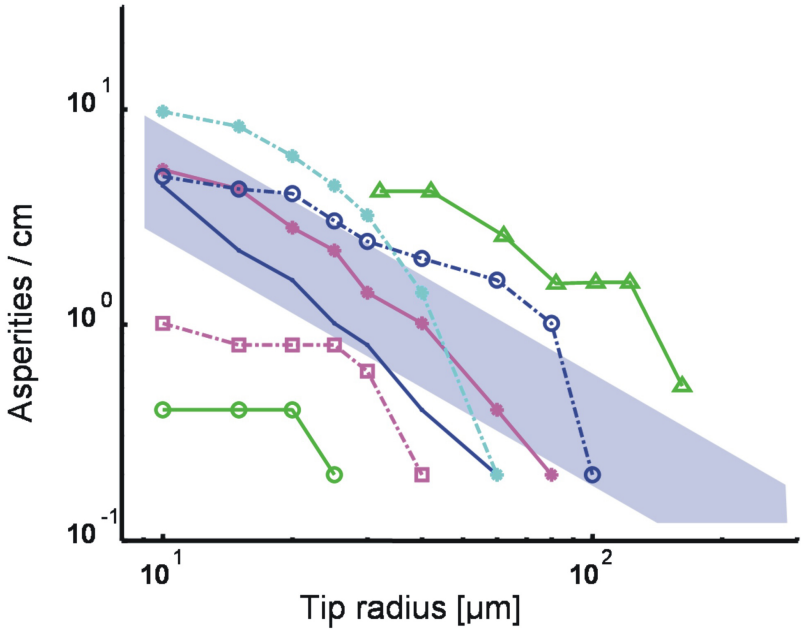

Figure 2.3: Number of asperities per centimeter versus spine tip radius for various surfaces, with $\theta_a = 45°$ and $\theta_{min} = 75°$. The numbers in the legend correspond to the surfaces in table 2.1. Solid lines indicate stone and concrete surfaces, and dashed lines indicate sandpaper surfaces. A band corresponding to the $1/r$ trend that would be expected for a self-similar fractal surface has been added for reference. The surfaces not plotted had curves very similar to those shown.

values of θ_{min} and θ_a. For the stone surfaces (solid lines) the number of asperities per centimeter varies at a rate close to $1/r$ for smaller tip radii.

This is to be somewhat expected, since many surfaces are approximately fractal over a range of length scales [17, 37, 38], so the surface properties should be similar at different length scales. Several other authors found natural rock surfaces to have fractal dimensions between 1.1-1.5 [78, 82], in the same range as our surfaces (see table 2.1). It should be noted that these surfaces are not truly self-similar, but only self-affine. Self-similar surfaces will have similar properties if the x- and y-directions are scaled equally, while self-affine surfaces will require a different scale factor in the x- and y-directions as the surface is viewed with a different scope [68]. In particular, self-affine surfaces will appear smoother at larger length scales. Truly self-similar

surfaces will have a fractal dimension of 1, while self-affine surfaces will have fractal dimensions between 1 and 2 [82].

If a surface was perfectly self-similar, the number of asperities per centimeter should vary as $1/r$: as the tip radius decreases, the spine tip should find proportionally more places to rest on the surface in proportion to the amount the tip radius was decreased. With the fractal dimension of our surfaces slightly larger than 1, we expect slight additional roughness at smaller length scales. However, the details of the normal vectors were such that this did not always correlate to additional asperities beyond $1/r$ at small radii in figure 2.3 (though it did sometimes).

At larger spine tip radii, however, the number of available asperities drops rapidly, implying that the surfaces do not behave fractally at large length scales. This is an effect of the cutting, polishing and wearing processes that have partially smoothed the stone surfaces so that large asperities are rare; at low frequencies, the power spectral densities of machined surfaces frequently fall below the fractal trend seen at higher frequencies [68].

In figure 2.3, the curves for the sandpaper surfaces have a shallow slope of less than $1/r$ for small tip radii. This occurs because the sandpaper surfaces have a relatively uniform particle size, so the number of asperities is closer to being a constant for small tip radii.

Figure 2.4 shows the number of asperities per centimeter versus spine tip radius for several values of θ_{min} and constant θ_a. As θ_{min} increases, corresponding to the need for asperities that are more shelf-like, the simulation is less likely to find useable asperities, as expected. This corresponds to a downward shift of the lines in the figure. All of the lines can be seen to follow the expected $1/r$ trend.

Figure 2.5 shows the number of asperities per centimeter versus θ_{min} and a constant spine tip radius. There are many asperities for low values of θ_{min}, which correspond to regions of the surface that are nearly vertical. Making use of these asperities would require extremely high friction between the spines and surface as well as the spines being loaded nearly parallel to the surface or towards the surface, for enhanced friction. There are relatively few asperities for high values of θ_{min}, which correspond

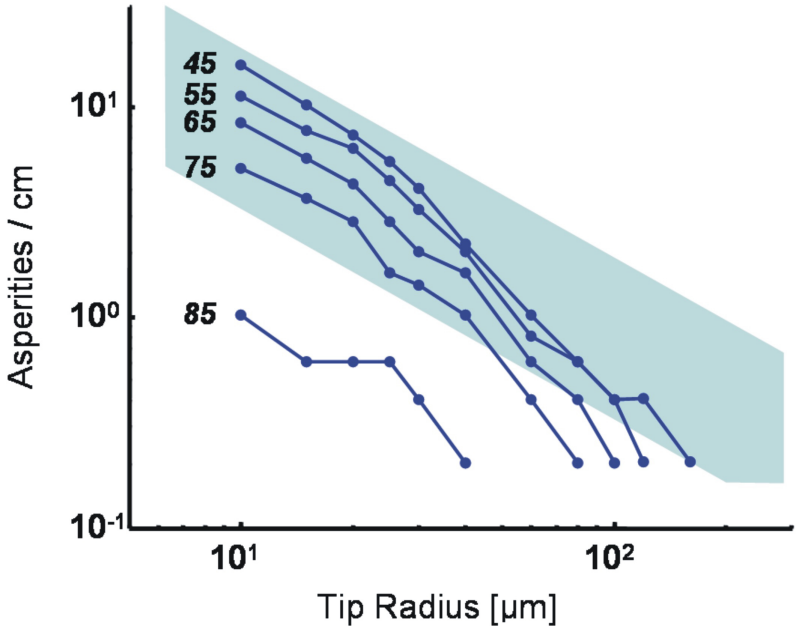

Figure 2.4: Number of asperities per centimeter versus spine tip radius for several values of θ_{min}, for a stone surface (values of θ_{min} are marked on the graph). θ_a is held constant at 65°. A band corresponding to the $1/r$ curve expected for a perfect fractal surface is shown for comparison.

to shelf-like regions.

If θ_a is varied while holding θ_{min} constant, the number of asperities/cm changes relatively little, decreasing significantly only for large approach angles where the spine is nearly parallel to the wall. For small approach angles, the spine's ability to reach the regions of the surface it hooks on to is only slightly affected. In our analysis, we examined $\theta_a = 0°, 45°, 65°$, and 80°. There was essentially no difference between any of the approach angles for 65° or less, while the 80° case showed a reduction in the number of asperities.

The distribution of lengths between asperities is approximately described by a gamma distribution, with probability density function

$$f_X(x; k, \theta) = x^{k-1} \frac{\exp(-x/\theta)}{\Gamma(k)\theta^k}, \quad \text{for } x \geq 0 \text{ and } k, \theta \geq 0, \tag{2.3}$$

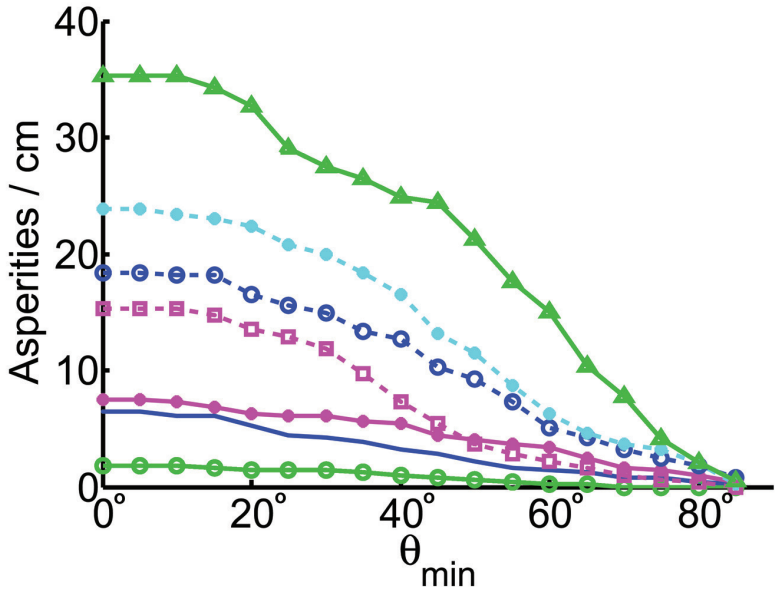

Figure 2.5: Number of asperities per centimeter versus θ_{min} for various surfaces, for a constant spine tip radius of 30μm. θ_a is held constant at 45°. The numbers in the legend correspond to the surfaces in Table 2.1. The number of asperities/cm can be seen to drop drastically as θ_{min} approaches 90°, showing that there are many fewer ledge-like regions that are perpendicular to the surface face than sloped regions more parallel to the surface face.

where x is the distance between asperities, k, θ are parameters for the distribution, and Γ is the Gamma function. Histograms of the distances between asperities are plotted for several surfaces in figure 2.6, along with the gamma distribution that was the maximum-likelihood fit. The mean distance between asperities is $k\theta$ and the variance is $k\theta^2$. The asperity lengths are approximately exponential random variables.

2.2.2 Correlation with climbing robot performance

In this section we compare the results of the foregoing analysis to the empirical results obtained with our climbing robot. The parameters θ_{min} and θ_a used by our climbing robot, SpinybotII (see figure 2.7), were measured and used in the simulation. Based on the geometry of SpinybotII, the feet are loaded at angles $3.5° < \theta_{load} < 8°$ degrees from the wall. The coefficient of friction between stainless steel spine tips and rock

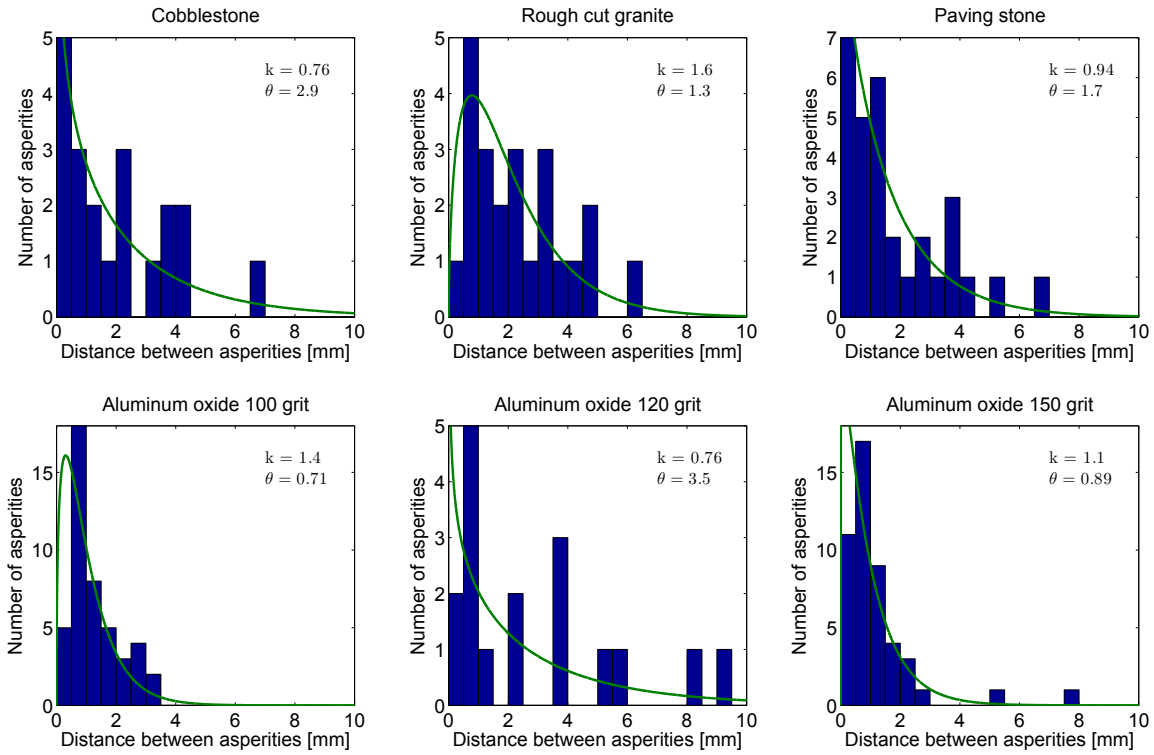

Figure 2.6: Histograms of distances between asperities for several surfaces, along with a plot of the best-fit gamma distribution. Numbers shown for k and θ are the parameters for the gamma distribution for each plot, found using a maximum-likelihood estimator. Data was found using parameters $\theta_{min} = 75°$, spine tip radius $= 10\mu m$, $\theta_a = 45°$.

is generally between 0.15 and 0.25, which corresponds to θ_{min} between 86.5° and 81° for an average θ_{load} of 5° using equation 2.1. The approach angle, θ_a, is from 45°-65°, based on the angle of the spines themselves and the motion of the tip over the surface. The tip radii, r_s, of the spines are 10-15 μm for new spines and 25-35 μm for spines dulled due to heavy use.

The results using these values qualitatively correspond to the actual performance of SpinybotII on the corresponding surfaces. SpinybotII can adhere extremely well to the Al-oxide 100 and 80 grit sandpapers, indicating that there is a high density of asperities with ledge angles of at least 81-86.5°. SpinybotII adheres less well to the Al-oxide 150 and 120 grit sandpapers, with the feet slipping down these surfaces

for a longer distance before solidly engaging, indicating a lower asperity density. It adheres poorly to the painter's 100 grit sandpaper, only rarely finding asperities. On the natural surfaces, SpinybotII adheres very well to the rough concretes, moderately well (i.e., barely well enough to climb) to the rough cut granite surface, and not at all to the ground and polished surfaces. In the simulation, if θ_{min} is 82°-85° and θ_a is 45° or 65°, at radii of 10-40 μm the ordering of the surfaces in terms of asperities/cm corresponds to the ordering of the same surfaces in terms of how well SpinybotII can adhere to them.

SpinybotII's spines do not scrape quasi-statically over surfaces. However, the effects of spine bouncing and reduced dynamic friction are mainly a reduction in the apparent asperity density. Also, asperity failure was not frequently observed for light loads on these surfaces. Thus, the relative ordering of how well SpinybotII's feet perform on different surfaces generally matches the predicted ordering in terms of asperities per unit length in the simulation.

The concrete profiles show somewhat fewer asperities than would be expected for small tip radii and very large values of θ_{min}. This is because they were recorded using a laser micrometer with a 64 μm spot size that produced some low-pass filtering. Consequently the concrete profiles appear to have few asperities in the simulation using these parameters, although in reality they have many. Also, all of the surfaces show many fewer asperities than would be expected if θ_{min} is increased above around 82°. This discrepancy is likely due to the reduced ability of the measurement instruments to accurately record abrupt changes in surface height.

2.2.3 Discussion

Dai et al. [19] present a planar model of spine/asperity contact that includes the relative size of the spine tip versus that of an asperity and coefficient of friction. Our analysis is similar, except that we use actual surface contours and compute the corresponding traced surface for the swept volume produced by a spine. Dai et al. state that the angle of spine/surface contact is key to obtaining traction between beetle claws and surfaces. However, they also discuss their results in terms of surface

Figure 2.7: Picture of upper section of SpinybotII on concrete wall and detailed view of several spines independently engaging asperities on the concrete surface.

roughness, a different parameter entirely (though it is usually correlated with the spine/surface contact angles). Our analysis indicates that the normal angle, θ, is the critical parameter, and that the linear and RMS roughness measures R_a and R_q are not always correlated with actual spine performance. As an example, the R_a and R_q of the painter's 100 grit sandpaper are larger than the corresponding values for 120 and 150 grit Al-oxide, but it has many fewer useable asperities for large assumed values of θ_{min}, due to its more rounded features.

Our present analysis is limited in that it cannot detect the presence of angles more than 90 degrees (upward-leaning ledges). Even at angles close to 90 degrees it is less accurate due to the non-zero cone angle of the profilometer stylus. For some surfaces, SpinybotII's spines may attach to many asperities with angles greater than 90 degrees.

The observed behavior of spines interacting with surfaces also differs slightly from that assumed by the model. As a foot is brought into contact with a surface and begins its downward stroke, we observe that many spines briefly catch on "unusable asperities" and then break away as the load is ramped up. There are several reasons

why the spines probably detach from these unusable asperities. The spines can deflect slightly or undergo rotations, which will lead to their slipping. This can be due to non-idealities in the toe linkage design as well as spine bending. Another possibility is that these unusable asperities are quite weak and break off the wall once the load increases past a certain point (see Appendix A.1 for analysis). Indeed, on some surfaces small particles can be observed breaking off the wall as a foot slides over it.

One final possibility is that the unusable asperities are regions where there is a ledge with a very shallow angle. In these regions, initially a spine can get stuck if there is a small but positive normal force being applied to the spine and a small shear force. However, as the shear force is increased (and normal force possibly decreased), eventually the friction force between the spine and the ledge is not large enough to overcome the applied load, and the spine slips. These asperities would be useable if the friction force between the spine and surface was higher or the loading angle was kept more towards the wall (or into the wall).

The spines also tend to skip over the surface (i.e., to become briefly airborne) after slipping off the unusable asperities and they undergo alternating regimes of static and dynamic friction. The effective coefficient of friction while this occurs is probably quite low. Finally, there is a chance that as a spine on a compliant suspension drags down the wall it may tend to follow a local groove or valley and thereby be steered away from protruding asperities. Conversely, negative asperities (pits) will tend to steer the spine into a favorable location for obtaining a grip. Hence, actual spine/surface dynamics vary depending on the surface type as well as how much the spine is able to move in the direction perpendicular to its travel.

2.3 Spine/Asperity Contact Strength

While smaller spines are more effective at engaging asperities on smooth surfaces, they also carry smaller loads. When steel spines catch on asperities, the contact typically fails in one of three ways:

- the spine fails plastically at its base due to tensile stress from bending,

- the spine tip rotates elastically such that it slips off the asperity,
- the asperity fails, typically as a particle becomes unbonded from the surrounding matrix.

In each of these cases, if we take a dimension such as the spine tip radius, r_s, as a characteristic length and scale everything uniformly, then the maximum load of the spine/asperity contact increases as r_s^2 (see Appendix A.1 for details).

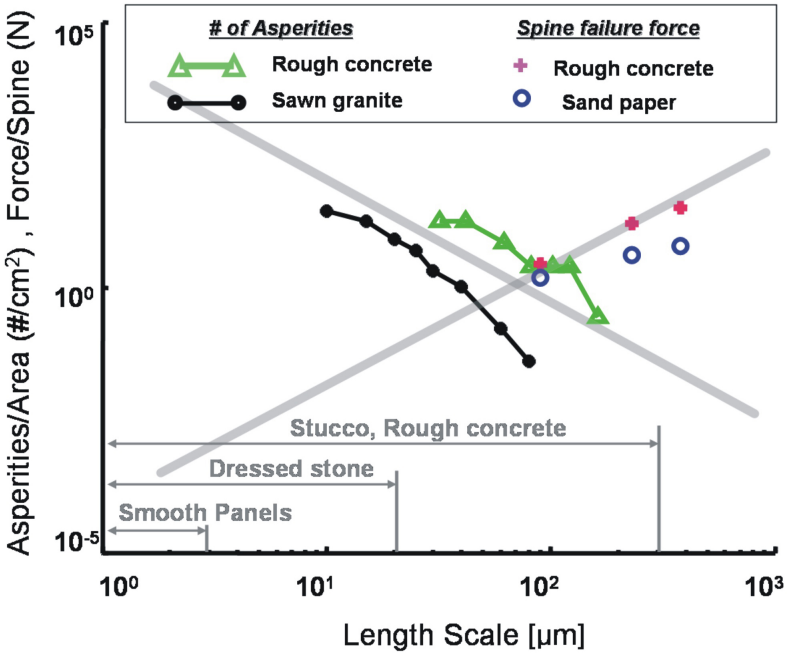

Figure 2.8: Log/log plot showing the expected r^2 trend of spine/asperity contact strength versus the expected $1/r^2$ trend for asperities per unit area of the wall. The number of asperities per unit area for surfaces of rough cut granite and concrete are plotted for comparison with the expected asperity density trend. Individual tests of spine/asperity failures are plotted for concrete and sandpaper surfaces, showing the force required to break the spine/asperity contact. Failures occurred either through asperity brittle failure or spine bending (either elastically or plastically).

Figure 2.8 shows graphically how the maximum load of the spine/asperity contact increases as r^2, while the expected number of asperities per unit area decreases as $1/r^2$. As spines become smaller we can ascend smoother surfaces because the density

of useable spine/asperity contacts increases rapidly. However, to support a given load we need proportionally larger numbers of spines because each contact can sustain less force. Thus, in order to make use of large numbers of spines, the two key design principles are:

- ensure that as many spines as possible will independently attach to asperities,
- ensure the total load is distributed among the spines as uniformly as possible.

Figure 2.8 also shows data that supports the r^2 and $1/r^2$ trends for spine/asperity contact strength and asperity density per unit area, respectively. Measurements of contact strength were done using spines of various sizes on concrete and sandpaper samples attached to a load cell. We note that the sandpaper consisted primarily of male features (which had a small bonding cross-section). Therefore, asperity failure tended to occur before spine failure on that surface. In contrast, the cast concrete primarily consisted of female features that were much stronger; so spine failure, either by excessive end rotation or plastic bending, tended to dominate. For other surfaces, all three failure modes tended to occur simultaneously. The figure also shows the asperity density data for a concrete and machined granite surface as compared to the expected $1/r^2$ for fractal surfaces. At the bottom of the figure, the representative asperity length scales for a few different surfaces are indicated. These indicate, for example, that rough concrete surfaces will present useable asperities of up to 300 μm in radius whereas smooth concrete or stone panels will present asperities of up to 20 μm. These values essentially impose an upper limit to the spine size that can be used with these surfaces.

For our first climbing robot, SpinybotI, we employed 4 spines per foot, each with a tip radius of approximately 30-50 μm. This machine was able to climb stucco and rough concrete reliably. The spine/asperity contacts could sustain loads of several Newtons (N), usually limited by brittle failure of the asperity rather than of the spine. However, for surfaces such as smooth concrete and dressed stone, the probability of a spine encountering a useful asperity during a vertical stroke length of approximately 2 cm was too low for reliable climbing. SpinybotII employs two rows of spines on each

foot, each spine having a tip radius of approximately 15-20 μm. The maximum force per spine/asperity contact is 1-2 N, and the probability of finding useable asperities per centimeter of stroke length is high. On most surfaces that SpinybotII can climb, 30-40% of the spines engage.

2.4 Spine-surface limit curve

By combining the model of how spines engage on surface asperities and the spine/asperity contact strength, we can model the forces the spines will sustain when engaged on asperities. Figure 2.9(left) illustrates an asperity with an engaged spine, corresponding again to the spine/asperity model described by equations 2.1 and 2.2.

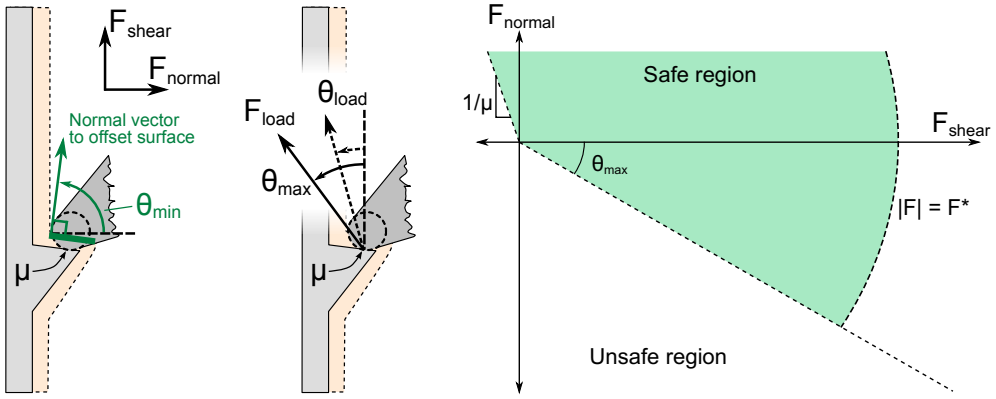

Figure 2.9: Left, diagram of spine on asperity showing angles of forces. Right, theoretical limit curve based on spine/asperity contact model.

In force-space, shown in figure 2.9(right), permitting $\theta_{load} \leq \theta_{max}$ corresponds to F_{load} within a region bounded by a straight line at an angle θ_{max} from the F_{shear} axis:

$$F_{normal}/F_{shear} \leq tan(\theta_{max}) \quad \text{where} \quad \sqrt{F_{normal}^2 + F_{shear}^2} = |F_{load}| \leq F^*. \qquad (2.4)$$

The F^* limit comes from the spine/asperity contact strength. The contact can fail due to plastic failure of the base of the spine in bending, excessive elastic rotation of the spine tip causing it to slip off the asperity, or brittle failure of the asperity

itself, as discussed previously. Each of these constraints individually will correspond to a different curve in force-space. We roughly approximate the combination of these constraints with the line $|F_{load}| \leq F^*$, which is assumed to be the force at which a typical spine/asperity contact fails (whether limited by spine strength or asperity strength).

The last constraint occurs if the spines are scraped against the surface in their non-preferred direction, up the wall in figure 2.9(left). In this case, Coulomb friction will apply, giving a slope in force-space of $1/\mu$. This can be seen with $F_{normal} > 0$ and $F_{shear} < 0$ in figure 2.9(right).

Together, all of these boundaries comprise a limit curve which designates a "safe" area. If the forces on the spine tip are within this area, the spine and surface will maintain contact.

It is important to note that this is the limit curve for a single spine/asperity contact. In a group of spines, each spine will typically catch on an asperity with a different maximum loading angle $\theta_{max,i}$ if i is the spine index. The maximum loading force magnitude F^* will likely be more consistent across spine/asperity contacts, because the spines are assumed to be the same and the material will have similar properties.

2.4.1 Limit curve testing

Testing of the spine-surface interaction was performed on a mechanized stage and force plate previously used for directional adhesion tests [90]. The stage has a positioning accuracy of $\pm 20\mu$m and force measurement accuracy of 25mN.

Ten spines designed for the RiSE climbing robot [99], described in section 4.2.2, were mounted on the stage above a tarpaper (roofing paper) surface (Royal Sovereign Shingles brand), with roughness similar to stucco, attached to the force plate. The spines were dragged across the surface at different angles after being preloaded into the surface at several depths. The spines hooked onto asperities as they encountered them.

During testing, the spines disengaged due to one of the following mechanisms: they slid off asperities because the loading angle was too large; the asperities came dislodged from the surface; or the spines hit their overload-protection bars after stretching around 11mm and were pulled off the surface. The resulting limit curve, and the maximum adhesive force magnitudes for each trial, are shown in figure 2.10.

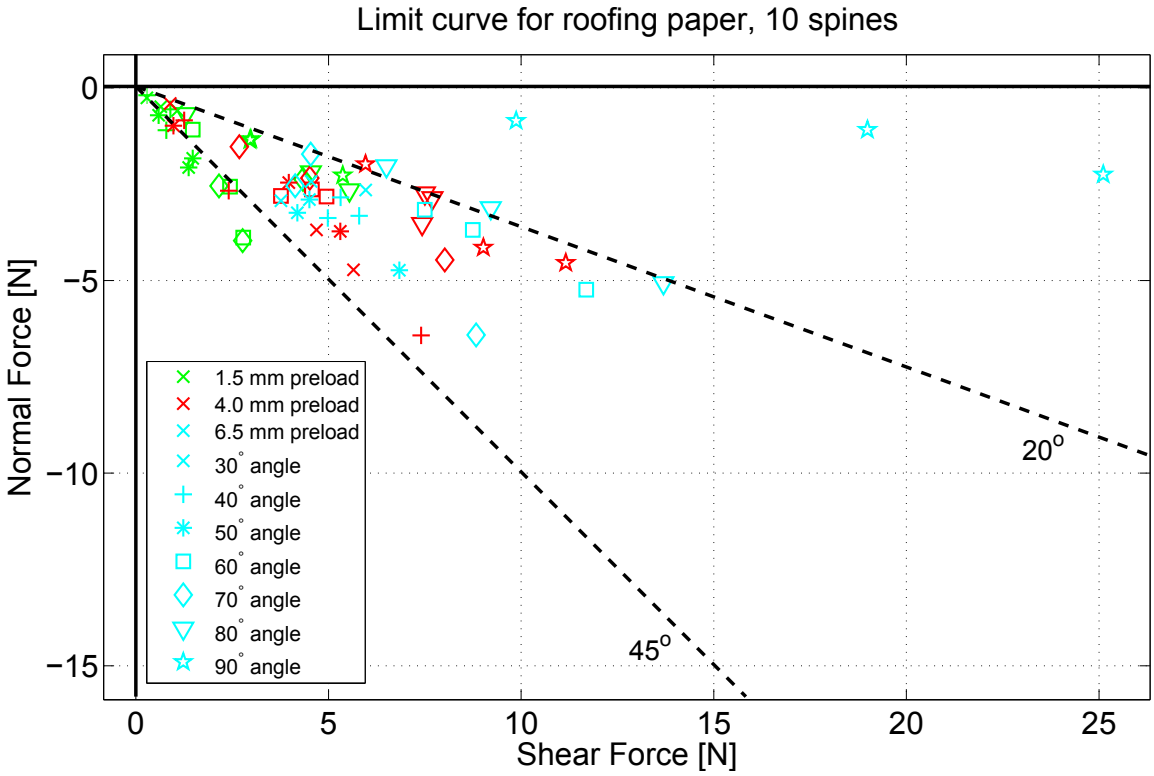

Figure 2.10: Limit curve as ten RiSE spines were dragged over tar paper.

As seen in this figure, higher preloads generally resulted in larger resulting forces before failure, although the angle of the drag had an effect as well. Dragging the spines parallel to the surface (an angle of 90° in the figure) produced larger forces than pulling the spines away from the surface (angles near 30° in the figure). With ten spines, dragged 16mm across the surface, there is a high probability that at least one spine will catch on an asperity able to support a significant load at a steep angle. In practice, generally several spines caught on asperities, and the force was typically limited by the asperity failure in these tests.

The maximum forces were generally between two angles, 20°-45° as indicated by dashed lines on the plot. The spines encounter asperities in a probabilistic manner, and the asperities themselves have maximum loading angles also in a probabilistic manner. Each of the spines can sustain different forces, since the θ_{max} and F^* limits are different for each asperity.

In theory, then, the maximum force able to be sustained by the group of spines should vary between zero degrees and some maximum angle (e.g. 45° in this case), although not all asperities will support loads up to the largest possible angle. However, even if the spines slip off asperities with smaller θ_{max} angles, they can continue sliding along the surface and catch other asperities further on with possibly larger angles. So, the limit curve for a group of spines will be similar to that of a single spine/asperity contact. As the number of spines increases, the variance of the limit curve will decrease, due to the central limit theorem.

We expect the limit curve to have larger magnitudes at smaller angles because there are more asperities with θ_{max} angles that are smaller (see figure 2.5). If the spines are exhibiting load-sharing, we expect the maximum force that can be exhibited by a population of spines to occur when the maximum number of spines have engaged on a surface. For a given loading angle, θ_{load}, the number of engaged spines should be proportional to the number of asperities with θ_{max} angles greater or equal to θ_{load}.

Furthermore, the limit curve will have larger magnitudes at smaller angles because the asperities are stronger when loaded more parallel to the wall. The effective asperity cross-section (in the direction of the applied force) will vary with the loading angle, and on average, will be maximum if the spine is pulling in the $-x$-direction. As a spine pulls further away from the wall, the asperity cross-section will shrink.

The effect of asperity strength on the resulting limit curve is shown in figure 2.11. The tarpaper used to generate the limit curve in figure 2.10 was composed of small rocks embedded into the tarpaper substrate. The bond between the rocks and the substrate was relatively weak, so rocks would come off the surface frequently. To test the effect of increased asperity strength, a thin layer of cyanoacrylate glue was spread over the tarpaper, and the test repeated. The glue flowed into the cracks between

the rocks and did not significantly affect the surface profile, while securing the rocks to the surface much better. In figure 2.11, the points corresponding to the glued tarpaper (blue dots) show increased maximum force levels while the failure points fall within the same angular ranges as without the glue (red plus signs).

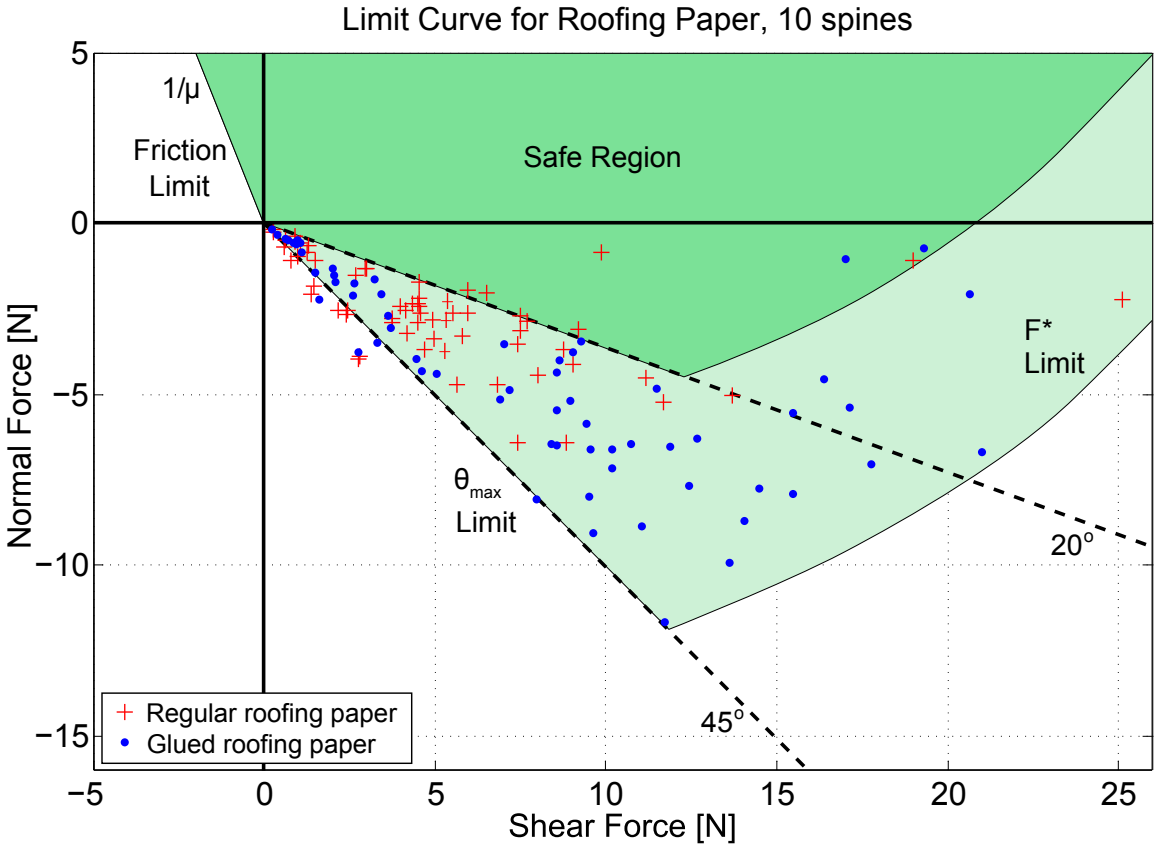

Figure 2.11: Limit curve as ten RiSE spines were dragged over regular tarpaper roofing paper and tarpaper in which the rocks had been secured better to the surface by covering the entire surface with a thin coat of cyanoacrylate glue.

Finally, like the gecko adhesive system, the limit curve of a spine/asperity contact passes through the origin in force-space. Physically, this corresponds to the spines lifting off their asperities in a direction approximately opposite to the direction in which they approached the surface. This means that the spines can detach from the surface with zero force, making control easier and minimizing energy loss from detachment.

Chapter 3

Spine suspension constraints

3.1 Introduction

Following the arguments about spine scaling in the previous chapter, to support large adhesive loads on smooth surfaces, many spines are necessary. This chapter presents constraints on spine suspensions to enable them to share the load.

3.1.1 Coordinate System and Characteristic Lengths

We first define the problem. Figure 3.1 shows a spine touching a surface. Let us embed a coordinate system at the tip of a spine with x normal to the wall and y along the wall; θ is taken anticlockwise. Forces on the spine tip are positive in the directions of the x- and y-axes. The spine tip is assumed to act as a pin joint at the wall's surface.

Following a tradition of modeling elastic mechanisms with a stiffness matrix that represents the rate of change of force with respect to displacement:

$K(x = x_0) = dF/dX|_{x=x_0}$,

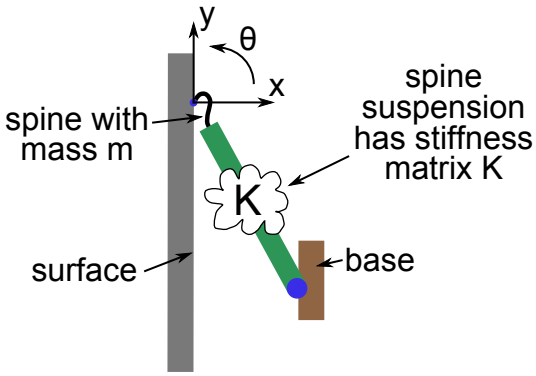

Figure 3.1: Spine suspension and coordinate system for suspension analysis. The coordinate system is centered at the spine tip, and the suspension is modeled by a stiffness matrix K. The suspension is supported by a structure defined as the "base," and the spine has a mass m.

$$K = \begin{bmatrix} k_{xx} & k_{xy} & k_{x\theta} \\ k_{xy} & k_{yy} & k_{y\theta} \\ k_{x\theta} & k_{y\theta} & k_{\theta\theta} \end{bmatrix}$$

where K is the stiffness of the suspension supporting the spine, observed from the spine tip.

Consistent with arguments in [58, 64, 18, 51] about conservative systems, we assume K is symmetric. It is also understood that K represents the instantaneous relationship between forces and displacements; K may therefore vary as the mechanism configuration changes.

The stiffness matrix K representing the spine's force-displacement characteristic corresponds to a physical linkage being attached at the proximal end to a structure that has controlled displacements in the x- and y-directions, and undergoes negligible translations and rotations.[1] In practice such a structure might be a robot leg or a

[1] In practice a robot leg does undergo some deflections as the spines are loaded. However, these are typically small compared to the elastic motion of the spine suspensions. Moreover, a modified spine stiffness matrix can be obtained as $K' = (K_{spine}^{-1} + K_{leg}^{-1})^{-1}$, where K_{leg} is a fixed stiffness matrix for the leg. Computing the stiffness matrix for such an appendage as a function of passive mechanical properties and servo gains is covered in Kao and Cutkosky [18]. An alternative to modifying the spine suspension is to add an ankle above the spine base to compensate for the leg stiffness.

mechanical stage for testing. In the rest of this chapter we refer to this structure as the "base" of the spine.

In a group of spines, the spines are assumed to be connected together only through the base, a rigid structure, so their suspensions are otherwise independent.

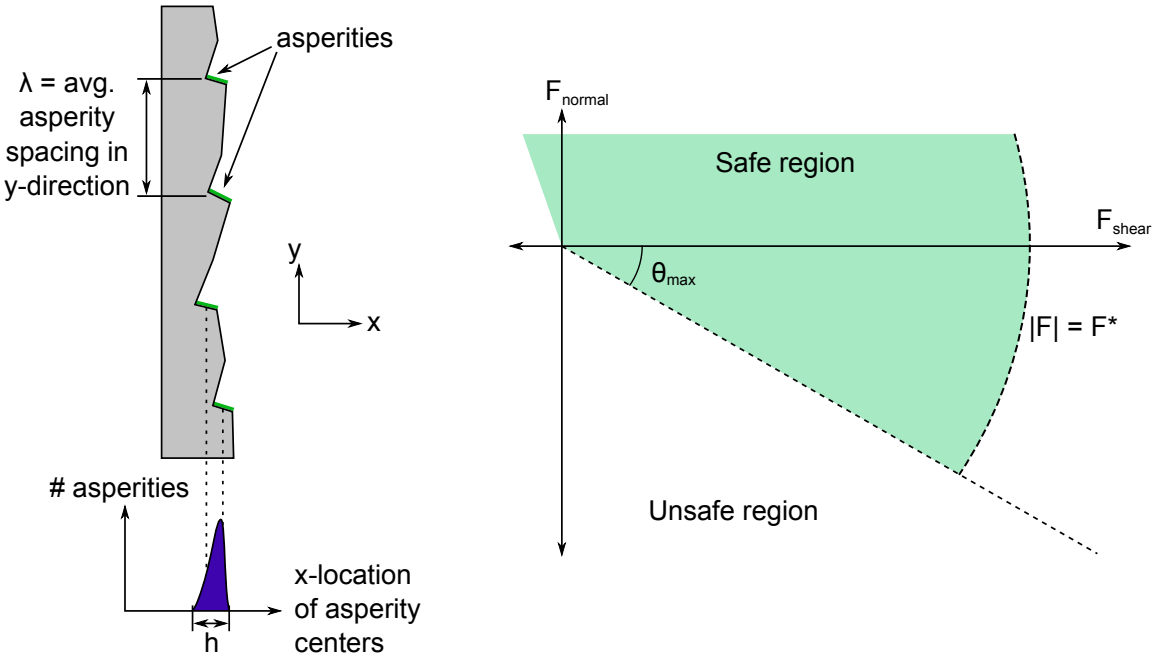

Figure 3.2: Left, λ is the average y-spacing between asperities, and h is the range of asperity locations in the x-direction. Right, in force-space, the spine-asperity contact limit curve is assumed to be bounded by a line at an angle θ_{max} from the origin and a radius of F^*.

We then define some other characteristic lengths: let λ be a characteristic length, equal to the average spacing between perchable asperities while traveling along a randomly chosen line in the -y direction. h is defined as the range of asperity locations in the x-direction, and we assume $h << \lambda$ (see figure 3.2(left)).

As discussed in chapter 2, F^* is a characteristic scalar force, defined as the average maximum force that a spine/asperity contact can sustain, and θ_{max} is an angular constraint on the loading angle. The variables F^* and θ_{max} are labeled on figure 3.2(right).

We further assume that the spine has a certain range of motion within which it

can move, due to limits on the suspension travel of a physically realizable mechanism. We define the range of motion in the x-direction to be Δx_{max} and in the y-direction to be Δy_{max}. We also define the preload (normal) force in the $x-$direction required to cause the spine to move through an $x-$displacement of Δx_{max} as $F_{x,max}$. Typically, as discussed later, spines will have $F_{x,max} << F^*$.

3.1.2 General considerations

To use many spines in parallel, each supporting a small load, each spine's suspension must have two properties:

1. Normal compliance – to have as many spines as possible come into contact with the surface when preloads into the wall are applied, the spine suspensions must be compliant in the normal direction. To permit all of the spines to reach the surface, the suspension should have $\Delta x_{max} \geq h$.

2. Shear compliance – the spines must have a suspension that permits them to move in the direction parallel to the wall, because if one spine has caught on an asperity, the other unengaged spines must be able to travel down the wall so they can encounter their own asperities. To permit a suitable number of spines to reach asperities, the suspension should have $\Delta y_{max} \geq \lambda$.

Putting these together we have a compliant linkage that permits motions in two dimensions for the spine. However, there are several other constraints to make the linkage practically useful.

The fundamental constraint on the suspension and how the spiny toe is controlled is that the forces on the spine tip must remain within the spine-surface limit curve. Because the spine suspension is a compliant structure, this means that we must apply appropriate forces to the base of the spine, or equivalently move the base through appropriate motions that correspond to the spine tip having an allowable force. For each possible spine suspension, there will be some forces/motions that the base can be moved through that correspond to the spine staying on the wall.

We model the contact between the spine tip and the wall as a pin joint, unable to transmit moments. From force balancing, it must be the case that $\sum F_x = 0$ and $\sum F_y = 0$. Because the forces applied to the spine tip are the same as those at the base, at first glance it seems like a simple matter to keep the forces on the spine tip within the safe region: just control the forces at the base of the structure, and all will be well. This is true, but there are several constraints that make certain spine designs better or worse. We must move the base of the spine through certain trajectories in (x, y, θ) space to achieve those forces.

Section 3.2 gives an example of a group of spines engaging on asperities on a surface, and shows the corresponding forces. This is useful in understanding the typical load-unload cycle used with spines, and understanding the forces experienced by the spines as a result of a particular linkage and base trajectory.

3.2 Spine engagement overview

Figures 3.3-3.6 show a series of drawings illustrating an example of how spines can be loaded, with their associated forces. In each figure, there are three subfigures, with a drawing of the spines on the left and a plot of the forces on the right.

In the drawings of the spines, forces on the spine tips are shown with arrows. The spines are connected together at a brown box, which is the spine base. The trajectory the spine base will follow is shown with three black arrows. Four numbered asperities are shown on the surface to the left of the spines. For illustration, it is assumed that each spine in the group will catch on an asperity, and the remainder of the spines will slide by that asperity.

In the drawings of the forces plotted in force-space on the right, the forces on the spine tips are shown with colored dots. The colors match the colors of the corresponding spines in the left diagram.

Figure 3.3 shows the spines being preloaded into the surface in a direction perpendicular to the surface. Initially, the spine tips have no forces on them because they are not touching the surface. In general, as the spine base moves to different

x-locations, indicated by vertical dotted and dashed lines at $x = \{x_1, x_2, x_3\}$, the forces on the spine tips will move to the corresponding line in force-space. Because the spines are connected together at their bases, all the spines in the group will have the same x-displacement. The y-displacements of the individual spines will determine where they will lie along the line in force-space. In this figure, the spine bases start between x_2 and x_3, so the forces move to the x_2 and then x_1 lines as the spines are preloaded into the wall.

Figure 3.4 shows the base of the spines being dragged parallel to the wall (at $x = x_1$) and the spines catching on the asperities. As the engaged spines extend in the y-direction, their corresponding forces can be seen to move along the corresponding curve in force-space. The unengaged spines experience a positive normal force, since they are still being pushed into the wall.

Figure 3.5 shows the base of the spines being pulled away from the wall, from initially $x = x_1$ to $x = x_2$ and then $x = x_3$ at a constant y-value. As this occurs, the forces on the spines change to lie on the different lines in force-space corresponding to the different x-values. In the bottom figure, if the base is pulled far enough away from the wall that portions of the lines fall outside the "safe region," then the spines lying on those portions of the lines will disengage. In this example, only the top spine remains engaged. The spines that disengage will return to their original resting position, shown in figure 3.6. In this example, the base position is such that the spines are not able to touch the wall and thus re-engage. Different linkages would behave differently.

To disengage spines smoothly, typically the loading trajectory is reversed, so the forces on the spines decrease to zero. This permits the spines to disengage without experiencing large, sudden changes in force, which can lead to vibration and cause disturbances while climbing.

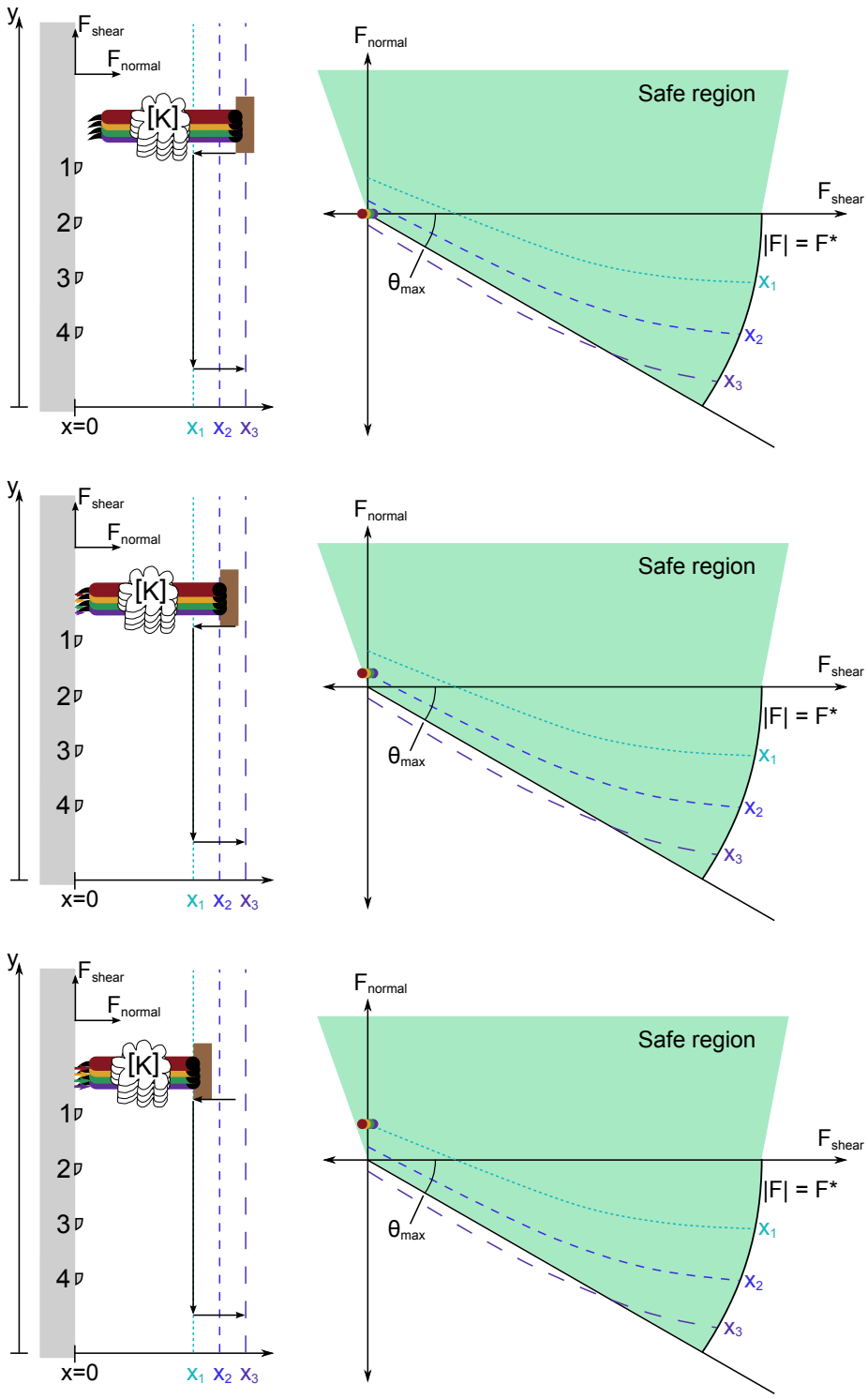

Figure 3.3: Spine loading example, preload phase

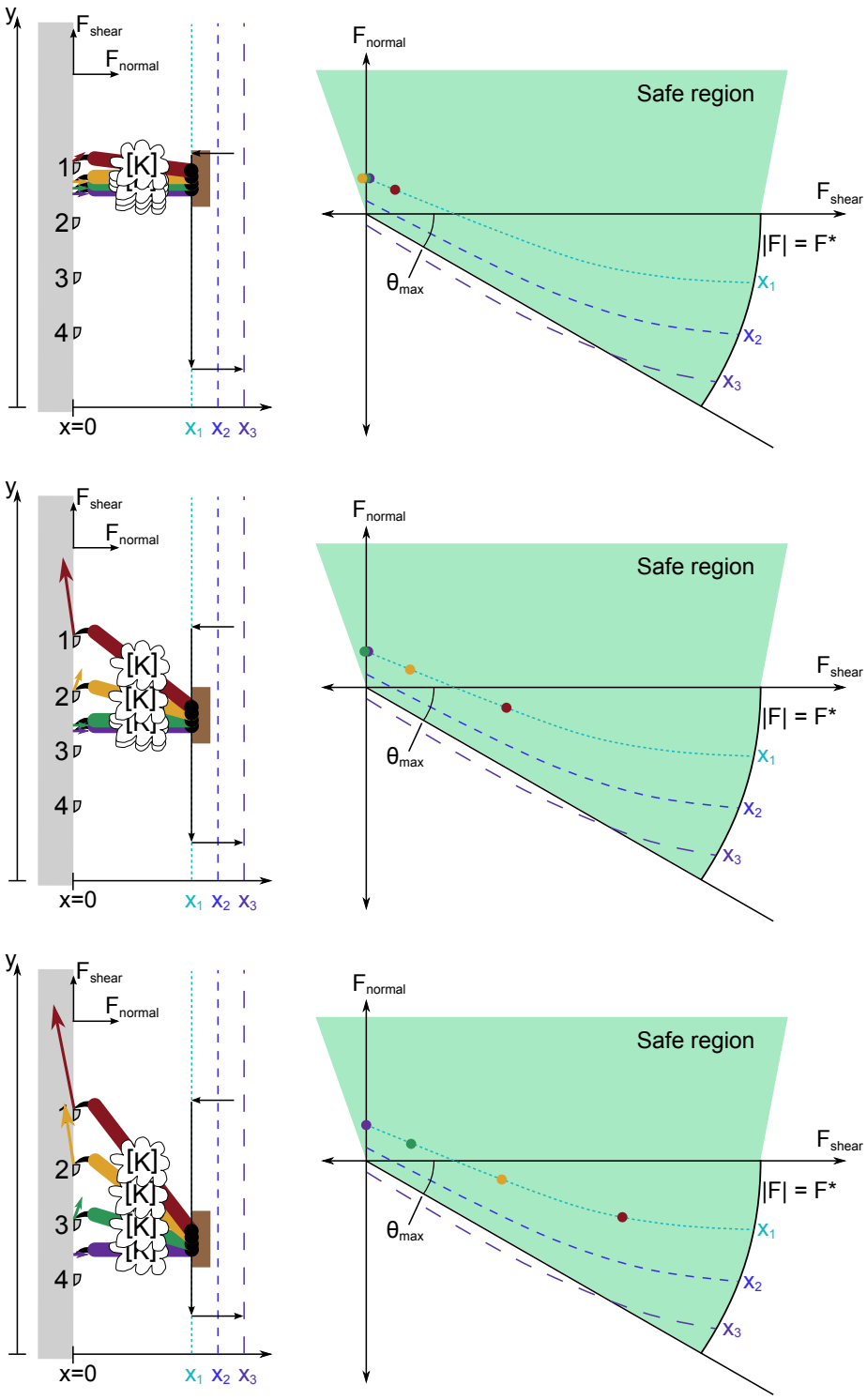

Figure 3.4: Spine loading example, shear phase

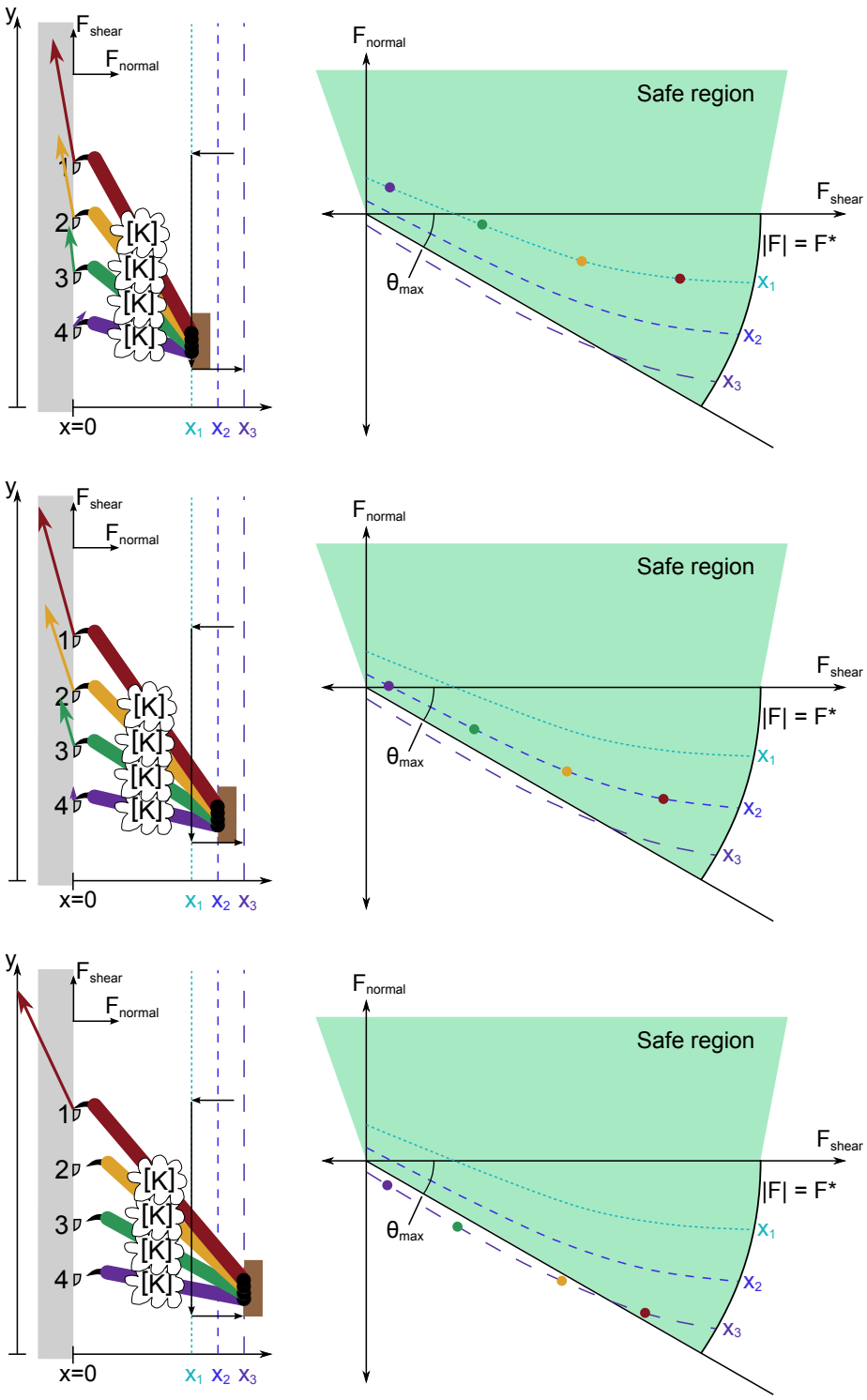

Figure 3.5: Spine loading example, pulloff phase

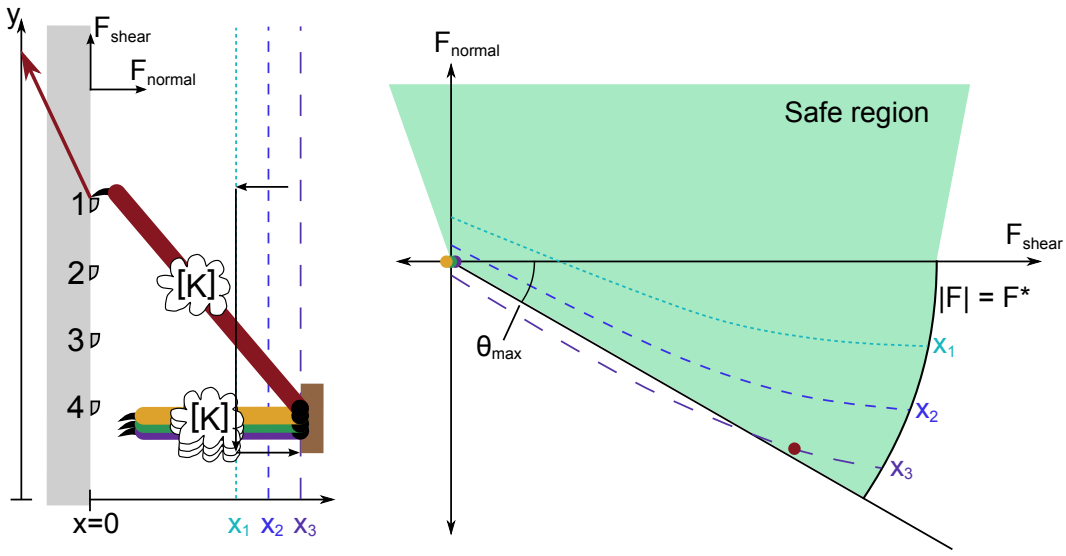

Figure 3.6: Spine loading example, final state

3.3 Constraints

In the following discussion, we assume a group of spines attached together in a row at the bases of their suspensions. Furthermore, we assume the following characteristic loading/unloading cycle:

1. Positive normal force ($F_x > 0$) is applied to the spine tip to bring it into contact with the surface.

2. The spine is dragged down ($-y$) the wall while maintaining positive normal force, until several spines have engaged on asperities. Once a spine has engaged, the shear ($+F_y$) force on it increases as the base is dragged down the surface further.

3. Adhesive loads in the normal direction ($F_x < 0$) are then applied, and possibly additional shear forces (F_y).

4. To disengage the spines, approximately the reverse trajectory is applied. The adhesive forces are either kept constant or reduced, and the shear force (F_y) is

reduced to zero, at which point the spines can be lifted off the wall and moved to another location.

There are several states within a single cycle of loading and unloading a group of spines for which constraints on the spine suspension in each state can be identified. The states are:

- Unattached – spines are tracing over the surface in order to engage on asperities. Forces are small ($\approx F_{x,max}$) and positive normal force is applied, pushing the spines against the surface.

- Loaded – spines have engaged on asperities and are supporting loads. Shear forces are typically large ($F_{shear} \approx F^*$), with moderate adhesive forces in normal direction ($|F_{normal}| \approx 0.1 - 1\ F^*$). Constraints in the Loaded state can be divided into two categories we will consider separately: Load-sharing, which deals with the forces on different spines in a group, and Geometric, which deals with physical interactions between the parts of the suspension structure and the wall.

- Re-engaging – spines have slipped off asperities or are otherwise not engaged while loads are still being supported by other spines. Forces on the group of spines as a whole are still in the same region as the Loaded state, because many spines are engaged. The spines that have slipped off their asperities have small forces, similar to the Unattached state ($|F_{normal}| \approx F_{x,max}$. Or, the spines that slipped off may quickly re-attach on new asperities and bear loads again.

- Disengaging – spines are in the process of being lifted off the surface. Initially moderate adhesive and shear loads are present ($|F_{normal}|, F_{shear} \approx 0.1 - 1\ F^*$), and then these forces decrease, ideally moving to zero, at which point the spines lift off the surface.

3.4 Unattached state

When the spines are not yet attached, as many spines as possible should stay as close to the surface as possible. It is particularly important that spines be able to reach into deep pockets or crevices on the surface, because these regions may contain asperities with favorable surface normal vectors. To accomplish this, there are two conflicting constraints on the spine suspension that must be traded off against each other.

First, if the spine is preloaded into the surface ($F_x > 0$) and dragged down the surface with a velocity $v_y < 0$, the spine may become airborne if it is dragged quickly over steep drop-offs on the surface. The times the spine is airborne will affect the swept spine volume as discussed in chaper 2. It is beneficial to minimize the time the spine is airborne.

The spine and any material attached to it can be modeled as a small mass m supported by the suspension. To a first approximation, this is a mass-spring-damper system with spring stiffness k_{xx} and mass m. This system will have a natural frequency of $f = 1/2\pi\sqrt{k_{xx}/m}$, or period $T = 1/f$. The spine will need roughly a half period or less to return to the surface after slipping off an asperity. If τ is the time to re-engage, then we should have $\tau \leq 1/2T$. For the spine to re-contact the wall before it reaches the next asperity, we must have $\tau\, v_y < \lambda$. In general, to minimize the time the spine is airborne, $\sqrt{k_{xx}/m}$ should be maximized, either by making the mass m as small as possible or making k_{xx} large. A slower v_y velocity will also decrease the distance the spine travels vertically before it re-contacts the wall.

A conflicting constraint is to make k_{xx} as small as possible when $F_{shear} \approx 0$ to enable as many spines as possible to touch the surface. If k_{xx} is too large, for very rough surfaces, some spines will not be able to reach deep pits because compressed suspensions of other spines will provide a sufficiently large force to resist the preload. More precisely, if half of the spines in a group are compressed a distance Δx_{max} due to their resting on protrusions, and the other half of the spines are not compressed at all due to their reaching into deep pits, then for a maximum preload force $F_{x,max}$ we must have $k_{xx} \leq 2F_{x,max}/\Delta x_{max}$. Furthermore, k_{xx} should be minimized because in climbing applications it is desirable to minimize the preload force $F_{x,max}$ since any

applied preload must be compensated for by increased adhesion at the other elements attached to the wall, either other attached spines or other limbs. This is one reason to have $F_{x,max} << F^*$.

3.5 Loaded state

3.5.1 Load-sharing

An important performance metric of a group of spines is their ability to share the load evenly between them. It is only effective to use many spines each bearing a small amount of force if the force can be evenly distributed between them. In particular, two properties are desirable: minimizing the maximum force on any individual spine, and keeping the loading vectors on all of the attached spines parallel. Constraints on the spine suspensions to achieve these properties refer to the load-sharing ability of the spines in the Loaded state.

Minimize the maximum force

First, the spines must share the force: the actual forces on the spines should be as similar as possible in magnitude so that the loads are shared. The constraint on any single spine is that the magnitude of the force must be less than F^*. In a group of spines, then, we wish to minimize the maximum force on any single spine. A useful metric for a group of spines is the maximum force magnitude on a single spine divided by average force on all of the engaged spines.

To minimize the maximum force on the spines, the k_{yy} and to a lesser extent k_{xx} stiffnesses should be non-linear. If the suspension is stiff at first, and then soft for large deflections, the load on each spine will increase quickly and then stay approximately constant as more spines engage.

Keep the loading vectors parallel

The second load-sharing constraint involves the θ_{max} boundary of the spine-surface limit curve. To enable a group of spines to remain attached up to the largest possible θ_{max} angle, all of the individual spines should have loading vectors at θ_{max} at the same time.

For an idealized surface where all asperities have the same θ_{max} angle, if any spine has a loading vector at an angle greater than the others, it will slip off its asperity before the others. The case where all spines have equal loading angles is the optimum where all will fail simultaneously.

In practice a surface will have asperities at various different angles, but the maximum loading angle is unknown for each spine. We can pick a conservative angle to use as the maximum loading angle θ_{max}, and then the above reasoning applies.

An alternate rationale is as follows: suppose a group of spines is initially loaded at a certain angle θ and that angle is maintained while adhesive loads on the base are increased. If the spines all sustain forces at that same angle θ, they will all remain attached (until they reach the force magnitude limit). Since each spine has been previously loaded at θ, each spine's asperity is known to sustain loads at that angle.

Suppose, however, that each spine's loading angle changes as the adhesive load increases, due to the spine linkage, even though the forces on the entire group are maintained in the same direction θ. In this case, different spines within the group must be loaded at different angles for force balancing to be correct. Then, some spines will be loaded at larger angles $\theta + \Delta\theta$ while others will be at smaller angles $\theta + \Delta\theta$. It is random which asperities can support angles larger than θ, so there is an increased probability of spines slipping off their asperities.

Furthermore, the value of θ_{max} will vary between surfaces. If the spines are to be used on a wide range of surfaces, then, the forces on the individual spines in a group should all be parallel. In this case, all of the spines will fail simultaneously independent of the particular value of θ_{max}. This is illustrated in figure 3.7. Both diagrams in this figure show the limit curves for two example surfaces, A (red) and B (blue), with different θ_{max} limits. Black dots in groups 1 and 2 show forces on two

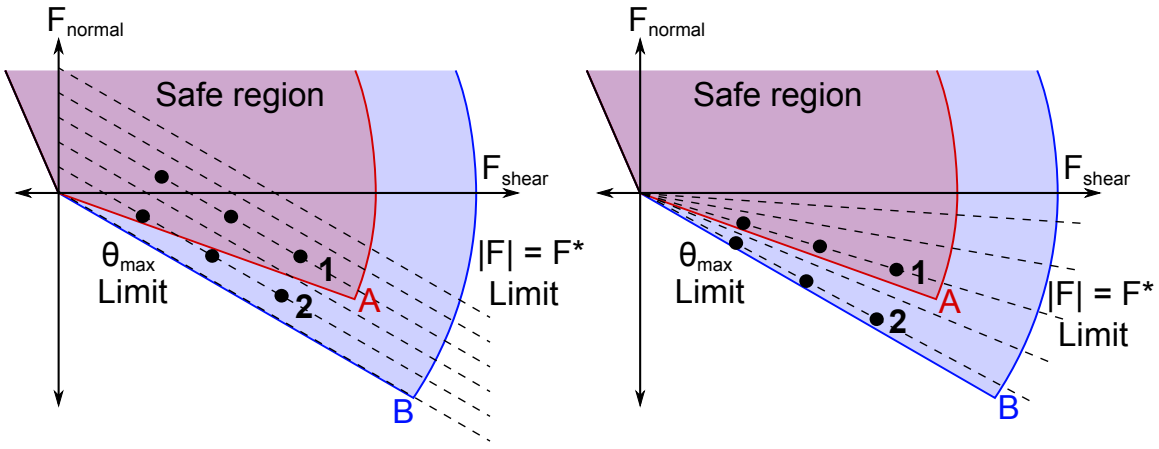

Figure 3.7: Diagrams showing how a nonlinear spine linkage stiffness, corresponding to radial lines, is best at load sharing across different surfaces. Limit curves are shown for two example surfaces, A and B. Black dots in groups 1 and 2 show forces on two different groups of three spines. On the left, a constant-stiffness linkage will cause the three spines to fail simultaneously at surface B, but on surface A they will fail at different times, shown by how some of the dots in group 2 are outside the limit curve for surface A. On the right, a nonlinear stiffness with radial linkage lines will cause the spines to fail simultaneously on both surfaces A and B.

different groups of three spines. The left diagram shows a set of lines corresponding to spines with a constant stiffness matrix as they are loaded. These spines would work well on surface B, because all engaged spines would fail simultaneously. However, on surface A the most-loaded spines will fail before the least-loaded spines, indicating that the load is not evenly shared. The right diagram in figure 3.7 shows a spine linkage with a nonlinear stiffness that corresponds to radial lines. In this case, the spines will fail simultaneously on both surface A and surface B.

Figure 3.8 shows the forces experienced by a group of spines with an ideal linkage, and the corresponding positions of the spines. The left side shows a diagram of a group of spines connected together at one point to the base, shown as a brown box. These spines are attached at various locations in the y-direction on a flat wall surface. The base of the spines is permitted to move within a specified region in xy-space, due to the spine linkage not being able to extend infinitely. For a given value of x, the spines can deflect a maximum of Δy_{max} in the y-direction. The right side of

the figure shows the forces experienced by those spines, as well as a diagram of the limit curve for each spine-asperity contact, with the safe region colored in green. In this diagram, spine N is deflected this maximum amount, and has the corresponding maximum possible force, $|F| = F^*$, indicated by the N next to the point in force-space. Spine 0 is not deflected at all in the y-direction, and has no force on it. The forces on the spines are in a radial line from the origin, corresponding to the ideal suspension.

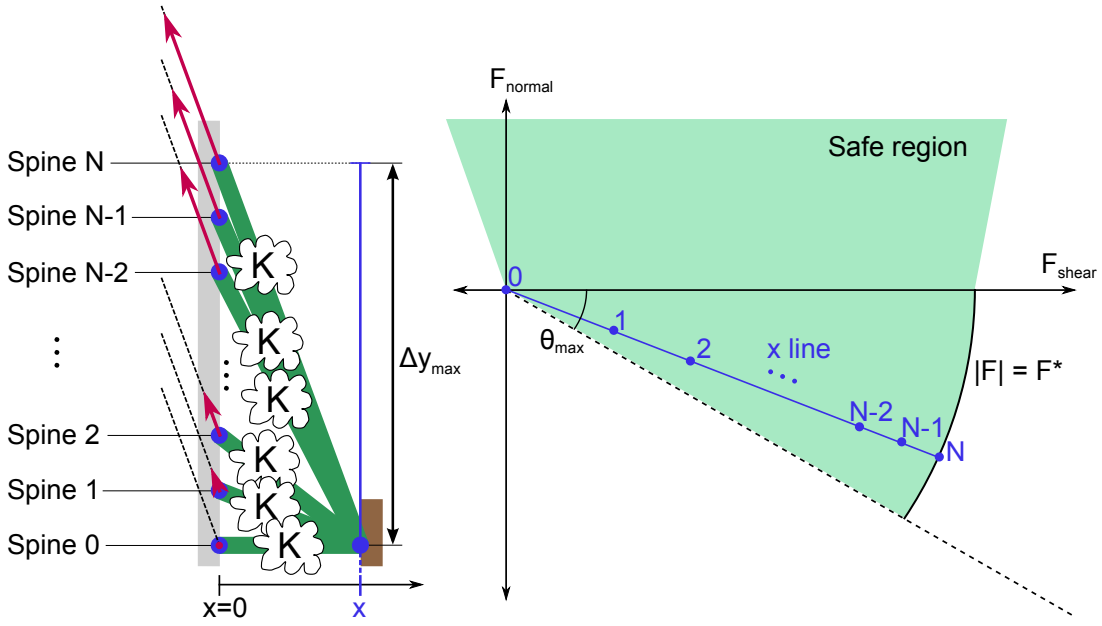

Figure 3.8: Positions and forces on different spines in a row with ideal load-sharing such that the loading vectors are all parallel. The diagram on the left illustrates the forces on individual spine tips engaged at various locations along a flat surface, while the plot on the right shows the forces corresponding to those spines. Spine N is extended the maximum possible distance, Δy_{max}, determined by the spine suspension.

The ideal suspension requires a set of spine base positions with varying x-deflections but with zero force on them. For these points, the k_{xx} stiffness must be zero. This ideal situation would not be possible with a real spine suspension, where the stiffnesses must always be non-zero, though possibly very small. In practice, to get close to ideal load-sharing, the suspension should have $F_{x,max} << F^*$ (note that F^* is determined by the surface or spine strength, while $F_{x,max}$ can be chosen as part of

the suspension design).

Mathematically, the ideal suspension corresponds to the following: If the base of the spines moves purely in the y-direction, in the equation

$$\begin{bmatrix} dF_x \\ dF_y \end{bmatrix} = \begin{bmatrix} \partial F_x/\partial x & \partial F_x/\partial y \\ \partial F_y/\partial x & \partial F_y/\partial y \end{bmatrix} \begin{bmatrix} dx \\ dy \end{bmatrix}$$

we have $dx = 0$. Also, for a constant loading angle θ_{const}, we must have

$$\begin{aligned} dF_x &= dF \sin\theta_{const} \\ dF_y &= dF \cos\theta_{const} \end{aligned}$$

for a given value of x, with $\theta_{const} = f(x)$ where $f(x)$ is some function. This leads to

$$\begin{bmatrix} dF_x \\ dF_y \end{bmatrix} = \begin{bmatrix} \star & \partial F_x/\partial y \\ \star & \partial F_y/\partial y \end{bmatrix} \begin{bmatrix} 0 \\ dy \end{bmatrix}$$

where $\star$ can be any value because it is multiplied by zero, and

$$\begin{aligned} dF_x = dF \sin\theta_{const} = \partial F_x/\partial y \, dy = k_{xy} \, dy \\ dF_y = dF \cos\theta_{const} = \partial F_y/\partial y \, dy = k_{yy} \, dy \end{aligned}$$

so

$$\frac{k_{xy}}{k_{yy}} = \frac{\sin\theta_{const}}{\cos\theta_{const}} = \tan\theta_{const}$$

which must hold true for a given value of x.

Furthermore, for a stiffness matrix to be physically realizable, the stiffness matrix must be symmetric [58], so $k_{xy} = k_{yx}$. Practically, this corresponds to the region of valid base positions being non-rectangular, as shown in figures 3.9 and 3.10.

A derivation of the region of valid base deflections for the ideal linkage is as follows, and uses the notation in figure 3.9. We assume a uniform x-spacing of the base positions, between x_{shear} and x_0, corresponding to a uniform θ-spacing of the

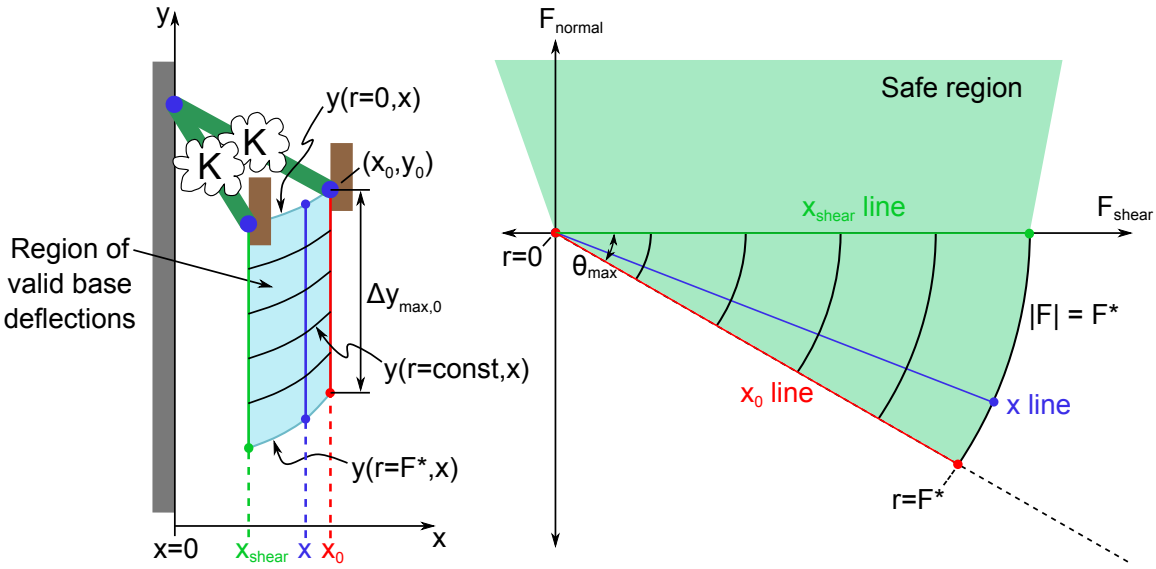

Figure 3.9: Diagram of forces (right) and base positions (left) for the ideal suspension. The base of the spines can move horizontally between $x = x_{shear}$ and $x = x_0$, and vertically between the curves $y(r = 0, x)$ and $y(r = F^*, x)$. At $x = x_0$, the maximum spine displacement is $\Delta y_{max,0}$.

lines in force-space, between $\theta = 0$ and $\theta = \theta_{max}$, respectively. This results in the following equations for the spine tip forces as a function of the base position (x, y):

$$F_x = -r(x, y)sin(A(x - x_{shear}))$$

$$F_y = r(x, y)cos(A(x - x_{shear}))$$

where x_{shear} is the position of the base closest to the wall, x_0 is the position of the base furthest from the wall, $r(x, y)$ is the magnitude of the applied force, and

$$A = \frac{\theta_{max}}{x_0 - x_{shear}}$$

Using the initial conditions

$$r(x_0, y_0) = 0$$

$$r(x_0, y_0 - \Delta y_{max,0}) = F^*$$

and setting

$$\frac{\partial F_x}{\partial y} = \frac{\partial F_y}{\partial x}$$

so that the stiffness matrix is constrained to be symmetric, we get:

$$\frac{\partial F_x}{\partial y} = -\frac{\partial r(x,y)}{\partial y}\sin(A(x - x_{shear}))$$
$$\frac{\partial F_y}{\partial x} = \frac{\partial r(x,y)}{\partial x}\cos(A(x - x_{shear})) - r(x,y)A\sin(A(x - x_{shear}))$$
$$\Rightarrow r(x,y)A\tan(A(x - x_{shear})) = \frac{\partial r(x,y)}{\partial x} + \frac{\partial r(x,y)}{\partial y}\tan(A(x - x_{shear}))$$

which we solve with Mathematica [105]. This results in:

$$r(x,y) = \sec(A(x - x_{shear}))\ f(y + 1/A\ \ln(\cos(A(x - x_{shear}))))$$

where $f()$ is any arbitrary function of the argument. Choosing $f(u) = \alpha u + \beta$ which gives us enough free variables for the initial conditions, and plugging in the $r(x_0, y_0) = 0$ initial condition, we get:

$$\beta = -\alpha(y_0 + 1/A\ \ln(\cos(A(x_0 - x_{shear}))))$$

Plugging this back into the original equation for $r(x,y)$, we get:

$$r(x,y) = \alpha\ \sec(A(x - x_{shear}))\ [(y + 1/A\ \ln(\cos(A(x - x_{shear}))))$$
$$-(y_0 + 1/A\ \ln(\cos(A(x_0 - x_{shear}))))]$$

Next plugging in the second initial condition, $r(x_0, y_0 - \Delta y_{max,0}) = F^*$, we solve for α:

$$\alpha = -\frac{F^*}{\Delta y_{max,0}}\cos(A(x_0 - x_{shear}))$$

which results in

$$r(x,y) = -\frac{F^*}{\Delta y_{max,0}}\ \frac{\cos(A(x_0 - x_{shear}))}{\cos(A(x - x_{shear}))}\ [y + 1/A\ \ln(\cos(A(x - x_{shear})))$$
$$-(y_0 + 1/A\ \ln(\cos(A(x_0 - x_{shear}))))]\ .$$

Rearranging this, we find lines of constant radius $r(x,y) == r$ satisfy the equation

$$y|_{r=const} = -r\ \frac{\Delta y_{max,0}}{F^*}\ \frac{\cos(A(x - x_{shear}))}{\cos(A(x_0 - x_{shear}))} + y_0$$
$$+1/A\ \ln(\cos(A(x_0 - x_{shear})))) - 1/A\ \ln(\cos(A(x - x_{shear})))\ .$$

A plot of an example valid region of the base deflections, and a plot of the corresponding forces plotted in force-space, are shown in figures 3.10 and 3.11, respectively. In these figures, $(x_0, y_0) = (2, -2)$[cm] and $\Delta y_{max,0} = 1$ cm.

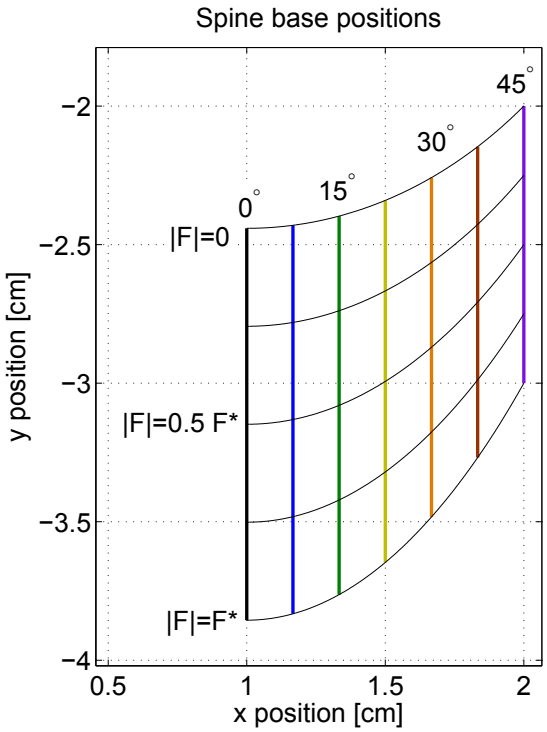

Figure 3.10: Base positions for ideal suspension. Black lines correspond to positions of constant magnitude forces, while the vertical colored lines correspond to different angular loads. Labels correspond to those in figure 3.11.

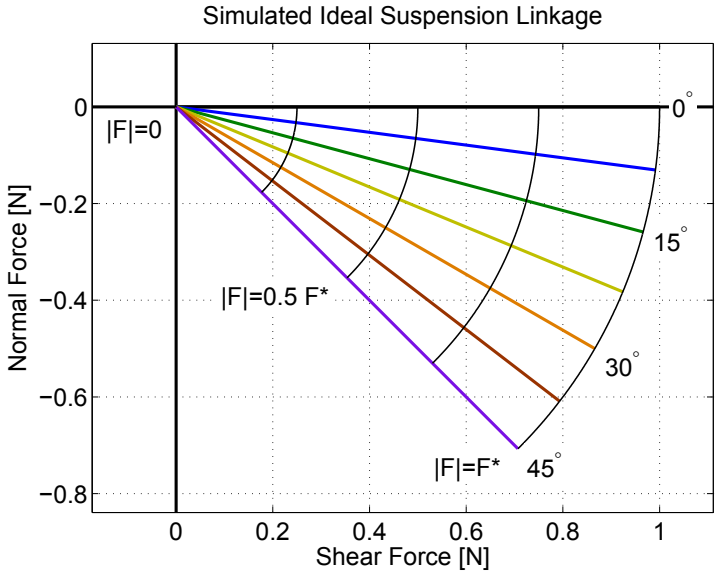

Figure 3.11: Ideal suspension in force-space, with labels corresponding to those in figure 3.10.

3.5.2 Constraints due to the wall

During the Loaded state, there are also geometric constraints on the suspension because the wall itself presents a physical constraint in two ways.

First, if the suspension requires us to move the base of the spine towards the wall significantly in order to maintain appropriate forces on the spine tip, the wall may prevent this motion. For example, in figure 3.12(left), the spine base will not be able to move towards the wall. Furthermore, in some cases the wall may actually protrude under the spine base (this may be common with a rough surface), and so the spine base may not be able to move towards the wall as much as in the nominal case.

Requiring the base of the spines to move towards the wall during loading is common for many linkages. All spines will need to move towards the wall to some extent to achieve a preload force. Furthermore, if the spines have $k_{xy} < 0$ to achieve self-reengagement (see section 3.6), the base must move closer to the wall when the spines are loaded. This is the case for the ideal suspension for load-sharing discussed in section 3.5.1.

For suspensions with $k_{xy} < 0$, moving the base of the spine closer to the wall will achieve loads at smaller loading angles. However, for some linkage geometries, the base of the spines can run into the wall at large preloads, limiting the range of motion and reducing the nominal distance of Δx_{max}. With this reduced range of motion caused by the wall, the spine linkage characteristics are then poor. An example of this can be seen in figure 3.13: the bottom set of figures corresponds to a linkage that must move a large distance toward the wall (past the lines for preloads that are drawn on the figure) to have a good linkage behavior. If it is limited to the preloads shown in the figure (6mm) because the wall would interfere at larger preloads, then it can only sustain very small forces.

In these cases, the fundamental geometry of the spine should be changed, to have better linkage characteristics without requiring such large displacements towards the wall.

Second, the spine suspensions may have internal structures which may come into

contact with the wall as the spine is loaded. For example, typically in our implementations a spine is embedded in a region of hard polyurethane which is supported by a compliant linkage. If that compliant linkage permits the hard polyurethane to rotate until it touches the wall, this will cause a positive normal force at that contact point. Because the structure needs to remain in static equilibrium, this will then cause a force at the spine tip which is in the opposite direction, which pulls the spine tip away from the wall. An example of this can be seen in figure 3.12(right).

This effect can also occur with just the metal spine itself, if the spine rotates far enough that the shank of the spine pushes against the surface. To prevent rotation of the spine as it is loaded, the stiffness matrix for the spine suspension must have large $k_{y\theta}$ and $k_{x\theta}$ terms. It was found in practice that spine angles between 45-60 degrees are generally preferable for attaching to the surface. If the spine is limited to rotating 15° (=0.262 radians), then the stiffness matrix must have $k_{y\theta} > F^*/0.262$ to prevent excessive rotation during loading, and $k_{x\theta} > F_{x,max}/0.262$ during preload.

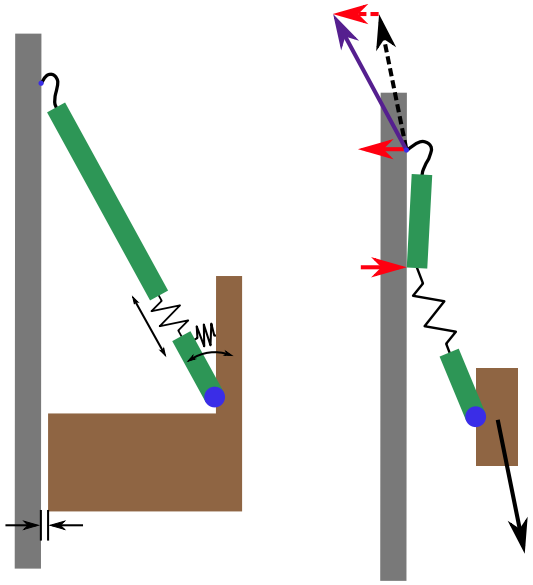

Figure 3.12: Left, the wall can prevent the base of the spine from moving through a desired trajectory. Right, part of the spine suspension can run into the wall.

3.5.3 Other constraints while loaded

Another major constraint on the spine suspensions is that the spines should be able to attach to asperities with small θ_{max} angles. For the spines to be able to be used on a wide range of surfaces, they should be able to both attach to asperities with large and small θ_{max} angles. Alternatively, spines may need to attach with small θ_{max} angles if, for example, they are used on the rear feet of a robot, where less adhesion is required but large levels of shear force are required.

To attach to asperities with small θ_{max} angles, the linkage lines in force-space must fall within the safe region bordered by that small θ_{max} angle. Two examples of different linkages are shown in figure 3.13. In this figure, the right diagrams show linkages and the regions that the base of the spines are permitted to move through. The linkages used are the "stalk model," explained further in section 4.2.3, here with parameters $k_{ext} = 150N/m, k_\theta = 0.01Nm/radian, \theta_{preload} = 0, l_0 = 0.03m$. The top two diagrams have $\theta_0 = 20°$ and the bottom diagrams have $\theta_0 = 50°$. The left diagrams show the forces experienced by the spine tip, with linkage lines overlaid. In all of the diagrams, the spine is assumed to be attached to an asperity with $\theta_{max} = 20°$.

The top two figures show an example of a spine with a linkage that permits the spine tip to experience forces throughout a significant portion of the safe region (while the spine is in adhesion). In the left figure, the upper-most linkage line, corresponding to a preload of 6.0mm, will permit the spine to experience adhesive loads at angles of $< 4°$ at a magnitude of $|F| \approx F^*$. This spine will be able to attach to asperities with θ_{max} angles as little as 4°.

For comparison, the lower figures show an example of a spine that cannot attach well to asperities with small θ_{max} angles. The left figure shows that the linkage lines go out of the safe region at magnitudes of 0-0.5N. In the right figure, this corresponds to the base only being able to move through less than half of their possible base deflections before the spine disengages.

In summary, this means that the spine will only be able to support very small loads on asperities with $\theta_{max} < 20°$. Applying larger forces will cause the spine to leave the safe region, or exceed the region of valid base deflections. If the latter occurs, the

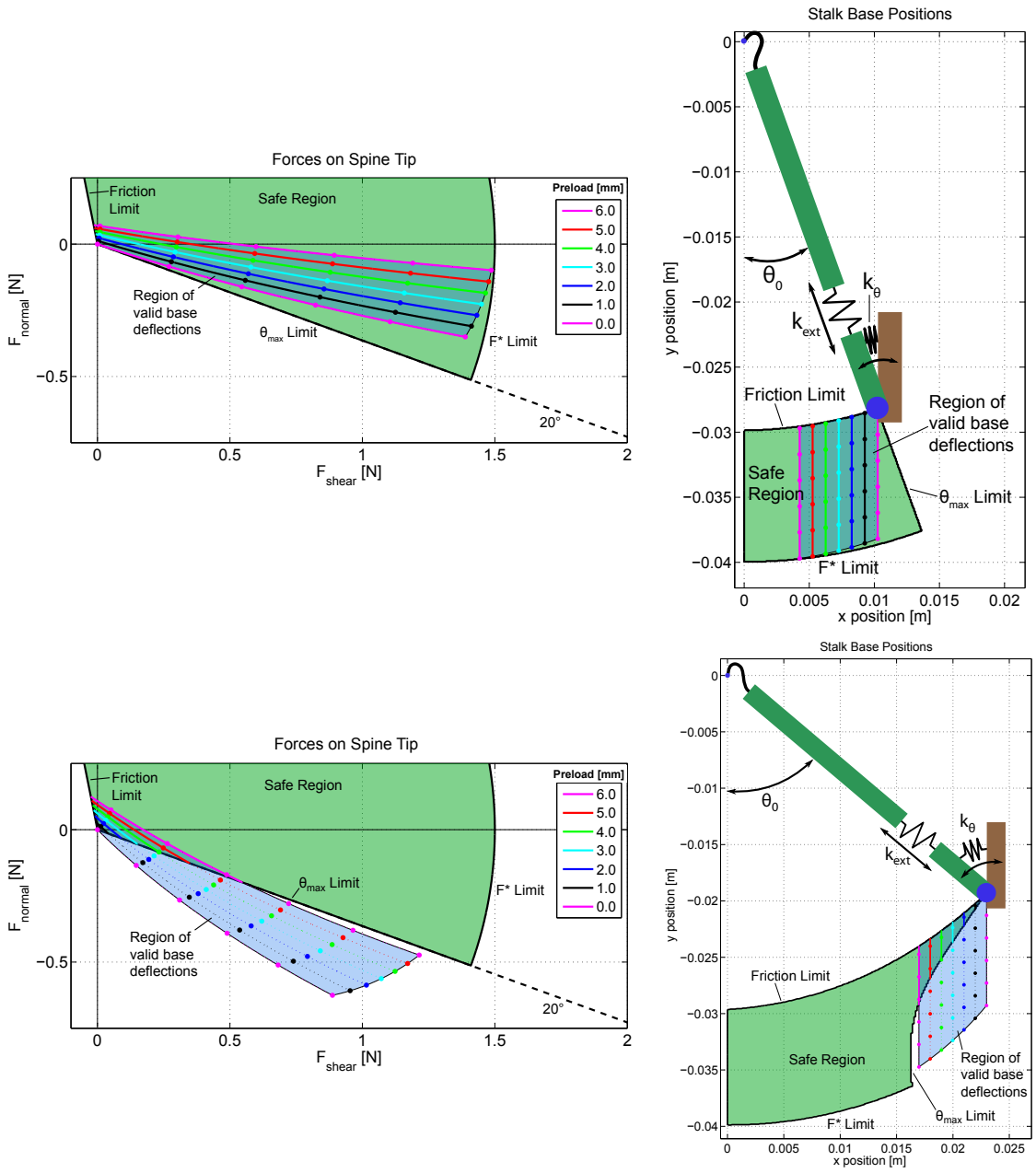

Figure 3.13: Two examples of linkages with different performance when attaching to asperities. The left plots show the normal and shear forces experienced by the spine tip when the spine base is moved through different trajectories, and the "safe region" where the spine will stay attached to an example asperity with $\theta_{max} = 20°$. The diagrams on the right show the deflections of the spine base that cause those forces: these deflections fall within the linkage's "region of valid base deflections." The right diagrams also show the safe region from the left plot, transformed into x-y space via the linkage kinematics.

behavior is unknown, but generally load-sharing will decrease markedly and one spine will support much larger loads than the others. So, in practice, this spine suspension will work poorly on asperities with $\theta_{max} < 20°$. If this spine suspension was used on a surface with many asperities with $50° < \theta_{max} < 20°$, however, it would work very well because the suspension linkage lines on the force diagram would fall within the safe region. This behavior might be useful if the spines were only intended to attach to asperities with large θ_{max} angles. Likewise, the spine suspension in the top two diagrams in figure 3.13 will not work well if forces are applied between $20 - 50°$. In that case, load-sharing will be poor and one spine will take the majority of the load.

In this particular example, the design can be optimized for small θ_{max} angles simply by lowering θ_0, as illustrated in the top diagrams. Further discussion of this particular linkage design and the effects of varying θ_0 can be found in section 4.8. But in general, many linkage designs are unable to attach well to asperities with low θ_{max} angles. To work, the linkage must have linkage lines at shallow angles. As discussed in section 3.5.1, if the linkage lines are perfectly radial, this corresponds to having a stiffness matrix with

$$k_{xy}/k_{yy} = \tan\theta_{const}$$

where θ_{const} is the angle of the linkage line. In practice, it will be difficult to achieve perfectly radial linkage lines, but if a linkage has a stiffnesses close to this, for small values of θ_{const} within the range of valid base positions, it should have good behavior.

Finally, it is important to be able to move the base of the spines downwards parallel to the wall, because the spines can slip. In practice, on a climbing robot spines are frequently slipping, due to surface failure or spines being overloaded and hitting their overload protection or having forces outside the limit surface. So these spines will then come off, and the foot will slip down the wall a little and the spines will (ideally) re-engage (the ability of the spines to re-engage will be discussed at length in section 3.6). The only steady-state trajectory that will enable constant sliding is a path parallel to the surface.

3.6 Re-engaging state

Another highly desirable but not fundamentally necessary property of spine suspensions is the ability of the spines to re-engage the wall if they slip off of an asperity. In practice, on climbing robots spines frequently disengage, due to vibrations in the robot or spines slipping off of asperities with low θ_{min} angles. If these spines do not engage the wall again after they slip off, this can lead to the foot detaching entirely.

To have the spines be able to self-re-engage, the base of the spines must be close enough to the wall that detached spines will press back against the wall with enough preload to re-engage. This is illustrated in figure 3.14. On the left, a spine has come off the wall but the engaged spines have extended far enough away from the wall that the spine does not even touch the wall. On the right, a spine has come off and now is pressed against the wall with preload force $F_{springback}$ in the normal direction. To re-engage, this force must be sufficiently large ($\approx F_{x,max}$).

In the stiffness matrix, the base of the spines moving towards the wall when positive shear loads are applied corresponds to the k_{xy} term being negative, and large enough that $F_{springback}$ is sufficiently large under moderate shear (F_y) loads. If $F_y \approx F^*$, to have the base move towards the wall a distance Δx_{max}, we must have $k_{xy} \approx F^*/\Delta x_{max}$. At this point, the unattached spine's k_{xx} stiffness must be $k_{xx} \leq 2F_{x,max}/\Delta x_{max}$ as discussed in section 3.4 about the Unattached state.

If a spine comes off an asperity, usually the base of the group of spines will displace down the surface ($-y$) so that the remaining engaged spines will stretch enough to accomodate the extra load that was formerly carried by the spine that just disengaged. If the detached spine can re-engage very quickly, it may be able to catch on an asperity and take some of that load. If it does not catch on an asperity immediately, it will be ready to catch on one if a different spine comes detached.

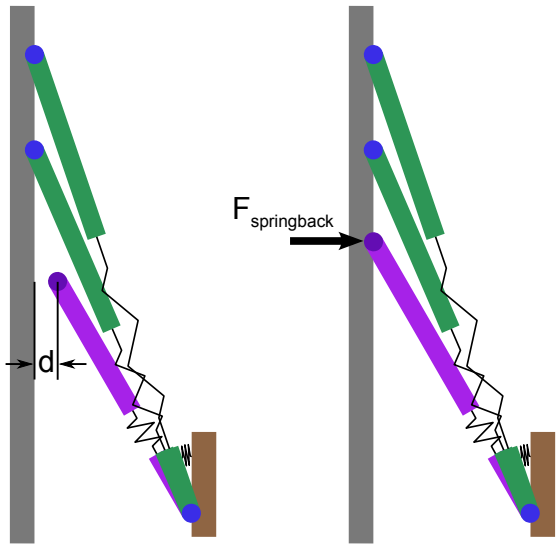

Figure 3.14: Requirements for spines to self-re-engage. Left, the purple spine has detached and returned to its original unloaded configuration, but is too far away from the wall to re-attach. Right, the spine is touching the wall again, and will experience a normal force of $F_{springback}$.

3.7 Disengaging state

When the spines are disengaging, the forces in the x- and y-directions on each spine are ideally reduced to zero, and then the foot can be lifted off the wall. In practice, the spines usually slide up the wall a little, inducing forces in the $-y$ direction. This occurs because spines engage at different y-locations along the wall, and so the spines that engage later may slide up the wall to the point where other spines first engaged. Furthermore, the robot or human controlling the base of the spines may not perfectly detect that the force has gone to zero, and may continue to drag the spines up along the wall in a disengagement trajectory.

Forces on spines dragging up the wall ($+y$) will be $F_y < 0$. In this case, the suspension must prevent the spine from rotating, which may lead to jamming in small crevices in the surface. We assume the maximum forces to disengage are comparable to the maximum preload force, $F_{x,max}$. If the spine is limited to rotating 15° (=0.262

radians), then the stiffness matrix must have $k_{y\theta}, k_{x\theta} > F_{x,max}/0.262$ to prevent excessive rotation during disengagement.

3.8 Summary

A summary of the constraints on the spine suspension stiffness matrix is shown in table 3.1. Because a single suspension must accomodate all of these constraints in different portions of the spine's load/unload cycle, and ideally accomplish effective load-sharing, the suspension must have nonlinear stiffnesses.

Table 3.1: Spine suspension stiffness matrix constraints

State	k_{xx}	k_{yy}	k_{xy}	$k_{x\theta}$	$k_{y\theta}$	$k_{\theta\theta}$
Unattached	tradeoff	-	-	-	-	-
Loaded–load-sharing	non-linear	non-linear	non-linear and < 0	-	-	-
Loaded–geometric	-	-	-	$> \frac{F_{x,max}}{0.262}$	$> \frac{F^*}{0.262}$	-
Re-engaging	$\leq \frac{2F_{x,max}}{\Delta x_{max}}$	-	< 0	-	-	-
Disengaging	-	-	-	$> \frac{F_{x,max}}{0.262}$	$> \frac{F_{x,max}}{0.262}$	-

3.9 Effects of an ankle

The foregoing analysis assumed that the spines were individually connected to an object, such as a robot leg, that had very small rotations even if significant forces and moments were applied. In practice, however, it is sometimes useful to have an "ankle" or secondary suspension above a group of spines. This ankle suspension typically is chosen to permit rotational movements (i.e., $k_{x\theta}$ and $k_{y\theta}$ are relatively small) while being stiff in the translational directions (k_{xx}, k_{xy}, k_{yy} are large).

The ankle can be added or modeled for two reasons. First, robot legs sometimes have unintentional torsional compliance due to forces being applied at the end of a relatively long structure; this compliance can be modeled by an "ankle" suspension. Second, sometimes an actual ankle is put in place, for the express purpose of permitting rotational movements of a group of spines. The purpose is to accomodate greater variations in the height of the surface while still affording robust attachment. If a robot is running open-loop or is moving at high speed, with no sensor detecting the distance to the ground, some forgiveness in the alignment of the foot with the ground is beneficial.

The existence of a compliant ankle has little effect on the preceding principles. Because spines are used in groups, the individual spine suspensions can be assumed to be quite soft relative to the ankle, and so the constraints are relatively unaffected in most cases. The exceptions to this are the load-sharing constraints in the Loaded state. To share the load between spines, the particular force-displacement characteristic is very important to keep the loading vectors parallel and permit motions in the y-direction. In these cases, then, the compliance of the ankle in series with the spine suspension must be taken into account following the approach given in the extended footnote in section 3.1.1. The spine suspensions as a whole will rotate as forces are applied to the spines, and so the net displacements must still satisfy these constraints.

Chapter 4

Real Spine Suspension Behavior

4.1 Introduction

In this chapter we present several spine suspension designs and analytical models of them. We show how these designs satisfy the criteria on the spine suspensions set forth in chapter 3. Recall that these criteria were established for different states of spine loading and unloading:

- Unattached – spines are tracing over the surface in order to engage on asperities.
- Loaded – spines have engaged on asperities and are supporting loads. Constraints in the Loaded state are divided into two categories: load-sharing, which deals with the forces on different spines in a group, and geometric, which deals with physical interactions between the parts of the suspension structure and the wall.
- Re-engaging – spines have slipped off asperities or are otherwise not engaged while loads are still being supported by other spines.
- Disengaging – spines are in the process of being lifted off the surface.

A brief outline of the chapter is as follows:

Section 4.2 describes the real spine suspension designs and analytical models of them that are useful for analyzing the design performance. The section discusses

design decisions and how the designs avoid some practical pitfalls, and shows how the designs satisfy the geometric constraints during the Loaded state and constraints in the Disengaging state.

Section 4.3 shows how these designs satisfy the load-sharing constraints during the Loaded state and constraints in the Re-engaging state.

Section 4.4 quantifies how well the spines do load-sharing, relative to the ideal behavior set forth in the previous chapter.

Section 4.5 discusses extensional load-sharing characteristics of the spines.

Section 4.6 shows time-domain results of the spines attaching to a roofing paper surface.

Section 4.7 discusses how the spines achieve dynamic adhesion—continuous adhesion while sliding over a surface.

Section 4.8 shows how the designs can be modified to better or worse satisfy the constraints during the Loaded and Re-engaging states, using the analytical models.

4.2 Actual suspension designs

In this section, several suspension designs and analytical models of those designs are described. The designs are made to satisfy the constraints on the suspension stiffness matrix during the Loaded state (geometric constraints) and Disengaging state. How the designs satisfy the constraints during the other states will be discussed during subsequent sections.

4.2.1 Design methodology

The overall design methodology for spines is as follows. We assume that around 20% of the spines will attach under worst-case conditions, if the surface has infrequent asperities and is only marginally climbable. The total force the group of spines (e.g., in a foot) must support is estimated, based on e.g. a robot's total weight. The total horizontal width of the group of spines is also assumed, based on the practical space

constraints in the design. For example, on a climbing robot, feet that are too wide can cause the sides of the foot to run into the ground unintentionally if the feet are slightly misaligned with the surface. The width of each spine is also known, based on the available manufacturing methods, so this plus the overall foot width dictates the total number of spines (here we assume a single row of spines). With the total force assumed and 20% of the total number of spines assumed to be attached (at half their maximum deflection, on average), the average k_{yy} stiffness can be computed. Next, it must be verified that the asperities can support this much load per spine; if they cannot, the foot must be made to include more spines, and the load per spine reduced. Following the determination of the stiffness in the y-direction, the k_{xx} stiffness can be computed based on the overall linkage performance and the minimum stiffness to overcome friction effects between adjacent spine linkages.

4.2.2 RiSE and ZMan toe designs

The RiSE toe design was made for use on the RiSE climbing robot [99]. A picture of the RiSE robot climbing a wall can be seen in figure 4.1(left). As shown in figure 4.2(left), the toe consists of a small hardened steel hooks ($\approx 10 - 25\mu$m tip radius) (Tiemco 900BL fish hooks) embedded in a molded structure of hard and soft urethane (Smooth-On Task 9 and Vytaflex 30, respectively) created using Shape Deposition Manufacturing [16]. The system can be modeled as a damped, elastic linkage as shown in fig. 4.2(center).

Figure 4.2(right) shows a ZMan toe, designed for a human climbing application. A picture of the author supported by a patch of 1200 ZMan toes is shown in figure 4.1(right). This design uses the same overall structure as the RiSE toe, except some of the dimensions are different, and it uses the Smooth-On Vytaflex 60 polyurethane for the flexures.

In both designs, the general operation is as follows: rows of these toes are secured to two plates on each end via pins running through the toes. In figure 4.3, the pins are labeled 6, 7, and 8, and the top sideplate is labeled 9. In figure 4.2, pins go through the hole at the bottom of element 2, which acts as a rotational joint, and through the

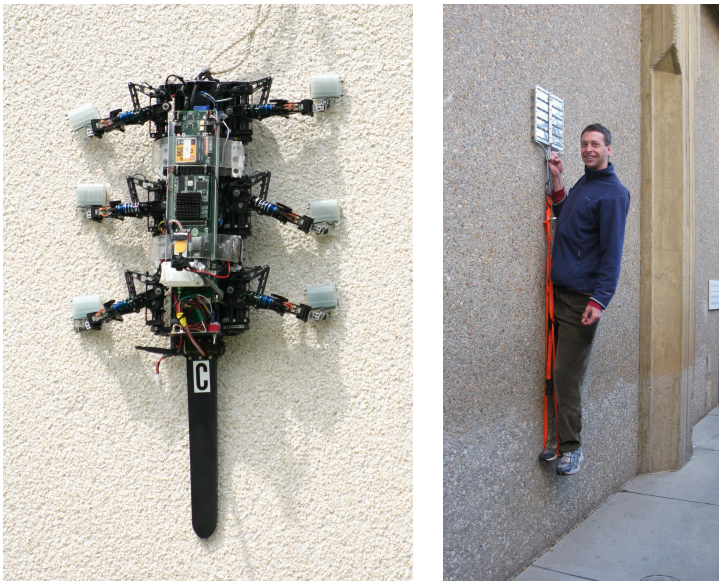

Figure 4.1: (left) Picture of the RiSE robot using the microspines developed in this thesis. (right) Picture of the author hanging from a large patch of ZMan spines.

hole in the rigid material at the end of flexure 5. A third pin, element 6, restricts the motion of the front of the toe in conjunction with the hole in element 1. Flexure 5 is quite soft, while flexures 3 and 4 are relatively stiff in both extension and bending.

As the spine is preloaded in the x-direction, element 1 deflects backwards, rotating about the pin in element 2 (labeled 7 in figure 4.3). Then, as shear loads are applied, flexures 3 and 4 stretch, and further rotation may occur. The combination of rotation and stretching gives the linkage a nonlinear characteristic, as well as bringing the base of the spines towards the wall as it is loaded, for certain combinations of flexure stiffnesses. With appropriate stiffnesses for the flexures, this makes it a good suspension for effective load-sharing during the Loaded state and makes it exhibit appropriate behavior during the Re-engaging state.

When set up between the side plates, flexure 5 is stretched to have a preload force. This causes the toe to rotate forward, except the pin (element 6) through the hole in element 1 prevents forward rotation, and the combinations of flexures 3 and 4 does not permit bending. In this manner, there can be a preload on the spine tip in the x-direction. This overall mechanism can be made to have a very small k_{xx}

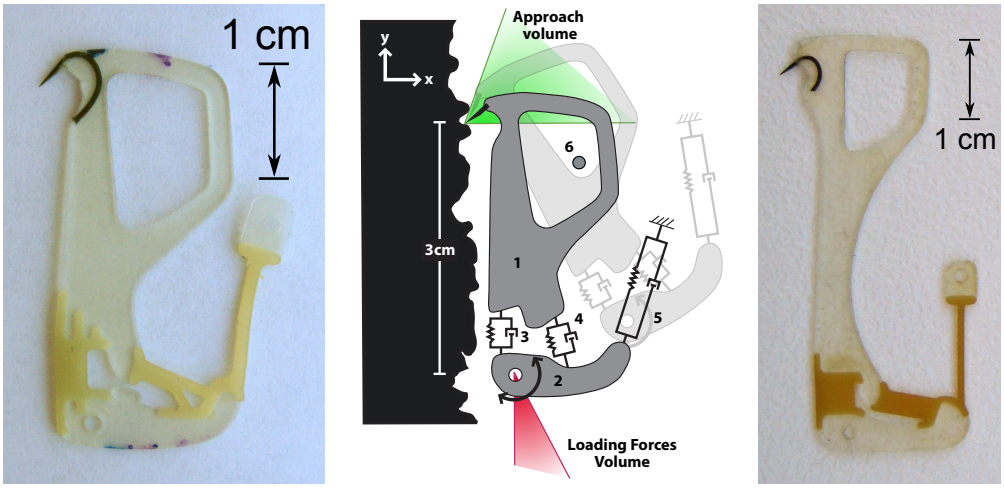

Figure 4.2: (left) Picture of a RiSE toe. (center) Spring/damper model of spine linkage. The spring elements 3 & 4 contribute to the tangential compliance (k=184 N/m for 3 & 4 in parallel, b=0.42 Ns/m), while element 5 provides compliance normal to the wall (k=16 N/m). Element 6, a pin going through the entire foot, acts as an overload protection mechanism in conjunction with the hole in element 1. The approach volume is mostly a function of the shape and orientation of asperities; the loading forces volume also depends on the coefficient of friction. (right) Picture of a ZMan toe, which uses the same general design as a RiSE toe but with different lengths and stiffnesses.

compliance, because flexure 5 is operating in extension rather than compression.

Flexure geometry

The flexures at the back of the spines (elements 3 and 4 in figure 4.2(center)) are designed to accomplish two goals. First, we wish to avoid clockwise rotation of the plastic piece that the spine is embedded in (element 1 in figure 4.2(center)), because if it rotates too far then it will hit the wall, as discussed in section 3.3 about suspension-wall constraints. By angling flexure 4 steeply, this motion can be reduced, satisfying the geometric constraints during the Loaded state. In the ZMan toe, the short-and-wide aspect ratio of the flexures aids with this effect.

Second, by adjusting the spring constants and locations of flexures 3 and 4, the rigid element (2) connected to the normal compliance flexure (5) can be made to

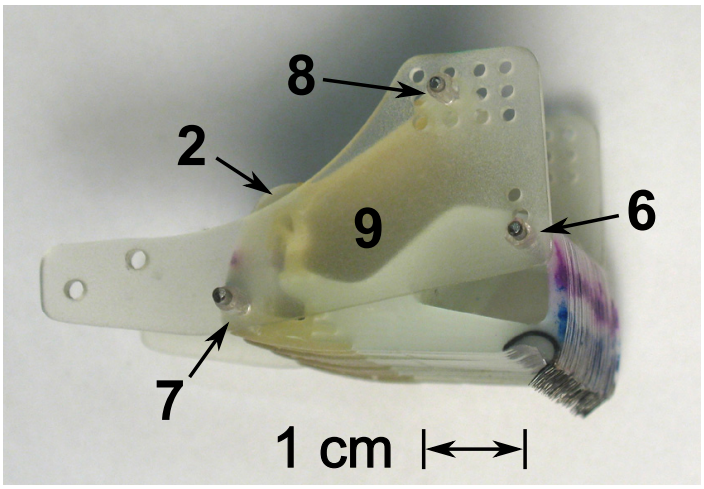

Figure 4.3: View of a group of RiSE toes assembled into a "foot." Numbering is the same as in figure 4.2. Pins 6, 7, and 8 go through all of the toes in the group, and are supported on the ends by sideplates (element 9). The toes rotate around the hole in element 2, which pin 7 passes through.

rotate about the pin at the base as the spine extends. The flexures are designed so that when the spine extends, element 2 rotates forward (counterclockwise), reducing the tension on the normal compliance flexure (element 5). This reduces the effective k_θ spring constant, which makes the spine not push against the wall as much. This has the desirable effects of improving load-sharing and self-re-engagement, while still allowing effective tracking over the surface while the spine is not extended and has not yet found an asperity.

Finally, the steep angle of flexure 4 helps keep the toes aligned properly and from rotating about the y-axis. The toes are in rows, and can easily become tangled unless countermeasures are taken.

At the ends of the flexures in both the ZMan and RiSE toes, the soft polyurethane extends along the edges of the hard material. This was done to reduce stress concentrations between the hard-soft material interface and help prevent delamination at the edges. Furthermore, on the RiSE toe, fingers of soft polyurethane can be seen extending into the hard material at the ends of flexure 3. If a straight interface was used at this linkage, the soft polyurethane exhibits delamination in the middle of

the interface. A fingered geometry was not necessary on the ZMan toe because of the greater similarity between the hard and soft polyurethane Young's moduli, as compared to the RiSE toe.

Overload protection

The spines are equipped with an overload protection system consisting of a hole in the plastic piece connected to the spine with a pin passing through it (elements 1 and 6 in figure 4.2(center). This system accomplishes several goals.

First, it facilitates disengagement of the spines. When the spines and linkages are lifted off the wall, sometimes the spine tip can become jammed into a small crevice on the surface, as discussed in section 3.7. In this case, to remove the spine a force must be applied that is parallel to the spine, and away from the wall. The pin-in-hole mechanism accomplishes this by preventing the spines from rotating forward after the pin hits the top of the enclosing element. At this point, the toe will maintain its orientation, so forces can be applied at the base of the spine in the appropriate direction to make the spines disengage. This satisfies the constraints in the Disengaging state.

Second, it prevents the spines from tangling. Because the spring force pushing the spine towards the wall is very weak (controlled by element 5 in figure 4.2(center)), the spines can move in the x-direction relatively easily. Furthermore, the spines can extend parallel to the wall when they are loaded. Without a mechanism preventing tangling, toes will frequently become disengaged due to slipping off an asperity, and then spring back such that their spines get stuck on top of an adjacent spine's suspension, so that it is not able to touch the wall any more. In climbing robot applications, this is very important to prevent because the robots take hundreds of steps, and tangles can accumulate.

Third, it prevents damage to the extensional flexures (elements 3 and 4 in figure 4.2(center)). The flexures are made of polyurethane with a tear strength of $13660 N/m$, and elongation at break of 1000% [97]. If a surface does not have many asperities, leading to only a few toes attaching, or if excessive force is applied to a

foot, then without overload protection many spines will extend beyond their maximum elongation, leading to ripping.

Spine shape

The fishhooks used in the spines are Tiemco brand, model 900BL, size 14, made of steel covered in a black coating. These fishhooks work well because the tip geometry and the hardened steel material resist bending. Even with these fishhooks, the very tips of the spines are still subject to dulling and bending. The dulling is avoided partially because of the spine trajectory during disengagement: the spines typically scrape upwards along the wall for a short period of time before disengagement, which serves to "file down" the tips and resharpen them. Pictures of a new spine tip, one dulled from heavy use, and a spine with a bent tip are shown in figure 4.4.

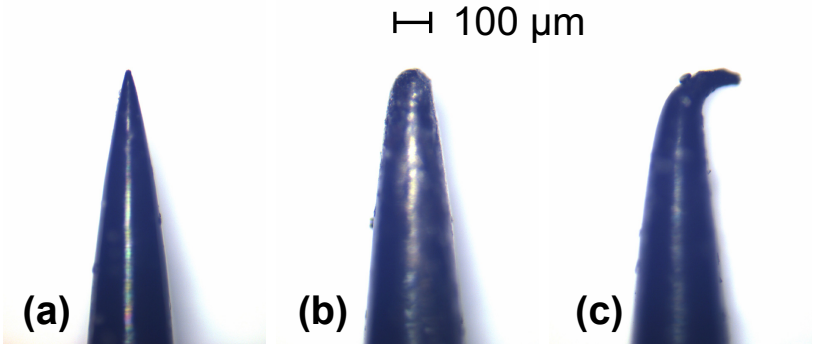

Figure 4.4: Pictures of spine tips: (a), a new spine, with tip radius 7.5μm, (b), a spine extremely dull from use, with tip radius 53μm, (c), a new spine bent at the tip.

The fishhooks are of constant diameter, with a taper near the spine tip. Even though they are constant diameter, bending at the base (where stress is a maximum, per Appendix A.1) does not occur because they are of a sufficiently large diameter for the applied loads. The spines do bend at the very tip, though, because there the fishhooks become more slender than they should be for the applied loads. The spines' bending at the very tip can be eliminated by an improved geometry: an optimal shape for the spines is a logarithmic spiral, which has constant stress along its length when it is subjected to a load at the end [69]. The claws of bears, tigers, and birds were

found to follow this shape [69, 25].

Stalk length l_0

Let the distance from the rotational hole at the back of the spine in element 2 to the tip of the spine be defined as l_0. On the RiSE toe, this distance is 3.0cm, while on the ZMan toe it is 4.6cm.

Changing l_0 has a practical effect because to avoid the constraint of the base running into the wall, the base must be a certain distance away from the wall. In practice, the RiSE spines can displace 8mm in the normal direction, so the base of the spines needs to start at least this far away from the wall. Also, the spines rotate about the bar at the base. To make the structure strong, the material around this bar must extend approximately 1-2mm below the bar. This means the bar must start approximately 9-10mm away from the surface.

A competing constraint is that the θ_0 angle should not be too large, or else the suspension properties suffer, as discussed in section 4.8.1. Together, these requirements mean there is a practical lower bound on the overall spine length. For a travel in the normal direction of 8mm, this corresponds to a minimum length of a few centimeters, or close to the length of the RiSE toes.

4.2.3 Stalk Model

We have developed a simple model that simulates the behavior of the RiSE and ZMan toe suspensions, and is useful for analyzing what makes a good suspension. The "stalk model" is shown in figure 4.5. It is composed of a pin joint where the spine tip meets the wall, an extensional spring k_{ext} able to extend parallel to the stalk shaft, and a torsional spring k_{theta} at the base of the spine. The base of the spine is connected via a pin joint to a body whose orientation and position are assumed to be controlled by a robot or other mechanism.

The stalk has an initial angle of θ_0 with respect to the wall, and θ_{final} is the final angle after the stalk deflects under a load. The torsional spring can have a preload

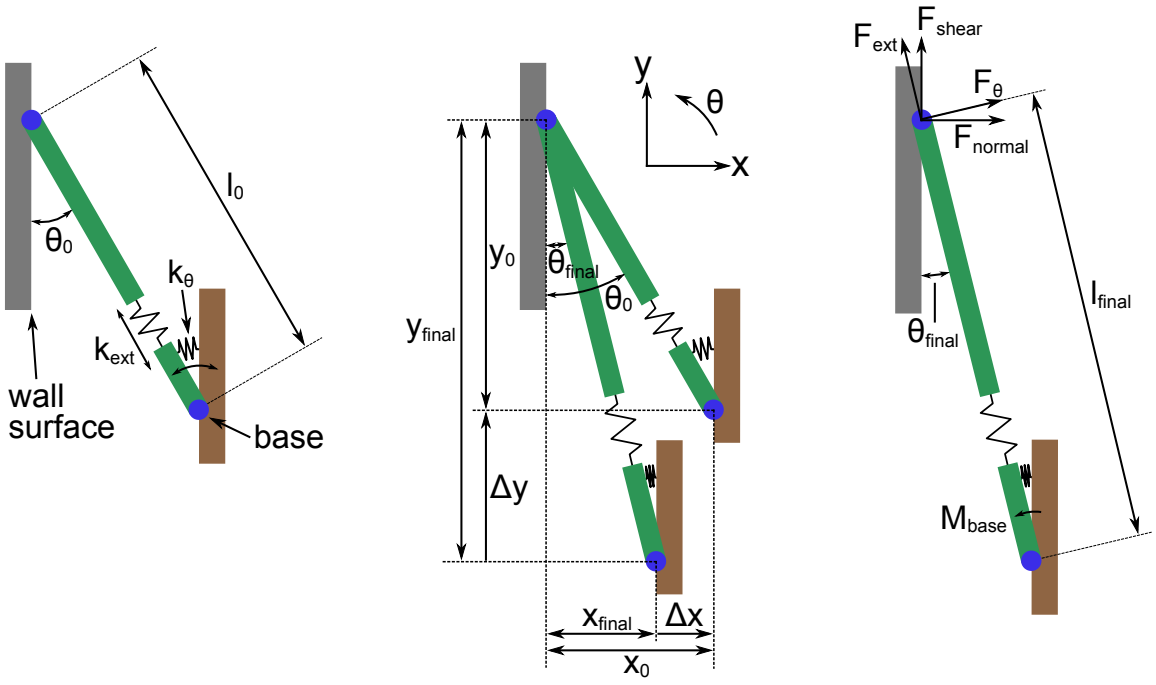

Figure 4.5: Stalk model: pin joints connect a stalk to the wall and the base of the suspension. An extensional spring k_{ext} allows the stalk to stretch, and a torsional spring k_θ causes moments at the base pin joint. The stalk is initially at angle θ_0 with respect to the wall, and is length l_0. After deflection by Δx and Δy, the stalk is length l_{final} at an angle θ_{final}. The forces on the stalk tip can be described by (F_{ext}, F_θ) or (F_{shear}, F_{normal}).

of $\theta_{preload}$, which models how the spines push against the overload protection pin in the resting state.

The stalk, when displaced by Δx and Δy to final positions of x_{final} and y_{final}, has a length and angle of:

$$l_{final} = \sqrt{(x_0 + \Delta x)^2 + (y_0 - \Delta y)^2}$$
$$\theta_{final} = \arctan\left(\frac{x_0+\Delta x}{y_0-\Delta y}\right) .$$

The torsional spring at the base applies the moment

$$M_{base} = k_{theta}(\theta_0 + \theta_{preload} - \theta_{final})$$

and the extensional spring causes a force along the stalk of:

$$F_{ext} = k_{ext}(l_{final} - l_0).$$

The wall end of the stalk experiences forces due to the wall of:

$F_{ext} = k_{ext}(l_{final} - l_0)$

$F_\theta = M_{base}/l_{final}$

which, when put in the (F_{shear}, F_{normal}) coordinate system, equate to:

$F_{shear} = F_{ext}\cos\theta_{final} + F_\theta \sin\theta_{final}$

$F_{normal} = -F_{ext}\sin\theta_{final} + F_\theta \cos\theta_{final}$

To determine the forces required to engage the spines and keep them attached to the surface, an array of 10 spines was tested on a mechanized stage and force plate described in section 2.4 and [90]. Using the results from the stage testing, we can compare the behavior of the stalk model to that of the RiSE toe. To compare the stalk model to the RiSE toes, the following parameters were used:

Table 4.1: Parameters in Stalk Model to match RiSE Toe behavior

l_0	3.0	[cm]
k_{ext}	184	[N m]
k_θ	0.0025	[N m/radian]
θ_0	30°	[degrees]
$\theta_{preload}$	3°	[degrees]

A diagram of the testing procedure is shown in figure 4.6. In testing, the spine base was first moved in the direction normal to the surface a specified preload depth, and then the base is moved parallel to the surface through a specified range of displacements. A rigid bar was mounted on the force plate such that the spines would catch on it as they were dragged horizontally. The trajectory is reversed to return to the starting position. Each line in the plot corresponds to a different preload distance.

To test the linkage, the spines were preloaded in the normal direction to the force plate to various depths. During this time, the spines slid in their non-engaging direction due to their linkage properties. Next the bases of the spines were dragged parallel to the surface. A rigid bar was mounted on the force plate such that the spines would catch on it as they were dragged horizontally across the force plate. After the spines grabbed on the bar, the shear forces and adhesive forces increased

as the spines stretched. To unload the spines, the trajectory was reversed.

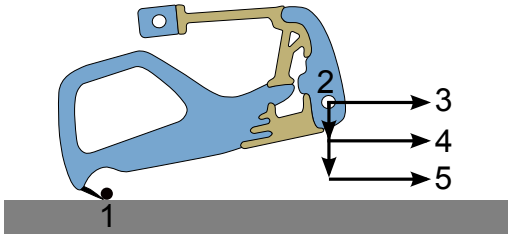

Figure 4.6: Diagram of stiffness testing procedure. The spine was positioned so that the spine was just behind a bar (1) glued to a substrate. Then, the base of the spine (2) was moved perpendicularly to the surface to various preload depths, and dragged parallel to the surface. (3) indicates the end of a drag with zero preload, and (5) indicates the end of a drag with the maximum preload.

Results can be seen in figure 4.7. In this plot, the measured forces from the stage correspond closely to the simulated model, the primary difference stemming from hysteresis in the linkage that was measured. Also, the forces from the stalk model show positive normal forces because the model assumes the spine tip is held in place by a pin joint, while on the stage the spines were allowed to deflect and slide back so as to not be in compression. In summary, the model is a good approximation of the RiSE spine linkage (at least for x- and y-forces, as rotations were not measured on the stage), and thus can be useful in simulating the effect of varying the parameters of the RiSE toe.

4.2.4 Parallel four-bar toe design

Another design, shown in figure 4.8, uses nitinol wires embedded in a hard polyurethane (Smooth-On Task 9) to form elastic four-bar linkages. The wires at location 3, form a parallel linkage that enables the spine, embedded in element 1, to travel vertically in the picture. A deflected location is shown, which results from applying a force F to the spine tip. The wires, from Malin Co., are of diameter 0.381 mm at location 3, and at location 4 are of diameter 0.254 mm. The toe is supported by pins going through one hole in each plastic part labeled 5. This forms two pin joints, so the body of the spine, element 2, can travel horizontally as forces are applied to the

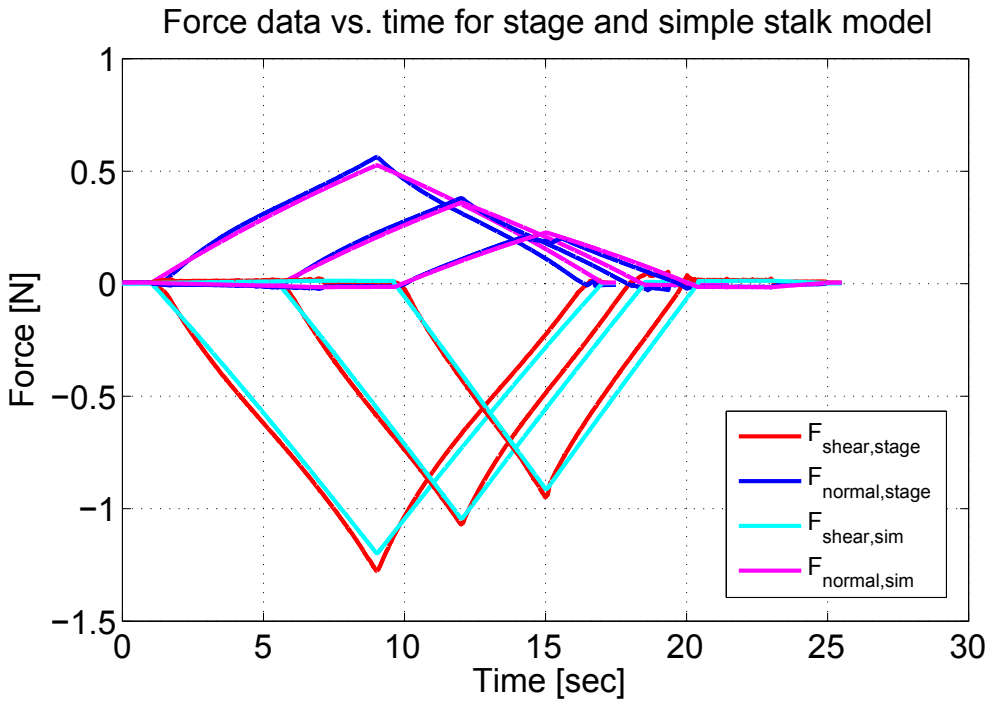

Figure 4.7: Plot of forces from the RiSE toes on the stage and the simulated forces from the stalk model, showing very good agreement. The three different pairs of lines show results for three different preload depths.

spine tip. Wires 4 are very slender, bending easily to allow this motion. Furthermore, because of the arrangement of the wires (one on the top, one on the bottom), the wires are always in tension as the spine tip is loaded, preventing buckling.

This design uses an overload protection mechanism similar to that in the RiSE and ZMan toes. The top part of element 1 is angled, and this runs into a pin in front of it, 6, after a certain deflection. When this occurs, the angled face hitting the pin causes a force pulling the spine away from the wall.

4.2.5 Constant stiffness model

It is also useful to compare the previous spine designs to a constant stiffness matrix. The matrix used in the constant stiffness matrix simulations is following; values were chosen to give the same general behavior as the RiSE toes:

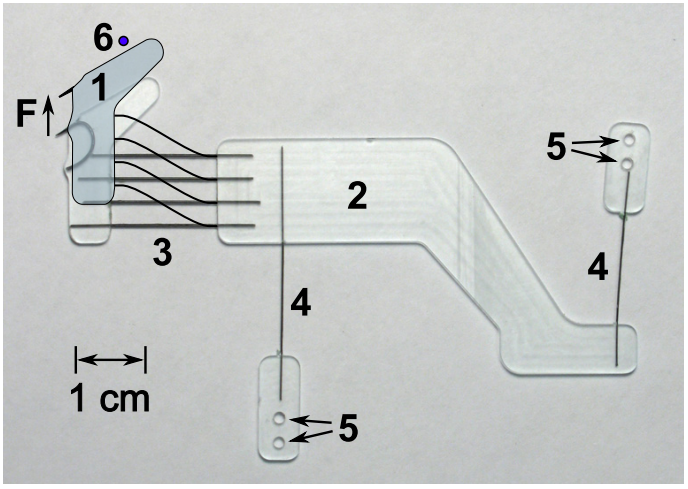

Figure 4.8: Picture of parallel four-bar toe design. Nitinol wires 3 permit the spine, embedded in 1, to move up and down relative to the main body, 2. A deflected position is also shown, which would result from applying a force F to the spine tip. One pin goes through each plastic element labeled 5, acting as pin joints so the main body can move perpendicularly to the surface. Nitinol wires 4 are in tension as the spine is loaded, avoiding buckling. Pin 6 acts in conjunction with the angled face of 1 to provide overload protection.

$$K = \begin{bmatrix} 15 & -30 & 0 \\ -30 & 175 & 0 \\ 0 & 0 & 1 \end{bmatrix}$$

4.3 Comparison of designs: Load-sharing

In this section, we compare three different designs: the ideal linkage for optimal load-sharing, the stalk model, and the parallel four-bar design. The stalk model is a good model of the RiSE and ZMan designs; the parameters used in this comparison were chosen to mimic the performance of the RiSE toes. With this comparison, we conclude that the RiSE toe and stalk model achieve good performance relative to the ideal, although improvements can still be made to more closely match the performance of an ideal linkage.

We compare the load-sharing ability of the different spine suspension designs in the Loaded state by examining plots of the forces on the spine tip as the base position is varied. Recall from section 3.5.1 that the spines in a group are connected together at their bases and thus have the same base distance from the wall. On a typical surface, spines will engage at different y-locations along the surface, but the forces on the spines will all be along the same curve in force-space. As the base is moved parallel to the wall, the forces on the different spines will move along this curve.[1] In the ideal case, these curves will be radial, so the loads on all of the spines will be parallel.

To determine the pattern of curves in force-space for each linkage, the same testing procedure was followed as shown in figure 4.6: the spines are preloaded to different depths and then the bases moved parallel to the surface. The resulting forces are plotted in figures 4.9-4.16, which give the characteristic pattern of curves for each linkage. We will refer to these curves in force-space as "loading lines." Each line in the plots corresponds to a different preload distance. We also calculate the stiffness matrices of the various designs at different stages of loading for comparison. Multiple stiffness matrices are shown because many of the linkages have nonlinear stiffness.

As can be seen from these plots, as the spine base is moved parallel to the surface, different designs have different trajectories through force-space at the spine tip. Figure 4.9 shows the linkage for ideal load-sharing, where the loading lines are radial. The more closely the lines in force-space match the radial pattern corresponding to the ideal suspension design, the better the design is at load-sharing.

Figure 4.10 shows the result using the stalk model, and figures 4.12, 4.13, and 4.14 show the linkage characteristics for the RiSE spine suspension with the spine oriented at different initial angles with respect to the surface. The stalk model matches the results for the RiSE suspension closely. Figure 4.15 shows the linkage characteristic for the fourbar spine suspension. Figure 4.16 shows the results of simulations using a constant stiffness matrix (described in section 4.2.5), for comparison, showing why

[1] This assumes that the differences in engagement locations in the x-direction are very small compared to the differences in the y-direction; if the engagement locations in the x-direction vary a lot, the different spine forces will be on nearby lines.

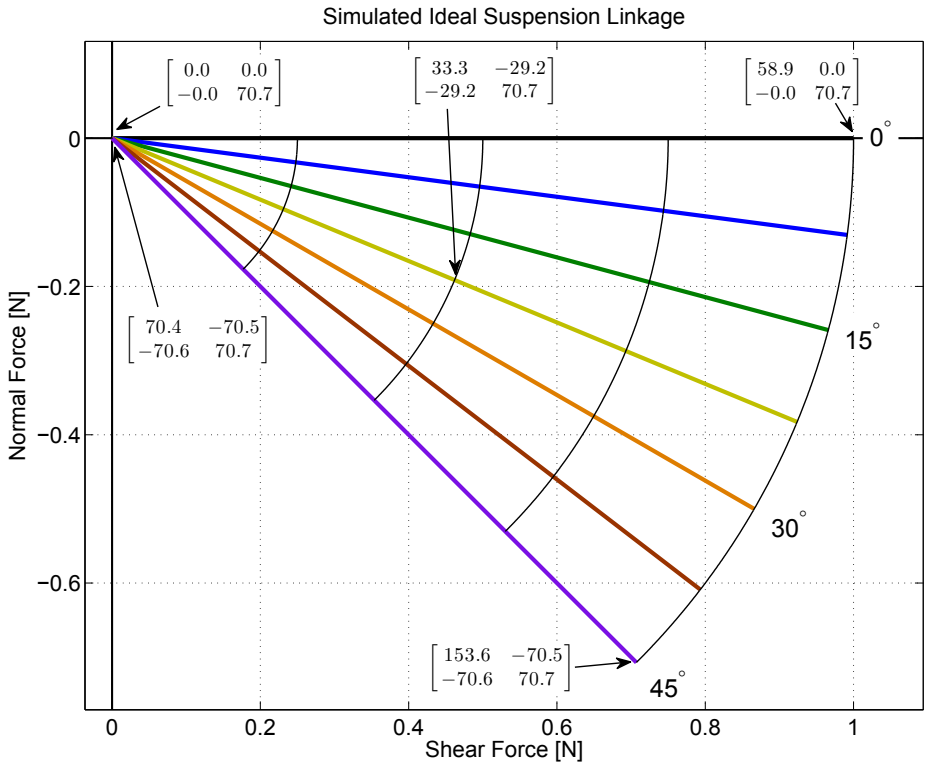

Figure 4.9: Stiffness matrices for ideal suspension. Each line in the figure corresponds to a constant distance between the base of the spines and the surface.

a nonlinear suspension is needed.

4.3.1 Curving up vs. curving down

These different plots show different linkage characteristics. The plots for the RiSE spines show the loading lines curving up towards the F_{shear} axis slightly as the loads are increased, while the fourbar suspension has loading lines that curve down towards the F_{normal} axis. The constant stiffness matrix has straight lines at a constant angle. In general, linkages that curve upwards toward the F_{shear} axis will have better performance than linkages that curve downward.

Consider the case where the load on the base of a group of spines is held at a constant magnitude while the loading angle is increased. This situation can occur if

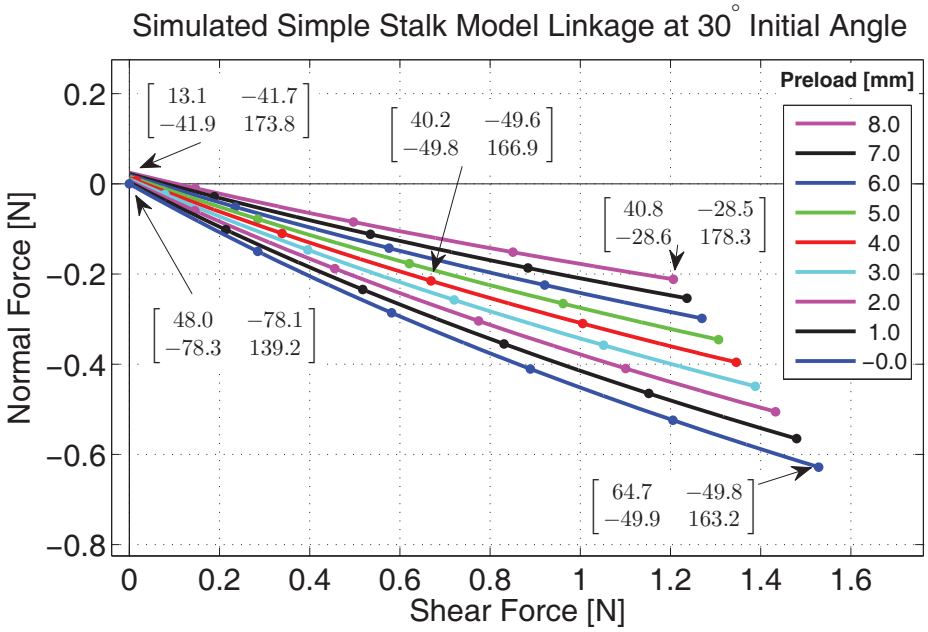

Figure 4.10: Stiffness matrices for stalk model with parameters set to match the behavior of the RiSE toes. Each line in the figure is a constant preload.

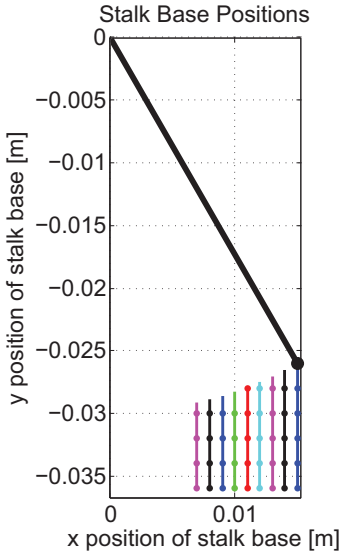

Figure 4.11: Base positions for the stalk model simulation in figure 4.10. The loading lines in this figure are the positions of the spine base corresponding to the same-colored lines in that figure. Dots indicate corresponding locations along these lines.

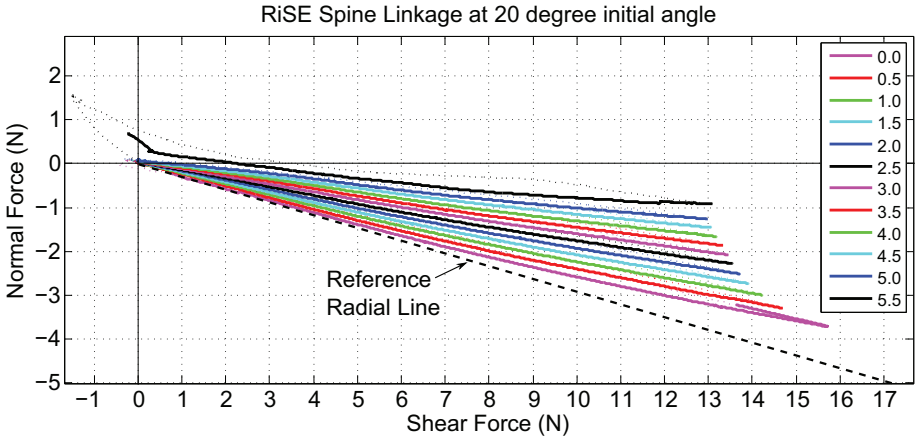

Figure 4.12: Force-space plot of RiSE spine linkage behavior with an initial angle of 20 degrees, for ten spines in parallel. Preloads from 0-5.5mm were applied perpendicularly to the surface, and then the spine base was moved parallel to the surface for 8mm. Each line in the figure is a constant preload.

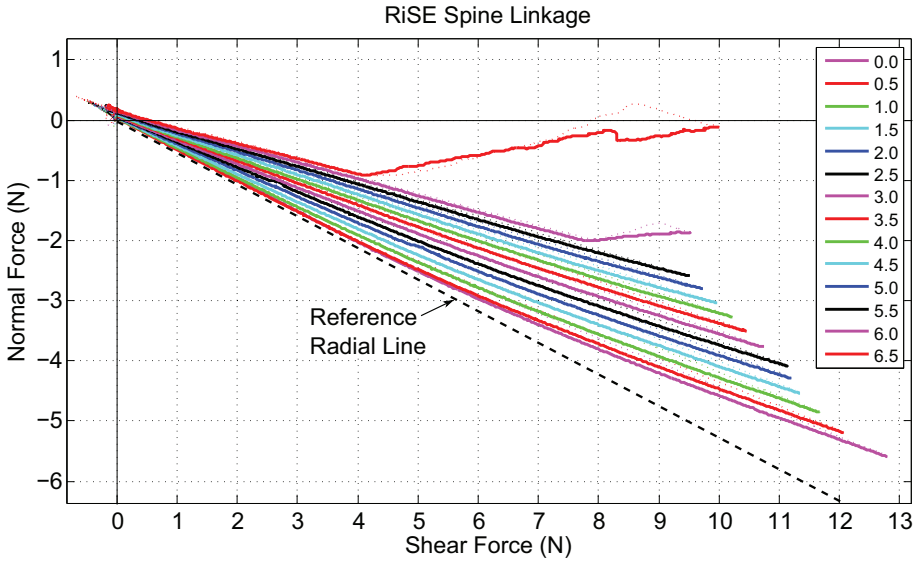

Figure 4.13: Force-space plot of RiSE spine linkage behavior, with an initial orientation of 30 degrees, for ten spines in parallel. Preloads from 0-6.5mm were applied perpendicularly to the surface, and then the spine base was moved parallel to the surface for 8mm. Each line in the figure is a constant preload.

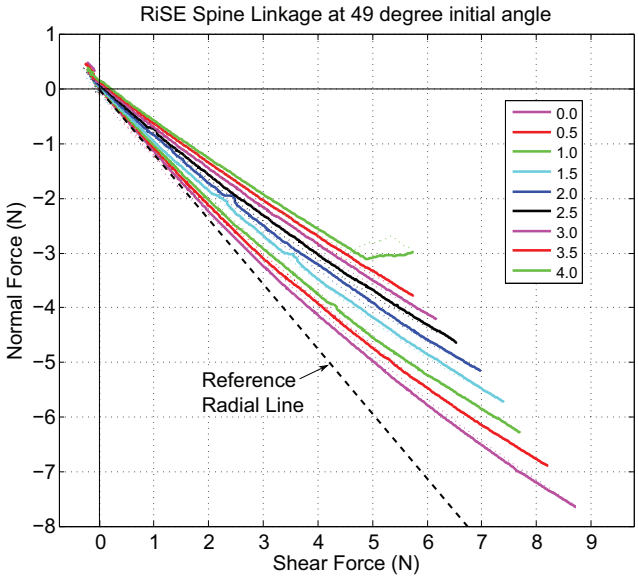

Figure 4.14: Force-space plot of RiSE spine linkage behavior with an initial angle of 49 degrees, for ten spines in parallel. Preloads from 0-4.0mm were applied perpendicularly to the surface, and then the spine base was moved parallel to the surface for 8mm. Each line in the figure is a constant preload.

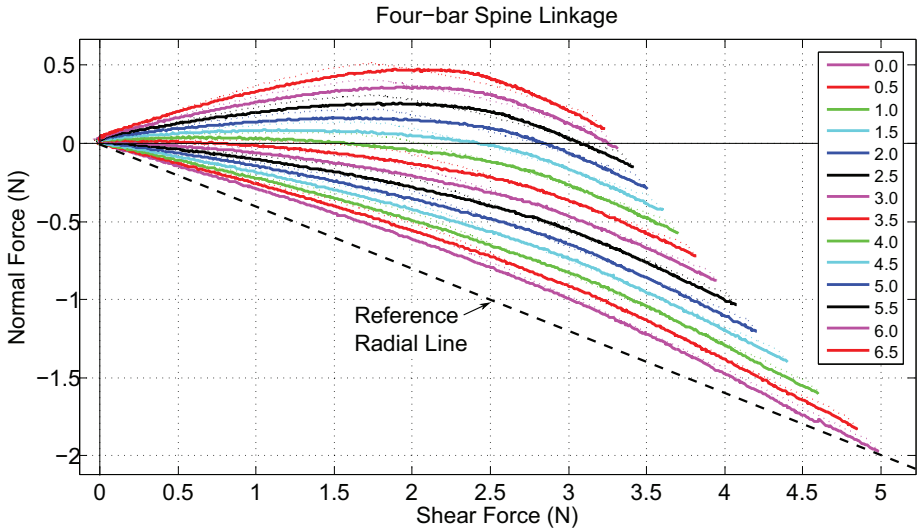

Figure 4.15: Force-space plot of Four-bar linkage behavior, for ten spines in parallel. Preloads from 0-6.5mm were applied perpendicularly to the surface, and then the spine base was moved parallel to the surface for 8mm. Each line in the figure is a constant preload.

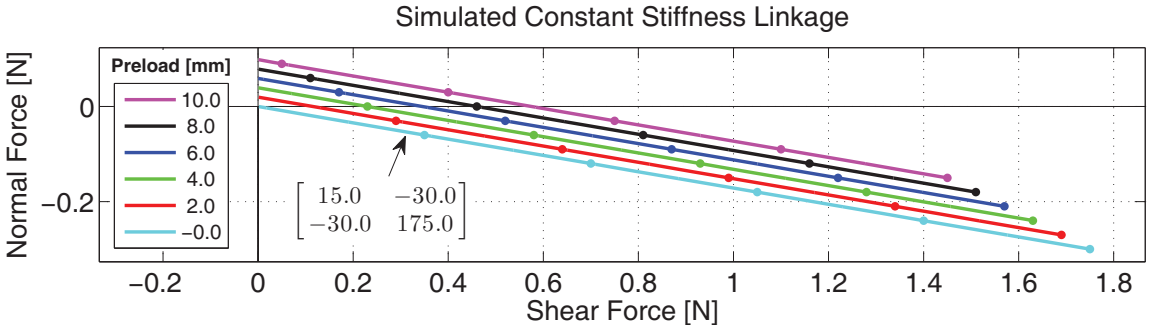

Figure 4.16: Lines in force-space of having a group of spines with the same x-displacement but varying y-displacements, with a constant stiffness matrix linkage. The loading lines deviate significantly from a radial pattern from the origin, illustrating the benefit of nonlinear stiffnesses in the spine suspension.

the spines are pushed into the surface initially, then loaded in shear, and then pulled away from the wall, such as is illustrated in the diagram sequence in figures 3.3- 3.6. This case is useful to consider because this is the pattern of loading used on the RiSE robot [100].

As the loading angle is increased, the spines are loaded increasingly in adhesion. Eventually, some spines will be loaded at angles in excess of θ_{max} for their individual asperities, and they will disengage from the surface. At this point, the spines that remain attached will encounter increased loads as they re-distribute the force previously supported by the spines that just detached.

If the loading lines curve upward, the spines that disengage will more likely be the least-loaded spines. The loads on the spines that remain attached will then increase only a small amount. As long as these spines do not exceed their F_{max} limit, they will stay engaged, an acceptable outcome.

In comparison, if the loading lines curve downward, the spines that disengage will likely be the most-loaded spines. The loads on the spines that remain attached will increase by a relatively large amount. Because the lines curve down, as the still-attached spines re-distribute the load, more spines may be loaded at angles in excess of θ_{max}, causing them to disengage as well. This may cause a chain reaction, leading to all of the spines disengaging.

Furthermore, loading lines curving up toward the F_{shear} axis are good because the true limit curve also curves upward, due to the differences in the magnitude at which asperity failure occurs. This can be seen in the limit curve for roofing paper in figure 2.11. It is useful for the loading lines to mirror the spine/surface limit curve so that as many spines can stay attached as possible. With spines experiencing forces at various locations along a single linkage line, a line parallel to the limit curve will raise the probability that spines will remain attached at both large and small force magnitudes.

4.3.2 Re-engaging performance

If a spine slips off an asperity, it is desirable for the spine to re-engage on another asperity further down the wall. To examine this situation, we consider the force $F_{springback}$ that a spine will experience normal to the wall if it has returned to its original (non-extended) position, while other spines in the group are still engaged and extended.

For the spines to re-engage, the base of the group of spines must be close enough to the wall that an unengaged spine tip can touch the wall again. If the base of the group moves towards the wall a distance x, then an unengaged spine will experience a springback force $F_{springback}$ that results from being preloaded a distance x towards the wall.

This force can easily be determined at different states of loading for the group of spines by examining the foregoing plots of the spine linkage behavior. Because the plots show the forces exhibited by spines as the spine base is held a constant distance from the surface, the normal force on an unengaged spine is simply the F_{normal} force on a particular line at the point where $F_{shear} = 0$. For example, in the plot of the stalk linkage behavior in figure 4.10, the top pink-colored line (corresponding to a preload of 8.0mm) has a preload of 0.04N at $F_{shear} = 0$. If the loads on the engaged spines in the group occur on this line, then any spines that come disengaged will spring back to their original position and experience a preload of 0.04N.

As can be seen from an examination of this figure, the springback forces are quite

small. However, these small springback forces are enough to make the spines re-engage, if they were enough to make the spines engage initially. Larger springback forces occur if the loads on the spines are largely in shear (the top lines in the figure), while smaller springback forces occur as the loads on the spines are more away from the wall.

The plots of the other linkage designs have similar behavior. One additional interesting situation is illustrated in figure 4.17. In this figure, a number of dashed lines are plotted as well as solid-colored lines. These dashed lines correspond to base positions that are far enough away from the surface that unloaded spines will not touch the surface. Spines could potentially still have forces along these lines, if they engaged on asperities and then the base was gradually pulled away from the wall. For these lines, if they were extended all the way to $F_{shear} = 0$, they would correspond to negative values of F_{normal}. This indicates that adhesion would be required for an unloaded spine, and thus the spine would not actually be touching the surface if it were not engaged. Therefore, these lines correspond to regions where self-re-engagement cannot occur.

The foregoing behavior can be observed with the RiSE spines, which have a linkage that curves up. If loads are applied to a group of spines such that unengaged spines cannot re-engage, then to actually achieve re-engagement the spine base must be moved closer to the surface, corresponding to making the force on the group more in shear. In practice, if spines are loaded in this way and some spines disengage, it may be beneficial to completely detach the foot from the wall and re-place it with a pawing behavior. In this manner, the spine linkage characteristics partially dictate the necessary control strategies for engaging the spines.

4.3.3 Accomodating both shear and adhesive loads

In the figures showing the linkage characteristics (figures 4.9 - 4.16), for all of the linkages except the ideal suspension, the loading lines corresponding to the different preload values do not extend all the way up to the $F_{normal} = 0$ axis or all the way down to some regions of force-space at high loading angles close to the θ_{max} limit.

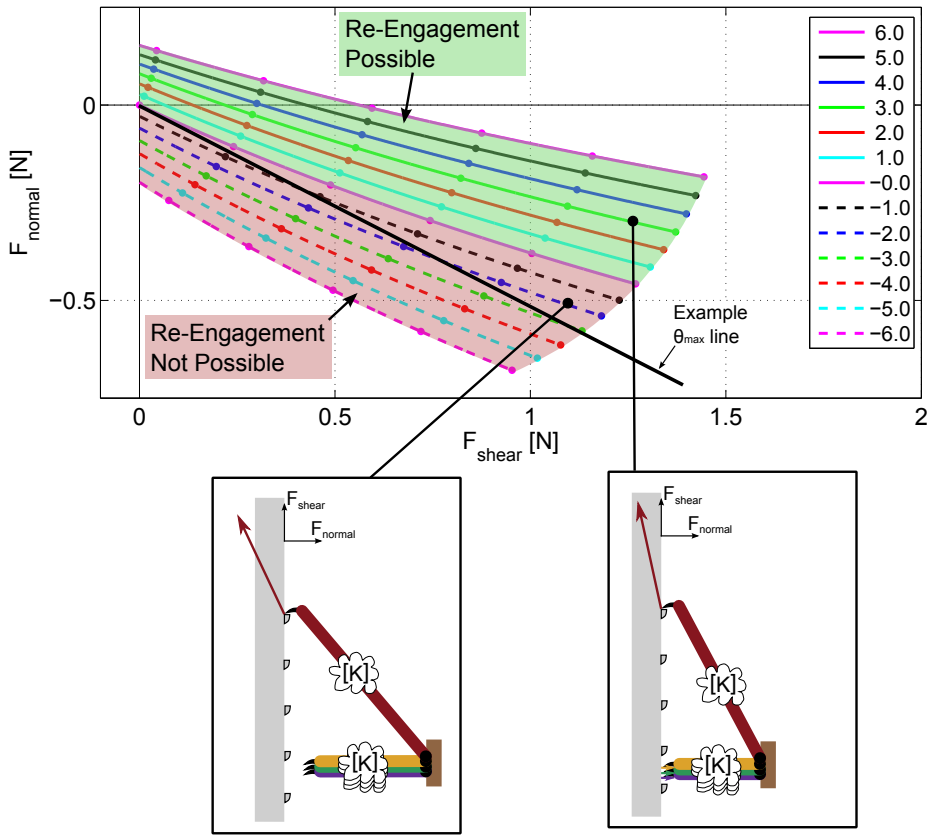

Figure 4.17: Regions of force-space showing where re-engagement is possible: if the loading lines intersect the F_{normal}-axis at negative F_{normal} values, re-engagement will not be possible because the spines will not touch the surface.

For example, figures 4.12-4.14 show the performance of the RiSE spine linkages at different initial angles. If the initial angle is set to 20°, the RiSE spine linkages can generate loads only in the range of around $4 - 14°$. If the initial angle is set to 49°, the linkages can generate loads only around $26 - 43°$.

The linkages can only generate small ranges of loads because the overload protection pin limits the angles to which the spines can rotate. In these graphs, the spines were loaded so that the overload protection pin did not hit its enclosure. Forces close to the $F_{normal} = 0$ axis or θ_{max} limit are indeed possible, but to achieve these forces the overload bar must run into the surrounding plastic. This will cause the forces to be whatever is necessary to achieve static equilibrium, but the linkage performance

will be altered.

One example in which the overload protection pin ran into the surrounding plastic is figure 4.13. In the measurements for this linkage, at high preloads (6.0 and 6.5mm, corresponding to the top two lines in the figure), the bar ran into the bottom of the surrounding plastic. This caused the spines to be pushed into the surface, and the forces on the spine tip to be much more in shear. A similar effect would occur if the overload protection bar ran into the top of the enclosure while the spines were pulling at large angles, except this limit would cause increased normal force rather than shear force.

The overload protection bar running into the surrounding plastic achieves the desired forces for an individual spine, but at the expense of load-sharing. If a group of spines is engaged, the positions of the spines will be slightly different in the normal (x) direction, and very different in the shear (y) direction. Consequently, one spine will be sticking up or down further than the others. When the overload protection pin reaches the limit of the enclosure, it will then typically contact one spine suspension before the others, causing the loads on that one spine to be very different from the other spines, and probably causing that spine to disengage prematurely.

To solve these problems, an ankle can be included between the group of spines and the robot body or climber. On the RiSE climbing robots, an ankle that acts like a pin joint with a torsional spring around it is positioned behind the spines, as shown in figure 4.18. This ankle permits the spine linkages to change orientations with respect to the wall as the load is varied; as the orientation changes, the regions of available displacement change as well. The inclusion of an ankle permits full coverage of the force-space without the adverse effects of the overload protection bar running into the enclosing plastic. A plot of the loading lines for ten RiSE toes on the ankle is shown in figure 4.19. In the range tested, the spines can support loads from 7-23° at maximum extension; larger angles can also be supported, if the spines are engaged and then the ankle is pulled further away from the wall.

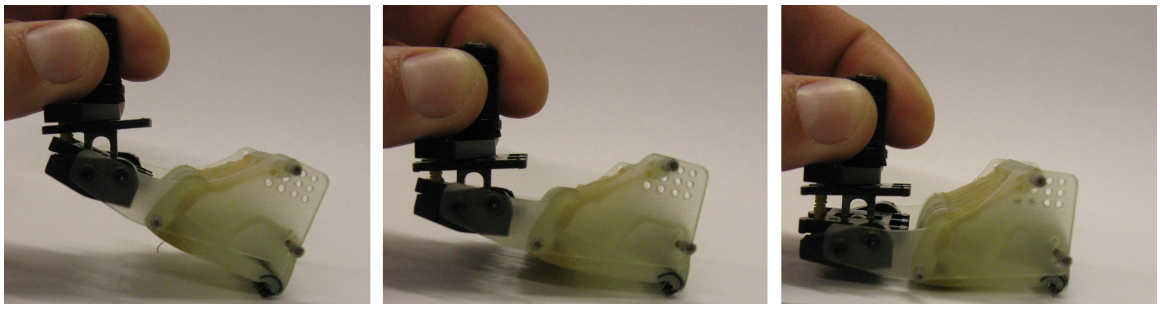

Figure 4.18: Ankle attached to a group of RiSE toes, showing how it permits deflection to different angles with respect to the surface.

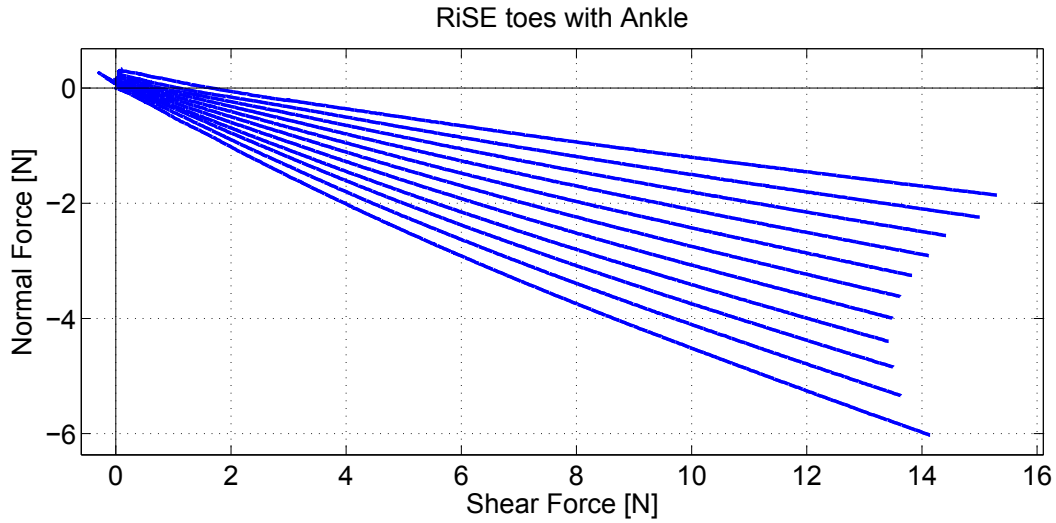

Figure 4.19: Linkage performance for ten RiSE toes attached to an ankle, showing an increased range of possible angles as compared to RiSE toes in isolation.

4.3.4 Strategies for control

The asperities on a given surface will have a wide range of maximum loading angles θ_{max}. A spine sliding over the surface will encounter different asperities as it slides, each of which has a different maximum loading angle θ_{max} drawn from this distribution. While we can generate adhesion by attaching to any of these asperities, if we are selective about which asperities we attach to, we can increase the capacity of the spine/asperity contacts to support normal forces. In other words, we would like the spines to attach to the asperities with maximum loading angles as large as possible.

This will allow the spines to sustain loads at angles as far away from the wall as possible: each asperity can support loads at angles up to $\theta = \theta_{max}$. If the spines initially engage on asperities with small θ_{max} angles, they will easily disengage as adhesive loads are applied, and may skip over asperities with larger θ_{max} angles before re-engaging. Therefore, performance is increased if the spines slide off asperities with small θ_{max} angles during loading, and only cling to asperities with high θ_{max} angles.

Strategies for accomplishing this involve both the spine linkages and the loading trajectory. In the case of an ideal linkage with radial loading lines, the group of spines could be preloaded as little as possible and pulled away from the wall, so that the forces were initially close to some desired angle $\theta_{max,desired}$. If the forces are maintained at $\theta_{max,desired}$ for small magnitudes, the spines will slip off any asperities with smaller θ_{max} angles. Thus, the spines will only engage on asperities with large maximum loading angles $\theta_{max} \geq \theta_{max,desired}$. Later, with larger loads, the direction of forces could be controlled to be at shallower angles if desired.

In practice, however, a group of spines is preloaded into the wall before being dragged down the wall, in order to overcome friction between adjacent spines and conform to the wall. Because positive normal force is applied, spines may attach to asperities with shallow angles. In this case, it may be appropriate to have a spine linkage characteristic with loading lines that curve upward. Then, at small loading magnitudes, the spines will pull away from the surface and slip off low-θ_{max} asperities. At large loading magnitudes, the spines can be operating in a region of the linkage where the loading lines are flatter. In this manner, linkages with lines that curve up may be beneficial.

4.4 Quantifying linkage Load-sharing performance

The focus of this section is quantifying the load-sharing performance of different linkages. If a linkage is non-ideal, we wish to determine the effects on the resulting limit curve, and how much adhesion is lost on account of the non-ideality.

For spines $i = 1, ..., N$, with forces $F_i = F_1, ..., F_N$, the total force on the group is

$$F_{total} = \sum_{i=1}^{N} F_i.$$

If the ideal linkage corresponds to a radial line at the very edge of a limit curve with maximum loading angle θ_{max}, the corresponding forces are

$$F_i = F_{shear,i} \cos\theta_{max}\hat{y} + F_{normal,i} \sin\theta_{max}\hat{x},$$

and the total force on the group will also be at an angle θ_{max} with respect to the F_{shear} axis. A non-ideal linkage will have forces

$$F_i = F_{shear,i} \cos\theta_i\hat{y} + F_{normal,i} \sin\theta_i\hat{x}$$

where $\theta_i \leq \theta_{max}$. The total force on the group of spines will be at an angle $\theta_{non-ideal}$ with respect to the F_{shear} axis. The angular reduction of the limit surface due to the sub-optimal spine suspension will then be:

$$\theta_{difference} = \theta_{max} - \theta_{non-ideal}.$$

This is illustrated in figure 4.20. The top left diagram shows forces on a group of individual spines, if the spines have an ideal linkage (red arrows) as compared to an example of a non-ideal linkage (purple arrows). The forces on the individual spines are plotted in force-space in the diagram in the top right. As shown there, if the linkage is ideal, the forces are all at the same angle. The angle shown in the diagram is θ_{max}, corresponding to all of the spines being on the verge of failure for that particular limit curve.

The purple line shows the forces with the non-ideal linkage. In this case, spines 1 and 2 are on the verge of failure, while spines N and N-1 are relatively far from failure. Because some of the forces are away from the limit curve, the total force on all the spines is at an angle $\theta_{non-ideal} < \theta_{max}$ with respect to the F_{shear} axis. The non-ideality in the suspension effectively causes a reduction in the limit curve for the entire group of spines, because it is not possible to pull on the entire group without some spines becoming disengaged.

Figure 4.21 shows simulated data using the stalk model as a spine linkage. Ten spines are assumed to be attached to the wall at spacings of 1mm, with the bottom-most spine only slightly loaded and the top-most spine loaded 1cm in shear, similar to what is shown in the top left of figure 4.20. The angular reduction in the limit

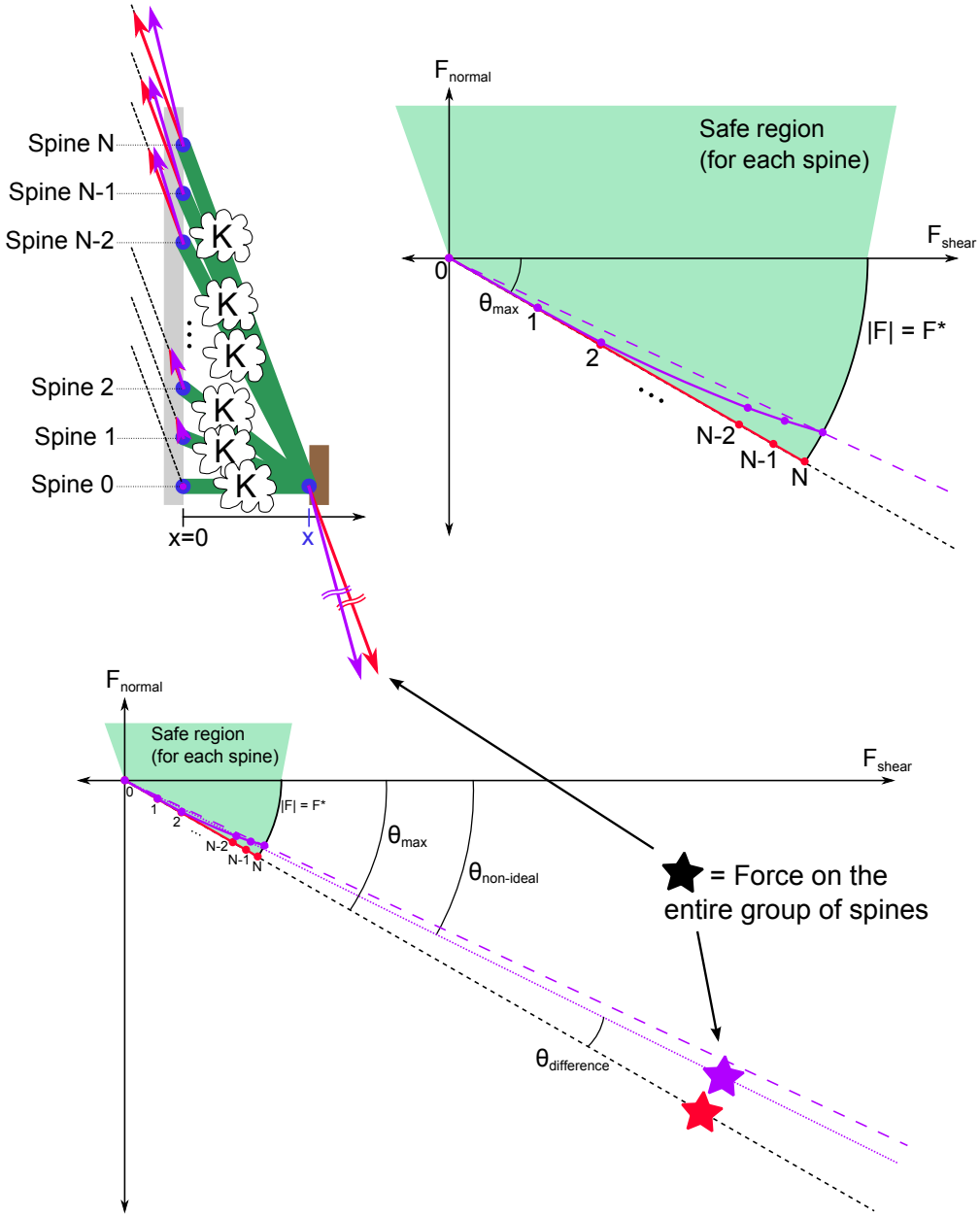

Figure 4.20: Illustration of the reduction in the limit curve caused by a spine linkage non-ideality. The red lines and forces correspond to a linkage able to perform ideal load-sharing, assuming asperities all have the same maximum loading angle θ_{max}. The purple lines and forces correspond to a linkage that is not perfectly radial. In this case, the total load on the group is at a shallower angle than the θ_{max} limit, because if the angle were increased, spine 1 would disengage.

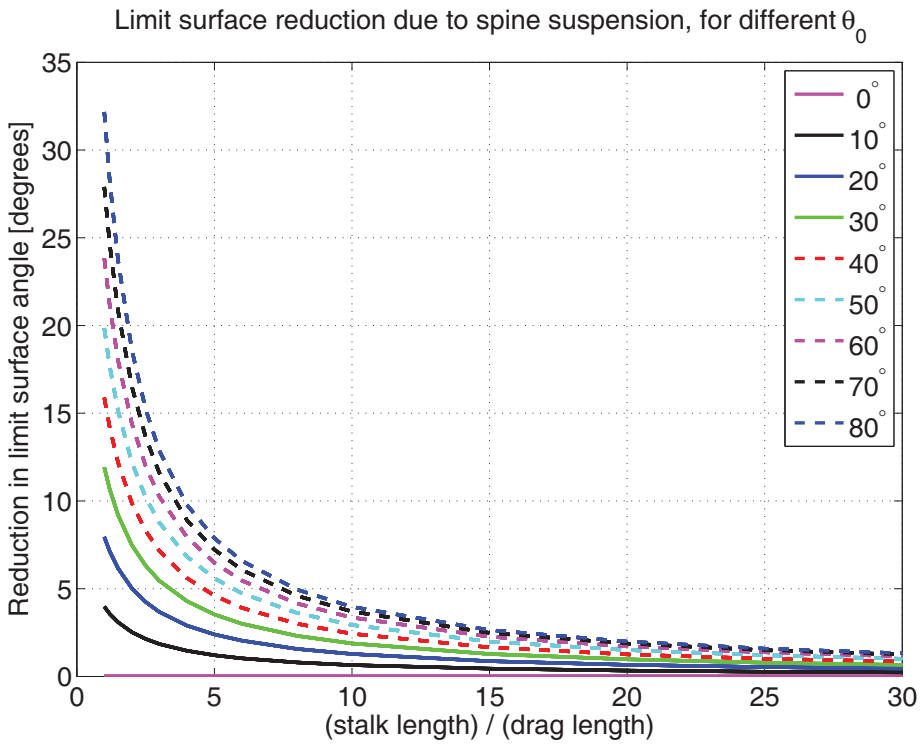

Figure 4.21: Results from a simulation showing the reduction in the limit curve angle due to the linkage non-ideality in the stalk model. Different curves are shown for different θ_0 angles in the model. We assume $k_\theta = 0$ N m/radian and $k_{ext} = 150$ N/m.

surface was calculated for this arrangement and plotted as a function of the initial stalk length. Simulations were done with the stalks at initial angles from $0 - 80°$ at spacings of $10°$, plotted as different lines in the figure.

As the length goes towards infinity, the ratio of $(displacement)/(length)$ goes to zero, causing the angular change to go to zero as well. Consequently, longer stalks will perform better, but suffer reduced packing density due to the increased length, if spines are used in multiple rows. Also, the plot shows that initial angles closer to zero have a smaller reduction in the limit surface.

The simulation done to produce figure 4.21 is a somewhat conservative estimate in the reduction in the limit curve. If the spines had all engaged at the same location instead of being uniformly distributed in the y-direction, then we would not see any

reduction in the limit curve, because all of the spines would be at the same loading angle. In general, the reduction in the limit curve will correspond to the distribution along the wall of where the spines are attached, which will in general be non-uniform. In reality, if the load is increased to an angle $\theta_{non-ideal} + \epsilon$, some spines may disengage, but others will stay attached and take an increased load, allowing the cluster of spines to stay attached. The particular behavior in this regard depends on the force-distance characteristic.

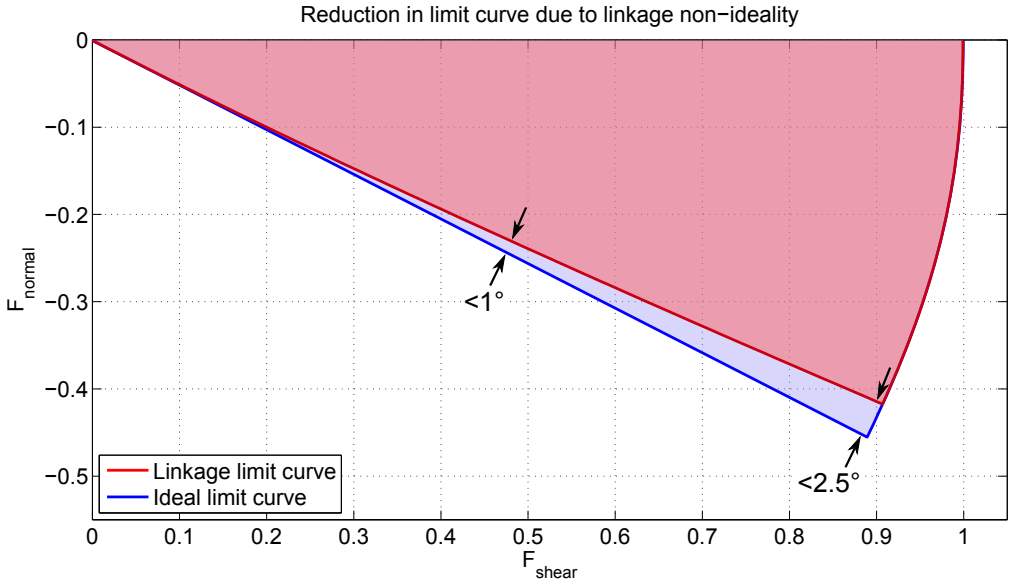

Figure 4.22: Actual reduction in limit curve due to linkage non-ideality for the RiSE toes. The RiSE toes have a loss of less than 1 degree at half the maximum magnitude, and less than 2.5 degrees at full extension.

An estimate of the actual effect on the limit curve with the RiSE toes is computed in figure 4.22 using the measured loading lines for the RiSE toes. To compute the estimate at the maximum magnitude, a similar procedure was done as before. At smaller magnitudes, it was assumed that, at a given angle θ, the spines that exceeded this loading angle disengaged, while the spines that remained attached supported their original loads. Thus, the total load on the group was less than the maximum possible.

4.5 Extensional Load-sharing

To evaluate different suspensions with respect to the extensional load-sharing criterium, simulations were performed using the stalk model. A setup of the simulation is shown in figure 4.23(left). In the simulations, a group of five spines was used on a surface that had five asperities, at locations [0, -1.25, -2.5, -3.75, -5] mm. The base position of the group of spines was moved to different locations. Each spine remained disengaged until the base was moved far enough down the wall that it could attach to its own asperity. For each location of the spine base in xy-space, the forces on the spines were computed. The maximum force on any attached spine was found, as well as the average force among all attached spines, and these were divided to find the load-sharing metric:

$$metric = \frac{\text{(maximum force of an attached spine)}}{\text{(average force of attached spines)}} \tag{4.1}$$

Values greater than 1 indicate that the spine with the maximum force is holding that factor of additional force more than the average. This indicates how well load-sharing is accomplished during the Loaded state.

In the simulation, the stalk model with a typical linear extensional stiffness ($k_{ext} = const$) was compared with a stalk model in which the k_{ext} spring had a nonlinear stiffness. The nonlinear stiffness followed a square root law, shown in comparison to a linear spring in figure 4.23(right).

Simulation results are shown in figure 4.24. The spine base started at (x_0, y_0), shown as a black dot near the top of each plot. As can be seen in both of the plots, the maximally-loaded spine (which is the first spine to attach) is loaded much more than the average load while new spines are first attaching. The extreme case is with the first and second spines: when the second spine just begins to attach, its load is approximately zero, so the average load drops to half of the load the first spine is supporting. In this case the load-sharing metric is equal to 2. Once all of the spines have attached, the average load per spine decreases as all of the spines stretch.

In general, the nonlinear k_{ext} stiffness achieves much better load-sharing than the

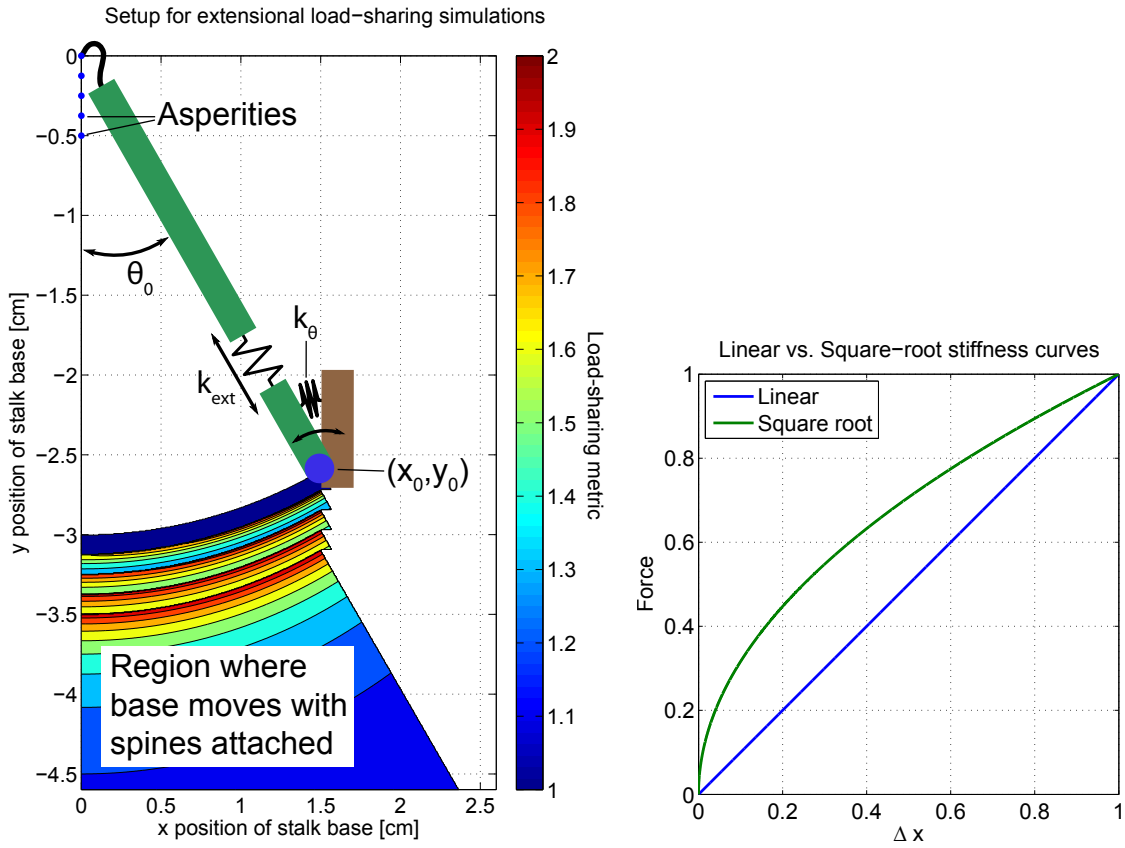

Figure 4.23: Left, setup of simulations involving multiple spines in a row. Spines are assumed to attach at asperities, shown as blue dots. The first spine grabs at (0,0). The base of the group of spines is originally at (x_0, y_0), but is moved to different locations (x, y) in simulation. The load-sharing metric (eq. 4.1) is plotted as a function of the base position. Right, linear and nonlinear (square root) stiffness curves used with the stalk model.

constant k_{ext}. Because the force increases rapidly for small displacements and then becomes more constant with the square-root function, at moderate displacements the forces will be much more equal.

4.6 Measured performance on tarpaper

The spines were tested using a sample of roofing tarpaper, chosen because it has a similar roughness to stucco and is easy to cut to size. A picture of ten RiSE toes

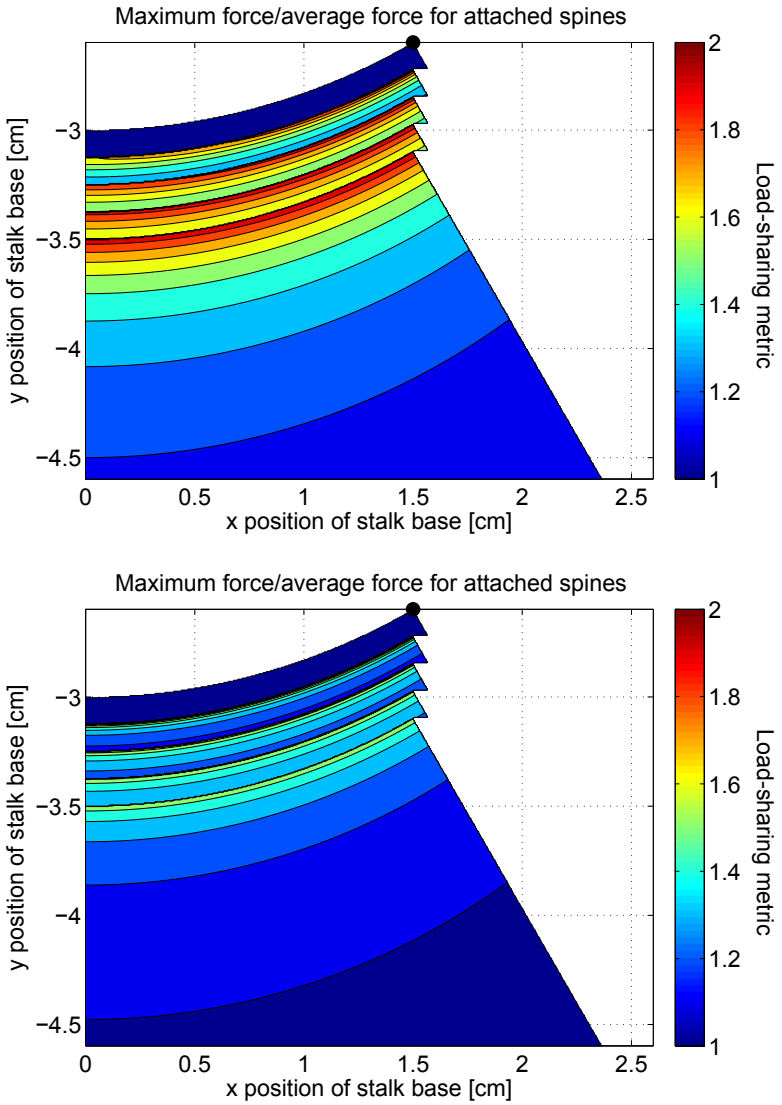

Figure 4.24: Load-sharing metric for the stalk model, with a linear spring for k_{ext} (top) and nonlinear spring for k_{ext} (bottom). The amount of excess load the most-loaded spine is carrying relative to the average load is plotted as the base position is varied. The spine base starts at the position of the large black dot at the top. The nonlinear spring follows a square root function, as shown in figure 4.23(right). Parameters used were: $l_0 = 0.03$m, $\theta_0 = 30°$, $k_{ext} = 184$N/m, $k_\theta = 0.0025$N m/radian.

undergoing testing is shown in figure 4.25.

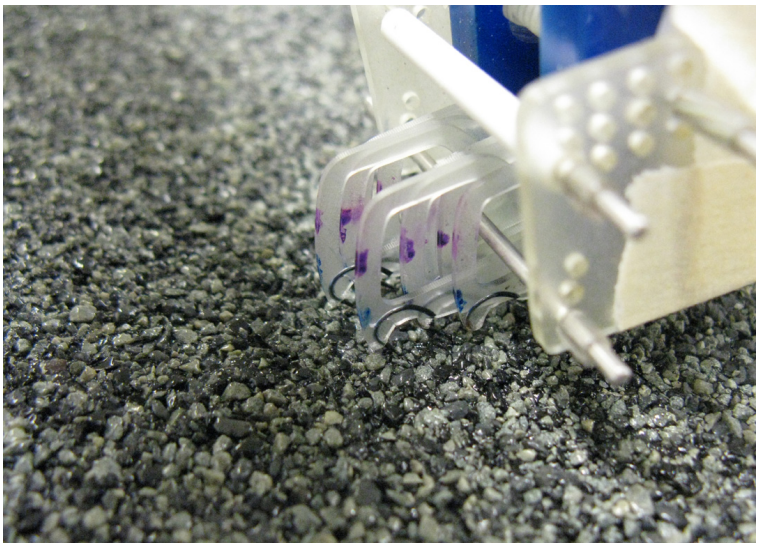

Figure 4.25: Picture of RiSE toes on the tarpaper surface. Several spines are seen to be engaged; two of them are near their limit of travel, while others have recently engaged.

4.6.1 RiSE Spines Time Trace

Results of testing of ten RiSE toes are shown in figure 4.26. In this plot, the blue line (F_{normal}) is the normal force, where negative values correspond to adhesion. The red line (F_{shear}) is the shear force parallel to the surface.

The trajectory used to drag the toes was as follows: the spines were preloaded to a depth of 4mm at a 45 degree angle with respect to the surface. (A preload of 4mm is about half of the working range of the spines.) Next, the spines were dragged parallel to the surface for 16mm, then retracted perpendicular to the surface for 6.5mm, at which point all of the spines had disengaged. The horizontal drag distance of 16mm is further than the extensional range of the spines, around 10mm, so the spines hit their overload protection, disengaged, and re-engaged over the course of the drag.

Figure 4.26 shows this trajectory and behavior as follows. During the preload phase, between the first vertical black line and the cyan line on the plot, the spines

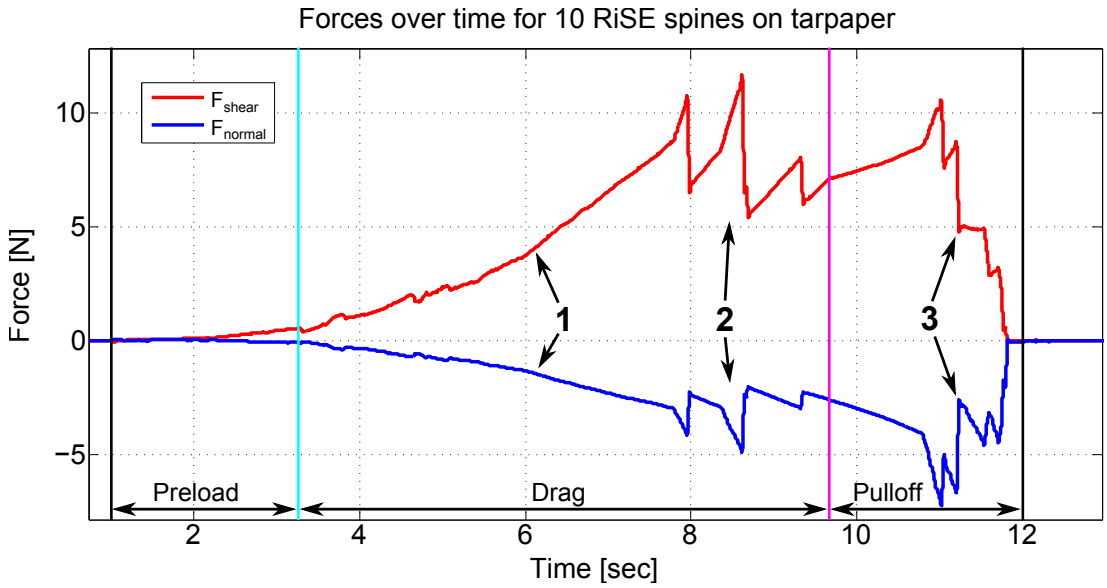

Figure 4.26: Forces over time for ten RiSE toes on tarpaper. The forces increase slowly as the toes are preloaded into the tarpaper. As additional spines engage, the forces increase faster than linearly (1). When the spines reach their overload stop, the forces spike until they disengage (2). During pulloff, the spines again reach a hard limit, and forces increase sharply until the spines disengage (3).

come into contact with the surface almost immediately and then deflect up as their base moves closer to the surface. The positive normal force required before the spines start generating adhesion is almost imperceptible, around 0.04N for a group of 10 spines. The preload force is so low partially because the preload trajectory is angled, facilitating the spines becoming parallel to the surface and beginning to generate adhesion, and partially because the normal compliance of the spine suspension is very low. For comparison, if the spines are preloaded perpendicular to the surface as was done in figure 4.13, the preload is 0.2N for the same group of spines. At the end of the preload phase, a few spines are generating a small amount of adhesion and shear. If we compute the value of μ' from this preload and the resulting 5N of adhesion, we get values of 25 and 125, for preloads of 0.2 and 0.04, respectively. Both of these numbers are larger than the published values for the gecko of 8-16 [8] and are far higher than any values for synthetic dry adhesives.

This property of a very low required preload is extremely useful for climbing

applications. The preload force required is proportional to the number of spines, which can range from between 20-30 spines in a group for robot applications to thousands of spines for human climbing applications (e.g., ZMan). Thus, if 10 spines require 0.04N, the preload forces required for larger numbers of spines can range from 0.1-10N. It is important that the preload forces be as small as possible, because any preload force will require the same magnitude of force in additional adhesion from the other patches of spines that are already engaged. Because the shear force an entire robot or person can generate (due to gravity) is fixed, any additional adhesion required will make the robot or person that much closer to falling because the margin for the engaged spines will be reduced.

During the drag phase, between the cyan and magenta vertical lines, the base is moved parallel to the surface. In this phase, more spines engage the surface while unengaged spines continue to trace over the surface. At the points labeled 1 in the figure, one can see that the slopes of the normal and shear lines increase over time. Because each spine generates an approximately linear increase in force as the base is moved parallel to the surface (see figure 4.7), the slope of a group of spines will become steeper as additional spines engage asperities. Between approximately 6 and 7.5 seconds in the figure, the slope stays approximately constant, indicating that no new spines are engaging.

After the spines have been loaded and stretch, they extend as far as their overload protection permits. At this point, the pin 6 in figure 4.2(left) runs into the hole in element 1, causing the spine to rotate clockwise in figure 4.2 and undergo forces causing disengagement. In figure 4.26, this behavior corresponds to the sudden increase and then decrease in force denoted by 2. The increase in force corresponds to one spine hitting the overload protection and being forced to release. Then when it releases, the force drops sharply, with the change in force corresponding to the amount of force that spine was supporting. At the arrows indicated by 2, two spines can be seen having sudden increases in force then decreasing sharply, at 8 and 8.7 seconds.

During the sudden increases in force, both the normal force and shear force increase, but the normal force can be seen to increase faster than the shear force relative

to the ratio of these forces during normal loading conditions, such as around 6-7 seconds. The overload protection works by prying the spine away from the surface, which increases the normal force until the spine is pulled at such a steep angle that it slips off its asperity.

At 9.3 seconds, another sudden drop in force can be observed, but without a preceding increase in force. This probably corresponds to the surface failing due to a rock particle coming off the surface due to high forces. (Surface failures did occur occasionally in these experiments.) The other possible cause of this spine failure is that the spine slipped off an asperity that could not support that particular loading angle. However, this is unlikely because the RiSE spine linkage causes the loading angle to become more parallel to the surface as the spine base is dragged parallel to the surface, as can be seen in figure 4.10.

During the pulloff phase, between the magenta vertical line and the following black vertical line in figure 4.26, the base of the spines is lifted perpendicularly to the surface. During this motion, the overload protection mechanism again causes the spines to lift off the surface after a maximum deflection, but in the normal direction. At this point, indicated with a 3 in figure 4.26, the normal forces increase until the spines come off the surface. This behavior is similar to that during the end shear phase, except that in the pulloff phase, the spines do not re-engage, so the forces on the group eventually drop to zero. Also, at the end of the pulloff phase, several instances of normal forces increasing with no change in shear forces can be observed, due to the spine base being pulled perpendicular to the surface.

4.7 Dynamic adhesion and re-engagement

Figure 4.27, another plot of the forces over time as ten RiSE spines are dragged over tarpaper, illustrates an additional important phenomenon during the shear phase: dynamic adhesion. Similar to how the gecko can slide across surfaces while maintaining adhesion, as described in [35], the spines also can support adhesion while the base is continuously moving across a surface. This property is relevant to the Re-engaging

state as discussed in chapter 3.

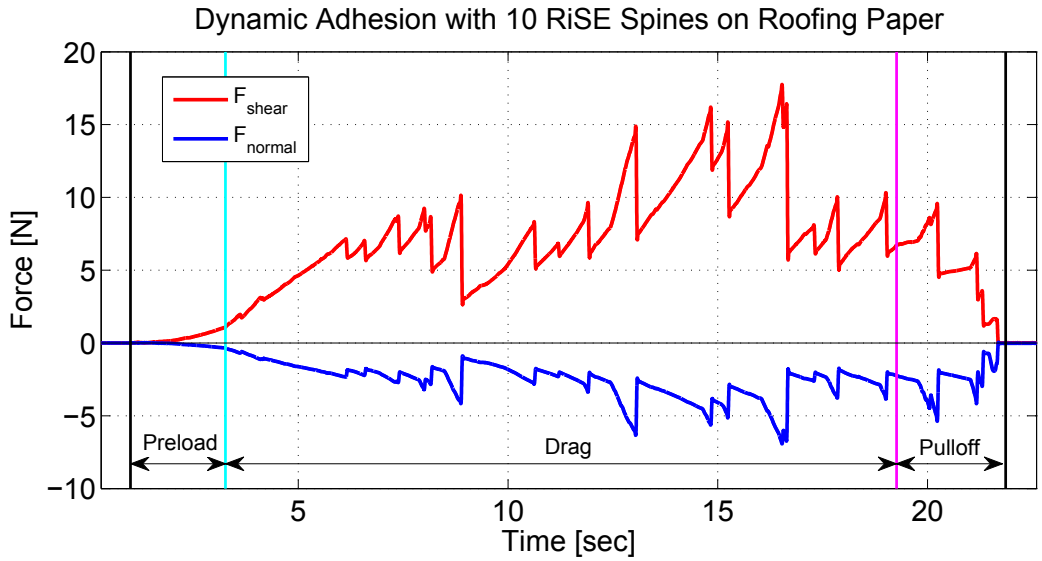

Figure 4.27: Plot showing forces as ten RiSE spines are dragged for four cm across a tarpaper surface at a constant height above the surface. Dynamic adhesion is exhibited, as multiple spines disengage then re-engage over the course of the drag.

To generate figure 4.27, the spines were preloaded to a depth of 4mm and then held at a constant height while being dragged 4cm across the surface. This distance is far longer than each individual spine can stretch before hitting its overload protection, at about 1cm. Although spines disengage when they reach their extension limit, other spines are still engaged and support force. The spines that disengaged can then re-engage on other asperities and support loads as other spines disengage later.

In this trial, the spines maintained a minimum of 1N of adhesion and 2.5N of shear during the drag, although peak forces were sometimes much higher than this. Because adhesion with spines is probabilistic and dependent on the spines encountering asperities with appropriate surface normal vectors, larger numbers of spines will exhibit more consistent adhesion even while sliding.

Figure 4.28 shows the results of four trials with spines dragged over the surface for 6cm. In all cases, adhesion never drops completely to zero, although it comes quite close at times. In these trials, generally 2-5 spines were engaged.

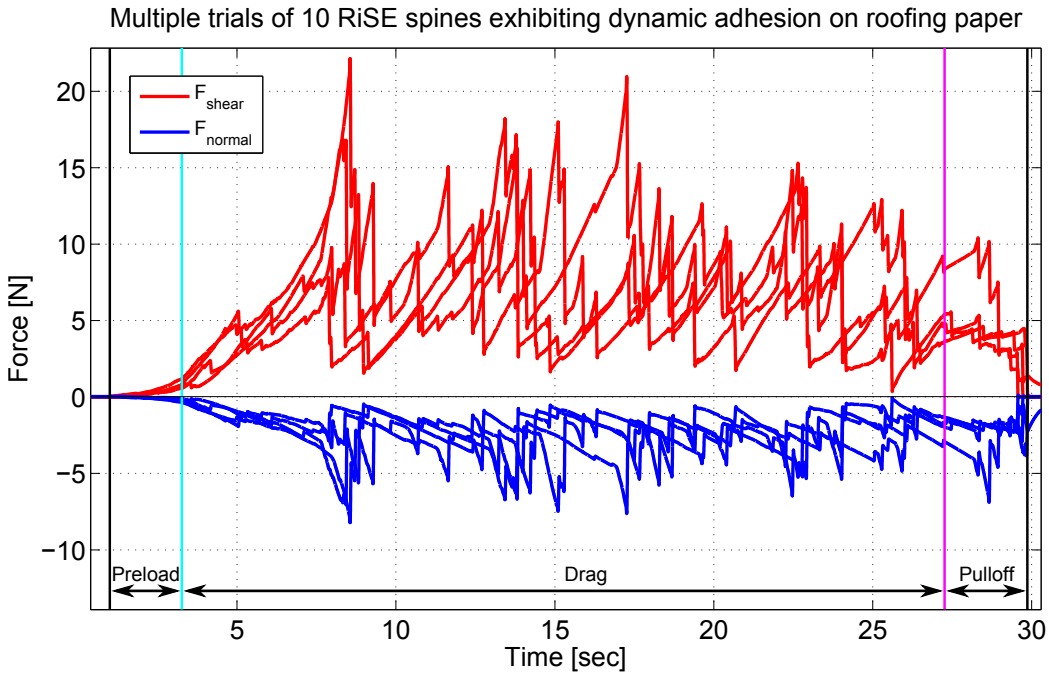

Figure 4.28: Multiple trials of forces over time for ten RiSE toes on a tarpaper surface are shown. The spines were preloaded 4mm, then dragged parallel to the surface for 6cm. In all cases, adhesion increases until spines hit their overload protection, at which point some spines disengage. Dynamic adhesion is exhibited as the spines continue to support loads even as some spines engage then re-engage, while other spines are still loaded.

The property of dynamic adhesion is extremely important for climbing applications, because it prevents slips from being catastrophic failures. On the RiSE robot, the feet slip continually down surfaces during operation, due to local surface failures or disengagement due to erroneous forces (personal observation). Dynamic adhesion permits the robot to stay attached to the wall even as these situations occur.

When the spines disengage, frequently they have been stretched a large distance parallel to the wall. At this point, the extensional flexures are exerting much higher forces on the spine tip than the flexures pushing the spine tip towards the wall. Consequently, the spines typically retract all the way to their original position before re-engaging, as opposed to re-engaging while they are still partially extended.

4.8 Effects of varying parameters with stalk model

In this section, we explore the effects of varying different design parameters, using the stalk model. As shown earlier in figure 4.7, the stalk model is a good model of the RiSE and ZMan spines, so performing simulations with the stalk model can allow us to quickly see the effects of changing parameters in future iterations of the toe designs and determine general trends. Changing the parameters will primarily effect the spines' ability to do load-sharing during the Loaded state and their behavior in the Re-engaging state.

In all of the following simulations, parameters were set to be close to those of the RiSE toes so the results can be interpreted intuitively. The stalk had an initial length l_0 of 3cm. For comparison to the values in the following plots, the RiSE toes have the parameters shown in table 4.1.

In the simulation, the toes were preloaded every 1mm from 6mm to -6mm into the surface. Negative preloads are shown to demonstrate the effects of pulling the base of the spines away from the wall after the spines have engaged. After preloading, the base of the spines was moved 1cm parallel to the surface in the (-y) direction. In the figures in this section, solid lines indicate positive or zero preloads, and dashed lines indicate negative preloads.

A general overview of the simulation can be seen in figure 4.29. In this figure, the top plot shows the forces on the stalk model under the applied displacements, i.e., preloads of 6mm to -6mm, and 1cm downward motion. The bottom plot shows the corresponding displacements of the stalk base, and the stalk itself, indicated by the dark black line (it is shown in its original position). In both plots, dots are plotted on the lines periodically (every 1mm in y-displacement, which is parallel to the wall) so the motion can be better understood.

Figure 4.30 illustrates the linkage motions for a very wide range of stalk preloads. If the spines were permitted to move through a wider range of angles, the resulting behavior would look more like this simulation. Different initial stalk angles will also result in different subsets of the entire range of linkage motion.

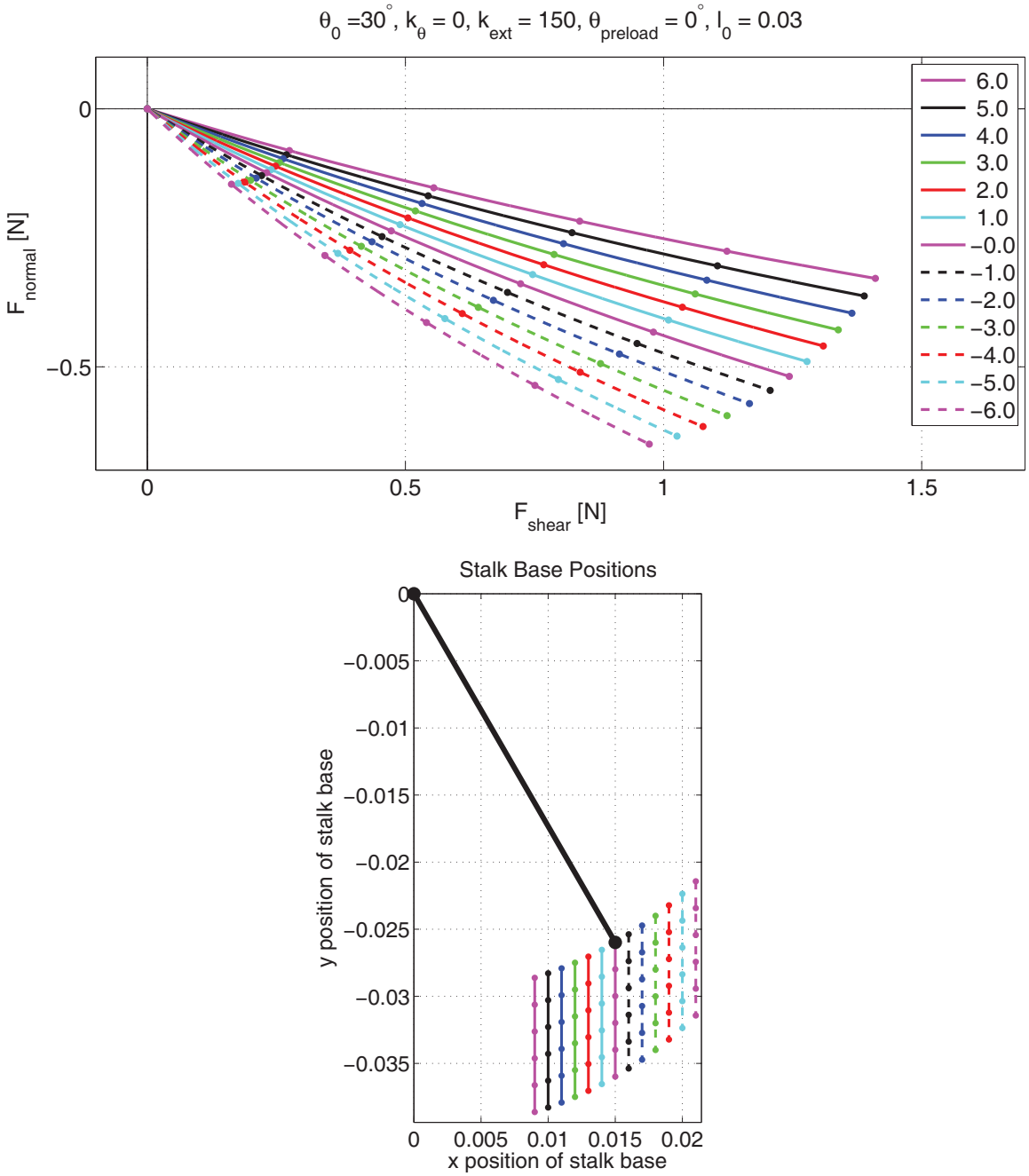

Figure 4.29: Top, example of forces found using the stalk model. Bottom, the base positions where the stalk was moved to generate those forces. The thick black line indicates the original stalk position. In the simulation, preloads from 6mm to -6mm were applied, (negative preloads, with dashed lines, showing the effects of adhesive loads), and the spine base was displaced 1cm down the surface. Dots are shown every 2mm of displacement.

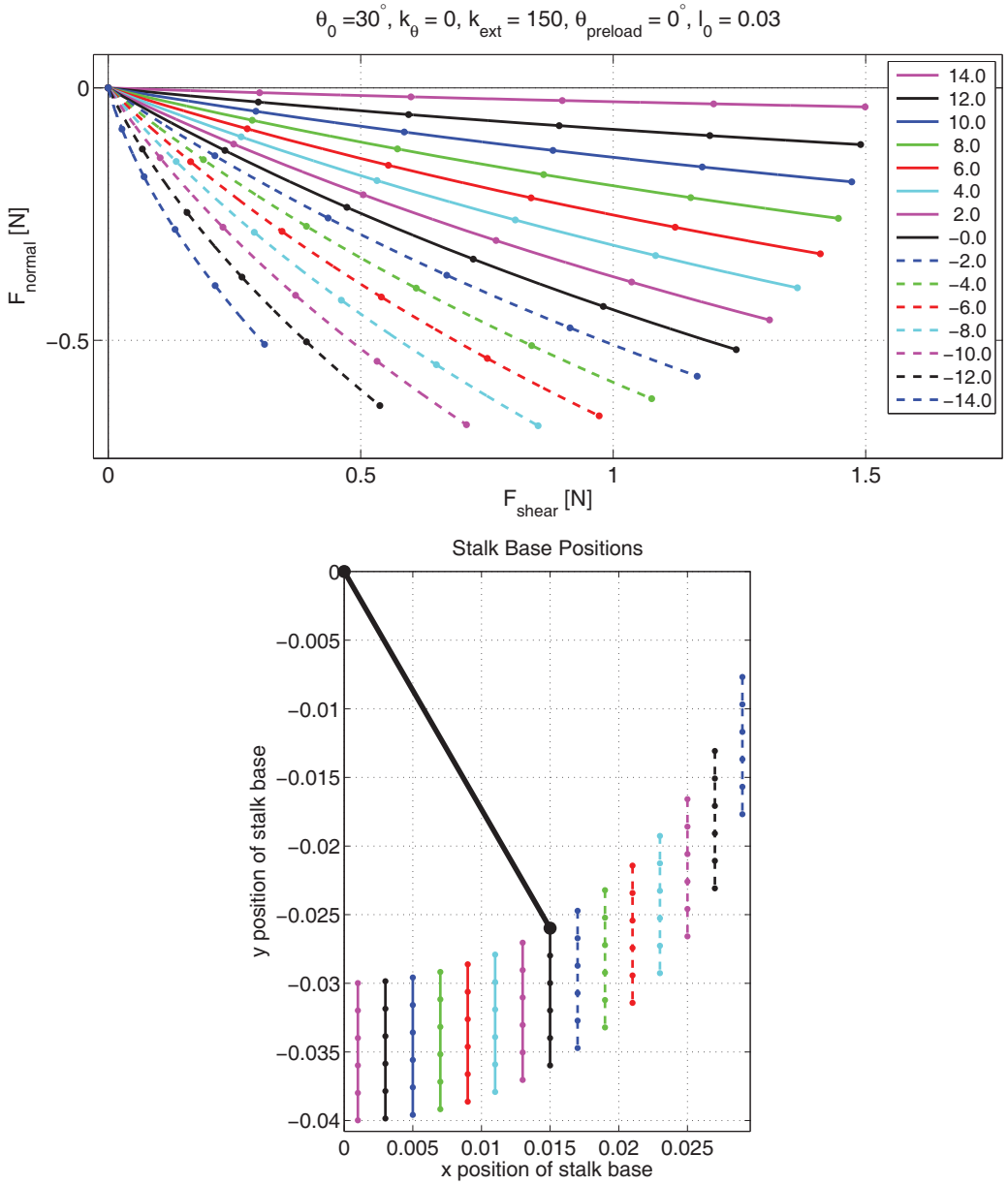

Figure 4.30: In this simulation, preloads from 14mm to -14mm were applied, in 2mm increments. Negative preloads, with dashed lines, show the effects of adhesive loads. The spine base was displaced 1cm down the wall. The original position of the stalk is shown with a black line.

In the limit as k_θ goes to zero, the spine linkage acts as an extensible beam supported on either end by a pin joint. In this case, since the pin joints cannot support moments, the forces will always go along the length of the beam. If the beam is then at an angle θ with respect to the surface, the forces on the spine will be at an angle θ as well. If the base of the suspension is moved toward the surface with a preload, this will cause the beam angle to change and thus the resulting loading angle as well.

4.8.1 Effects of varying θ_0 and k_θ

Figure 4.31(left) shows the effects of varying θ_0. From top to bottom, the rows have $\theta_0 = \{15°, 30°, 45°\}$. As the initial stalk angle θ_0 is increased, the slope of the loading lines becomes steeper.

In figure 4.31(left), the bottom plot has an initial angle of 45°. In this plot, for the largest preload of 6mm, the spine tip must be loaded with an angle of $> 30°$. Thus, this linkage will not be able to attach to any asperities with maximum loading angles less than this, making it practially worthless, as discussed in section 3.5.3. In general, when $k_\theta \approx 0$, the angle the stalk makes with the surface when the stalk is maximally preloaded (in this case 6mm) must be less than the maximum angle some surface asperities must support.

One solution to the problems caused by a large θ_0 angle is to increase k_θ, which is shown in figure 4.31(right). In this figure, from top to bottom, $k_\theta = \{0, 0.01, 0.02\}$ [N m/radian]. As k_{theta} increases, the lines shift upwards. For fixed other stalk parameters, a value of k_{theta} can be chosen to achieve forces in pure shear at the maximum deflection and preload. In figure 4.31(right), this can be seen to be true in the bottom plot, or in figure 4.31(left) in the top plot.

The cost to this favorable linkage behavior is that a very high preload force can be required, almost 0.4N with the largest preload deflection in figure 4.31(right). This is not a problem in applications where a positive normal force is applied, e.g. the rear feet of a climber. This linkage behavior can be used to produce high effective friction.

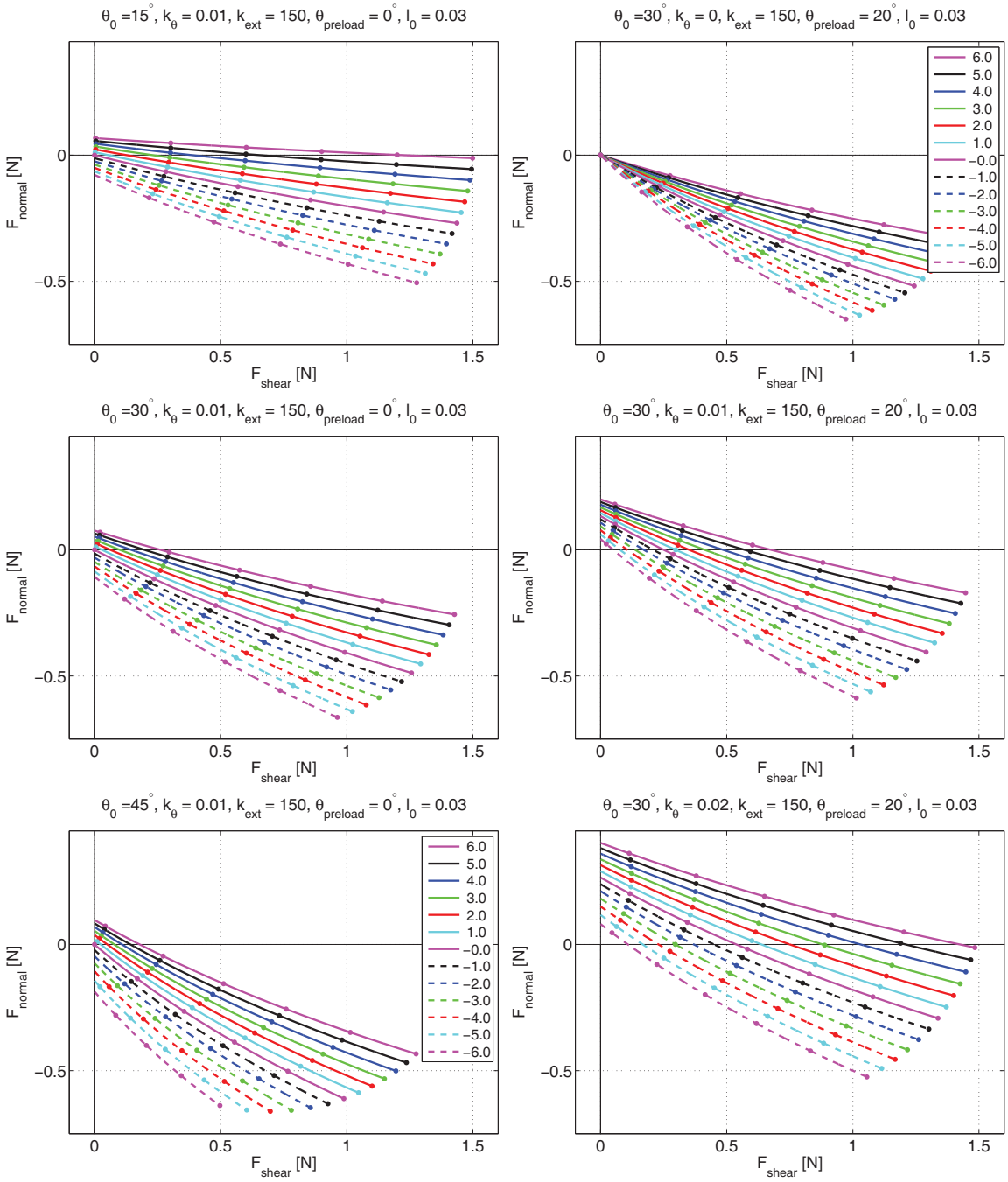

Figure 4.31: Results of simulations using the stalk model and varying parameters. Left, θ_0 is varied. From top to bottom, $\theta_0 = \{15°, 30°, 45°\}$. Right, k_θ is varied. From top to bottom, $k_\theta = \{0, 0.01, 0.02\}$ [N m/radian]. In both columns, the stalk model was set to have an initial length l_0 of 3cm. Preloads from 6mm to -6mm were applied, (negative preloads, with dashed lines, showing the effects of adhesive loads), and the spine base was displaced 1cm down the surface.

However, in applications where adhesion is required, high required preloads are counter-productive because any preload force applied into the surface must be sustained as additional adhesion by the other parts of the system attached to the surface. In this case, it is desirable to make the normal compliance as soft as possible. There does need to be a minimum value for the normal compliance of a spine suspension, however, because there is friction between the spines. With a very compliant structure, slight pressure between the toes leads to them sticking together and moving in groups, which hinders them from finding their own asperities.

These design explorations suggest that ideally, we should make the overload protection pin permit the toe to move through as large an angular range as possible. To make the linkage permit motions purely in shear, the θ_0 angle should be small, and then with the k_θ assumed to be non-zero, it will be possible to generate pure shear forces. However, the linkage should still be able to support large adhesive loads, if the spines are used on surfaces that could support them. If the overload protection pin can only permit a small range of angles, an ankle joint can be used in conjunction with the toe suspension.

Further plots showing the effects of varying the stalk model parameters k_{ext}, k_θ, θ_0, and $\theta_{preload}$ are shown in the Appendix, section A.4.

4.8.2 Effects of varying l_0 and θ_0

Figure 4.32 shows the effects of varying the initial stalk length l_0 and initial angle θ_0. In the left column, the initial angle θ_0 was changed to keep the x-component of the initial base position of the stalk a constant distance from the surface even as the stalk length was increased (i.e., x_0 remained constant). In the right column, the initial stalk angle (θ_0) was kept constant, so as the stalk length increased, the base of the stalk got further from the surface.

Keeping the base of the stalk a constant distance from the surface might be desirable to keep the height of the toe linkages (measured from the surface) small, for robotic or human climbing applications. Or, this constant distance could model the height required for the linkage itself. For example, in the RiSE and ZMan toes, in

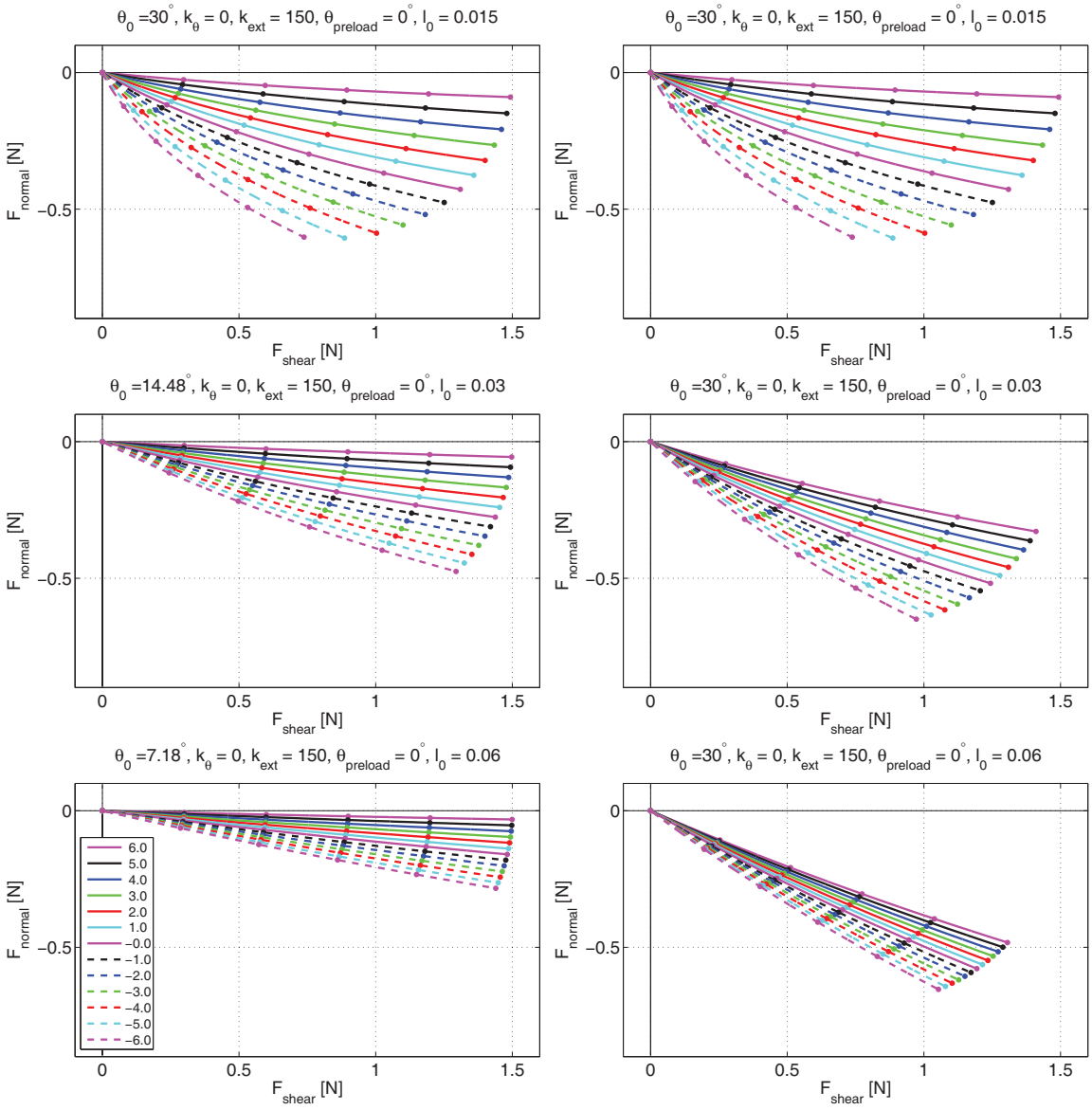

Figure 4.32: Results of simulations using the stalk model and varying l_0 and θ_0. In both columns, the stalk length increases from top to bottom, with $l_0 = \{1.5, 3, 6\}$ [cm]. In the left column, the initial angle θ_0 was changed to keep the base of the stalk a constant distance from the surface even as the stalk length was increased. From top to bottom, $\theta_0 = \{30°, 14.48°, 7.18°\}$. In the right column, the initial stalk angle was kept constant at $\theta_0 = 30°$, so as the stalk length increased, the base of the stalk got further from the surface. In each simulation, preloads from 6mm to -6mm were applied, (negative preloads, with dashed lines, showing the effects of adhesive loads), and the spine base was displaced 1cm down the surface.

figure 4.2, the plastic part supporting the back of the toes (element 2) has a minimum thickness under the pin to prevent it from breaking.

In both columns, as the stalk length increases, the range of angles that forces can be applied at decreases, for the fixed range of preloads. In the left column, the forces become more concentrated towards the F_{shear} axis, which is useful if it is desired to generate loads nearly in shear. In the right column, the forces stay approximately around the same angular range.

These effects can be understood as follows: as l_0 increases, the angular change that the stalk undergoes decreases, for a given drag distance. In the limit as the stalk becomes infinitely long, the stalk angle will not change at all if the base is moved, and thus the forces will remain at a fixed angle. So, if the stalk length is increased, it may be desirable to permit the stalk to move through a larger angular range.

Also, we can observe in this figure that as the stalk length increases, the loading lines become straighter. This leads to better load-sharing, as discussed in section 4.4.

4.9 Summary

In summary, the RiSE toes are close in behavior to the ideal suspension for load-sharing. The linkage characteristic loading lines in force-space are curved up slightly, but the spines require extremely low preloads and have an approximately radial pattern. The linkage causes a reduction in the limit curve of less than 2.5° due to the non-ideality, as compared to an ideal suspension.

It is better to have linkage characteristic loading lines that curve up (towards the F_{shear} axis) than curve down, because when excessive normal loads are applied, the least-loaded spines will disengage (rather than the most-loaded). Also, the true limit curves also bend towards the F_{shear} axis due to asperity failures, and loading lines that curve up will match this more closely. Finally, loading lines that curve up may be useful for facilitating the spines' catching on asperities with higher θ_{max} angles.

The RiSE spines also re-engage on surfaces effectively under most situations. One cost of the linkage non-ideality is that spines will not be able to re-engage when loads

are applied at large angles. However, for shallower loading angles, the spines exhibit dynamic adhesion, maintaining adhesion while sliding large distances over the surface. This behavior occurs when the loading magnitudes are too large, causing the spines to hit their overload protection pins and disengage, at which point they can re-engage.

One shortcoming of the RiSE spine suspension is that the range of possible loading angles over which the toes experience good load-sharing is somewhat small, only around $10 - 15°$, depending on the initial angle of the suspension with respect to the surface. This range is improved by the addition of an ankle between the robot and the spines.

Design explorations also suggest a number of areas for improvement to the spines. Making them longer will improve load-sharing performance, though at the cost of decreased packing density if multiple rows of spines are used. There is a practical limit to how short the RiSE spine suspensions can be, because as the length shrinks, the initial angle will become too steep for them to attach to many asperities. Allowing the spines to move through a wider range of motion by modifying the overload protection mechanism would also be beneficial. The extensional load-sharing performance of the spines can also be improved by making the extensional force (between the spine base and the spine tip) increase quickly and then become more constant for large deflections.

Chapter 5

Patch stiffnesses and moments

5.1 Introduction

When multiple rows of spines are distributed over a finite area (e.g., the area of a robot foot), it becomes necessary to consider the pressure distribution over the entire patch. Similarly, for directional dry adhesives, patch loading, which depends on patch stiffness and orientation, becomes an important consideration. Control of a robot's limb is drastically simplified if the foot will engage reliably when placed on the surface even if it is not parallel to the surface. However, creating a structure that facilitates alignment and even pressure distribution can be challenging, as we shall see in this chapter.

We focus our attention on patches of dry adhesives for this chapter because they are smaller, easier to measure, and perhaps more sensitive to minor misalignment, than arrays of spines. In particular, we will use the hierarchical directional dry adhesive developed in [2, 81] because it can be used in large patch sizes (larger than 100 cm^2). These adhesives, shown in figure 5.1, are constructed of a sheet of microwedges (small wedge-shaped rubber stalks) supported by a suspension layer (for details on the microwedge layer, see [80]; for details on the whole structure see [2, 81]). These adhesives are useful in analysis because they are directional, like the spines. They have a limit curve which is also characterized by a maximum loading angle θ_{max} and

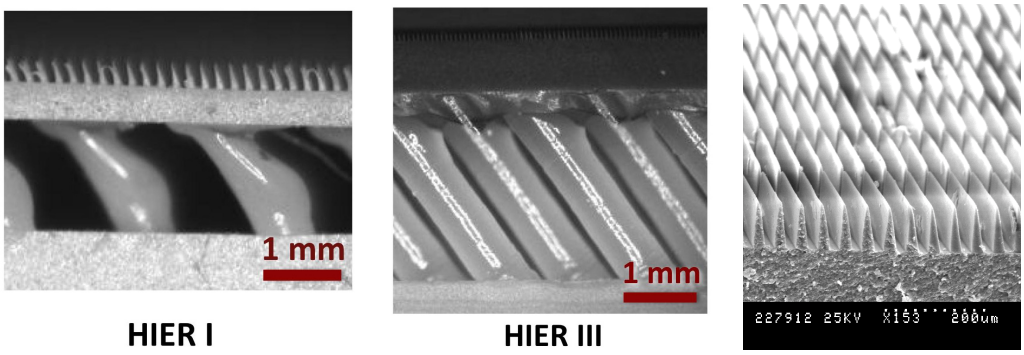

Figure 5.1: Left and center, examples of a patch of microwedges supported by a suspension structure. The center version has much smaller microwedges. Right, a close-up of the microwedges. Pictures from [81].

Figure 5.2: Left, example of a patch of dry adhesive supported by a hierarchy. The patch is viewed through the glass surface it is attached to, with gray areas attached and black areas not attached. Even with the hierarchy, the patch is only partially in contact with the surface. Right, a large patch with multiple rows of spines.

a maximum force F^* which follows a similar pattern to the spines.

We observe that with these patches of dry adhesives, the entire patch does not engage the surface, perhaps 50-80%. Figure 5.2 shows an example of a well-aligned patch of dry adhesive which is only partially in contact with the glass surface. The patch must be aligned to within fractions of a degree in both the ϕ and ψ directions

to engage even this well. Large patches of spines were also observed not to attach to a wall uniformly. With the ZMan climbing paddles, shown in figure 5.2(right), rows of spines were mounted to a rigid backing. During their use, it was observed that many fewer of the spines in the lower rows engaged as compared to the top row. In this chapter we will examine the properties of the suspension structures for multiple rows of spines, or patches of dry adhesives, and consider the tradeoffs between them, in an attempt to generate as much adhesion as possible between a large patch and a surface.

Patches of dry adhesives or spines have similar requirements to individual dry adhesive stalks (e.g. microwedge stalks) or rows of spines, but with the further requirement that moments at the face of the patch must be minimized. Because we have a large patch area and a compliant suspension structure, any moment at the patch-surface interface will lead to the patch tilting with respect to the surface, which may lead to the patch coming un-stuck. This is arguably the primary difficulty in creating a suspension for a large area, so we will examine the stiffness matrices for different patches and how they should behave in this regard. In practice, the suspension for large patches includes the compliance of the robot's leg or climber's hand.

5.2 Problem setup

We define a simplified form of the problem to use in analysis. A diagram of the problem setup is shown in figure 5.3. A patch of adhesive with width w_z and length w_y is connected to a rigid backing. The patch's rigid backing is connected to a ball joint at a distance (x_j, y_j) from the center of the front of the patch, and is in the center of the patch in the z-direction. The amount the front of the patch compresses or extends under a load is assumed to be small in comparison to y_j. The rotation of the ball joint (which equals the rotation of the patch) is ϕ in the x-y plane and ψ in the x-z plane. The surface it is attaching to is assumed to be flat, and in the y-z plane.

The ball joint has a torsional spring about it, so it can generate moments

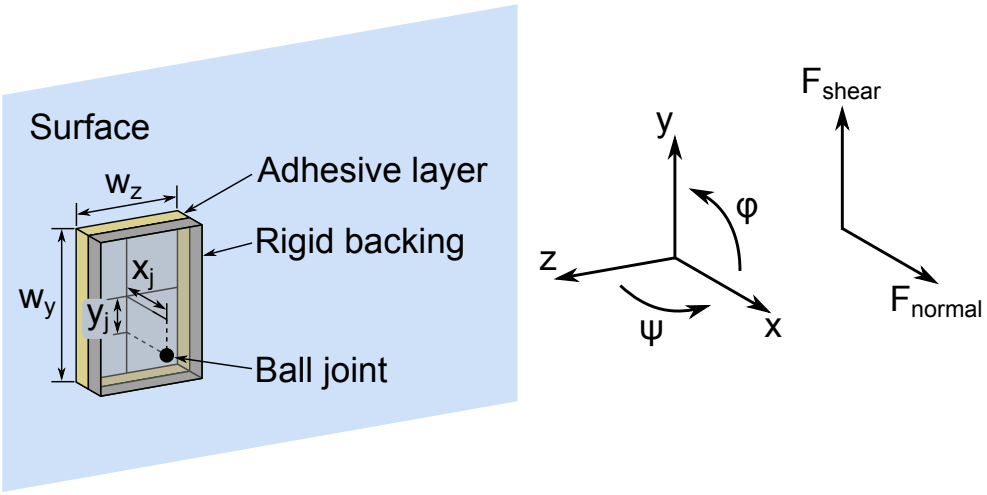

Figure 5.3: Coordinate system and problem setup for patch moments analysis. A patch of adhesive is attached to a rigid backing. The backing is supported by a ball joint a distance $(x_j, y_j, z = 0)$ from the center of the patch.

$$M_\phi = k_\phi \, \Delta\phi, \tag{5.1}$$

$$M_\psi = k_\psi \, \Delta\psi, \tag{5.2}$$

under rotations $\Delta\phi, \Delta\phi$.

When the patch is brought into contact with the substrate, it is at an initial angle of (ϕ_0, ψ_0) (we assume it is rotated properly in the third direction).

5.2.1 Applicability of setup to practical situations

Frequently, patches of dry adhesives are tested on a stage which is very stiff. The stage holds its orientation, and thus the patch's orientation, relative to the substrate. It can apply very large moments (in comparison to the moments caused by forces on the patch) in order to maintain this orientation. In our problem setup, this corresponds to $k_\phi, k_\psi \to \infty$. Furthermore, the patch is carefully aligned with the substrate before testing begins $(\phi_0, \psi_0 = 0)$. With this careful alignment and stiff stage, the forces the

patch can sustain will be as high as is practially achievable.

In applications other than testing on a stage, it is not always possible to hold the patch parallel to the substrate. A robot can be built to be relatively rigid, and can be very long relative to the patch diameter; in this case, it is possible to maintain the patch's initial orientation with respect to the wall—the feet will not rotate under applied loads (corresponding to $k_\phi, k_\psi \to \infty$). However, if the robot does not have sufficient degrees of freedom, the patch may not be parallel to the substrate ($\phi_0, \psi_0 \neq 0$). In this case, little of the patch may be in contact with the substrate if ϕ_0 or ψ_0 are large.

The other possibility is to have a soft structure supporting the patch, such as the human hand supporting the patch of spines in figure 5.2(right), corresponding to k_ϕ, k_ψ finite. In this case, we expect the patch to rotate under the applied loads. This may be useful to bring the patch into alignment with the surface, if it can rotate under preloads applied into the wall ($F_{normal} > 0$). However, the patch will also be able to rotate when adhesive loads are applied. This may cause it to disengage easily. For the case of a soft structure supporting the patch, we can assume either the patch is well-aligned to begin with ($\phi_0, \psi_0 = 0$) or not well aligned ($\phi_0, \psi_0 \neq 0$).

We are interested in determining the constraints on k_ϕ and k_ψ in order to maximize the ability of the patch to maintain adhesion to the surface even under a variety of F_{shear} and F_{normal} loads, and also maximize the ability of the patch to self-align if $\phi_0, \psi_0 \neq 0$. Also, to make patches of adhesive useable with soft supporting structures, we are interested in determining how k_ϕ and k_ψ can be made as small as possible.

5.2.2 Forces on the face of the patch

To analyze when a patch of adhesive will remain attached to the substrate or come off requires examining the forces on the individual adhesive elements. These are the individual microwedges, in the case of synthetic dry adhesives we consider, or the individual spines in a large patch. Each adhesive element can support normal and shear force up to some limits. If we again assume the elements can support force magnitudes of F^* at angles between pure shear and θ_{max} (see section 2.4),

then the maximum shear force per element is F^* and the maximum normal force is $F_{n,max} = F^* \sin(\theta_{max})$.

A diagram of the forces on the individual adhesive elements in a patch is shown in figure 5.4. The figure shows a top view of the patch in figure 5.3. N individual elements are distributed uniformly across the patch. In the limit as $N \to \infty$, it is useful to analyze the forces as a continuum and consider forces per unit length across the patch rather than the forces on individual elements. Force per unit length will be denoted by γ. The maximum normal force per unit length across the width of the patch is $\gamma_{n,z,max}$, and the maximum normal force per unit length across the length of the patch is $\gamma_{n,y,max}$.

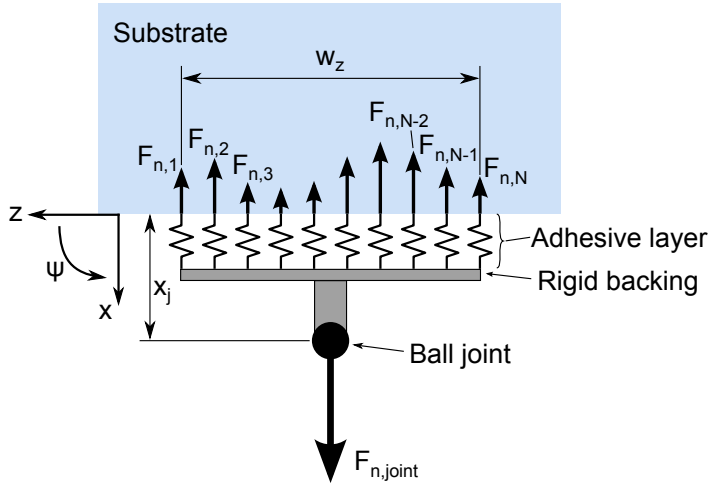

Figure 5.4: Top view of a patch, showing forces on individual adhesive elements across the width of a patch. The patch is loaded from the ball joint with a force $F_{n,joint}$ in the normal direction.

5.3 Calculations on patch behavior

In this section we compute the forces and moments on a patch when it is in static equilibrium, and use this to determine trends that govern how a suspension should be constructed. We begin by examining the patch in the y-z plane as shown in figure 5.4, because it is the simpler case.

5.3.1 x-z plane

Although it is tempting to assume the forces on the face of the patch are uniformly distributed, this is generally not the case. As illustrated in figure 5.5, the forces vary across the patch (here shown in a top view). This non-uniform distribution can be represented by a single force vector, $F_{n,patch}$, which is offset from the center of the patch by a distance d_z in the z-direction. There is a moment on the patch due to the offset of this force from the center:

$$M_{patch} = d_z F_{n,patch}. \tag{5.3}$$

To achieve static equilibrium, the patch must rotate a small amount ψ_{patch}. As the patch rotates, two effects will occur. First, the forces on the adhesive elements across the patch will redistribute to decrease d_z. Second, the spring around the ball joint will cause a moment on the patch. This moment from the ball joint spring will counter any remaining moment on the patch due to d_z not being zero. These two effects are illustrated in the lower diagram in figure 5.5, where the force distribution on the patch has changed as the patch rotates and there is a moment from the ball joint.

We first consider how the forces on the adhesive elements vary with the rotation of the patch. Suppose the adhesive layer on the patch has a spring constant κ per unit length across the width of the patch, due to the compliance of the adhesive elements. In general κ will not be constant (the springs will not be linear), but assuming κ is constant will provide insight into the problem. If κ is constant, a rotation corresponding to a height change of h from one side of the patch to the other corresponds to a moment of

$$M_{adhesive} = \frac{w_z^2 \kappa h}{12}. \tag{5.4}$$

We also assume $h << w_z$, which leads to $\Delta\psi$ small so $\tan(\Delta\psi) \approx \Delta\psi$. Then, the height change of h corresponds to an angular change of the patch of

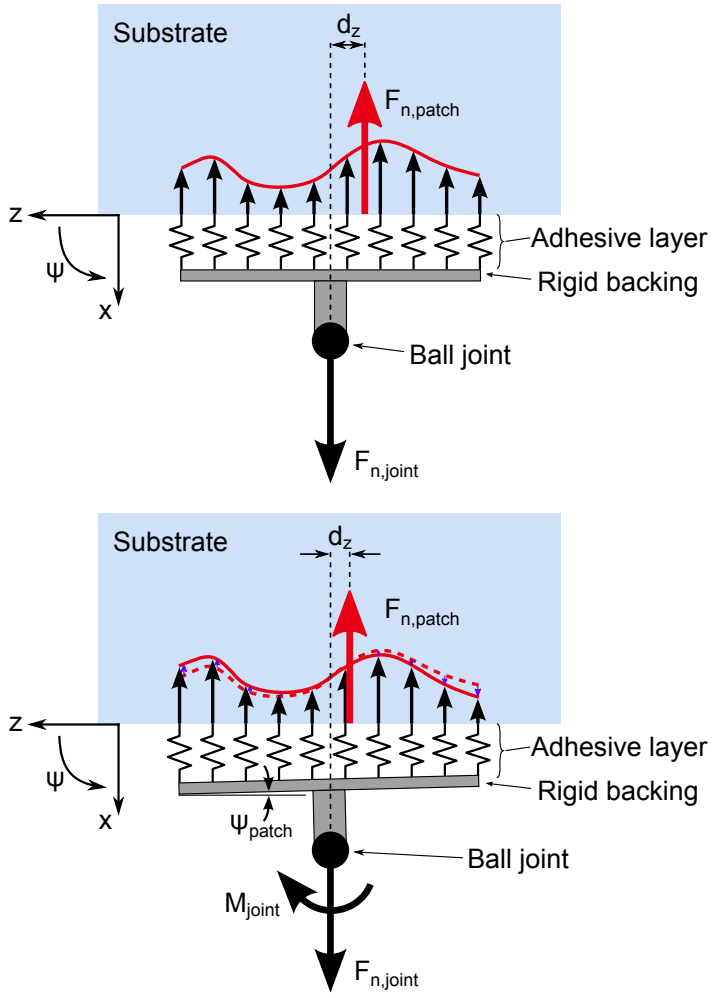

Figure 5.5: Top view of a patch, showing forces on individual adhesive elements across the width of a patch. The patch is not loaded uniformly, resulting in a net force $F_{n,patch}$ which is offset from the center of the patch a distance d_z. This offset creates a moment which must be resisted by either a moment caused by differences in adhesion across the face of the patch, or by the torsional stiffness of the ball joint after the patch rotates a small amount. The upper diagram shows the initial forces, and the lower diagram shows the system after the patch has rotated and reached static equilibrium. In the lower diagram, the dashed red line shows the initial force distribution, and the small purple arrows show the change in forces to reach the final distribution (solid red line).

$$\Delta\psi = \arctan(h/w_z) \cong h/w_z, \tag{5.5}$$

and thus:

$$M_{adhesive} \cong \frac{w_z^3\,\kappa\,\Delta\psi}{12}. \tag{5.6}$$

This is the moment on the patch due to the adhesive being loaded more in tension on one side and more in compression on the other side as the patch rotates about the ball joint.

The other moment on the patch is from the torsional spring around the ball joint. As the patch rotates, the spring applies a moment which is directly related to its angular change per equation 5.2, $M_{joint} = k_\psi\,\Delta\psi$. The patch will reach an equilibrium when the sum of these two moments equals the moment on the patch due to the force imbalance (eq. 5.3).

Of note, the patch moment will also be affected by the rotation due to the fact that the ball joint is a distance x_j from the patch face. As the patch rotates, d_z will decrease. The new distance d_z' is related to the original distance d_z by

$$d_z' = d_z - \Delta\psi\,x_j. \tag{5.7}$$

The decrease in d_z will decrease the M_{patch} moment in equation 5.3.

Examples

In general, there will be a tradeoff between these three contributions ($M_{adhesive}$, M_{joint}, d_z') to the moments on the system. A few sample cases are useful to discuss to gain intuition for the system.

In the case of a very stiff spring around the ball joint, M_{joint} will be large and the patch will rotate very little. This will correspond to d_z remaining large after the rotation, and the forces largely remaining unchanged.

In the case of a very small spring around the ball joint, M_{joint} will be small, and

the patch will rotate significantly. The forces on the patch will be required to change drastically. If the initial offset d_z is too large, stalks on one end of the patch may have forces on them in excess of $F_{n,max}$, causing them to disengage. Once one stalk disengages, frequently this leads to a rapid disengagement of the entire patch. With one fewer stalk, the remaining stalks must support the adhesive force formerly held by that stalk. This will cause two effects. First, the remaining stalks are more likely to fail because each must support an increased load. Second, the force distribution will shift slightly so as to increase d_z. This causes the M_{patch} moment to increase, followed by further rotation of the patch. The cycle will repeat itself, leading to complete disengagement, unless the force distribution over the width of the patch is altered somehow or the ball joint stiffness causes the M_{joint} moment to increase faster than M_{patch}.

Solving for static equilibrium conditions

Given the initial situation of a flat patch with a force imbalance as shown in the upper part of figure 5.5, we must solve the following equation for $\Delta\psi$ to determine the rotation of the patch at static equilibrium:

$$M_{patch} = M_{joint} + M_{adhesive} \tag{5.8}$$

$$\Rightarrow (d_z - \Delta\psi\, x_j) F_{n,patch} = k_\psi\, \Delta\psi + \frac{w_z^3\, \kappa\, \Delta\psi}{12} \tag{5.9}$$

Furthermore, the force per unit length γ must remain less than the maximum allowed γ_{max} or stalks will disengage. The most-loaded end of the patch will have

$$\gamma = \kappa(h/2) + F_{n,patch}/w_z \tag{5.10}$$

with the first and second terms corresponding to forces from the moment on the patch and the net force, respectively. Simplifying to remove h by substituting $h = \Delta\psi\, w_z$ we get

$$\frac{\kappa\,\Delta\psi\,w_z}{2} + \frac{F_{n,patch}}{w_z} < \gamma_{max}. \tag{5.11}$$

Combining equations 5.9 and 5.11, we get that the maximum force $F_{n,max}$ on the patch must satisfy:

$$\frac{6\,\kappa\,w_z\,d_z\,F_{n,max}}{12F_{n,max}x_j + 12k_\psi + w_z^3\,\kappa} + \frac{F_{n,max}}{w_z} \leq \gamma_{max}. \tag{5.12}$$

The first term of this equation is the additional force on the edge of the patch caused by the moment due to the forces on the face and ball joint being misaligned. The second term is the force uniformly distributed across the patch due to the applied adhesive force. If the forces on the patch and ball joint were perfectly aligned, i.e. $d_z = 0$, then the first term would be zero and the patch could sustain the maximum possible force of $F_{n,max} = \gamma_{max}\,w_z$. To determine the effect of the different variables in our model, we examine the first term of this equation, which we wish to minimize.

If k_ψ is increased, corresponding to stiffening the ball joint spring, the first term will decrease. This is perhaps obvious from the examples earlier. One of our original goals was to determine the minimum possible value of k_ψ, so this result is not entirely useful. Rather, how k_ψ affects the result in comparison to the other terms is useful.

If w_z, the patch width, is increased, then the first term will also decrease. Even if the offset d_z increases in proportion to w_z, the term will still decrease due to the w_z^3 in the denominator.

If x_j is increased, moving the ball joint away from the surface, the first term will decrease. The effect of x_j is interesting because in this analysis we assume we are applying an adhesive force exactly perpendicular to the wall. In practice, this may not be true. A large x_j will tend to amplify the effect of errors in the direction of force, so this result should be treated with some caution.

Finally, decreasing κ will minimize the first term in the equation. While κ appears in both the top and the bottom of this term, on the bottom there are two other terms as well. So, if κ is decreased, the numerator and the term with κ in it in the denominator will both decrease. However, the two other terms in the denominator

will remain constant, and so the entire first term in equation 5.12 will decrease as a result. Intuitively, this corresponds to the following: if κ is made smaller, the adhesive patch can rotate to larger angles before developing a force on the most-loaded stalks that will lead to disengagement. However, the torsional spring around the ball joint will develop moments rapidly with increased patch rotation, as will the effect of the ball joint being mounted a distance x_j from the patch face. In the end, these two components will end up contributing more towards the required moment on the patch than they did previously, leaving the adhesive patch with a more even force distribution.

It is also useful discussing the case where the patch is initially misaligned with the surface before it comes into contact ($\psi_0 \neq 0$). Misalignment will cause two problems. First, it will tend to increase the values of d_z, since one side of the patch will contact the wall before the other. The side which contacts first will have larger preloads during engagement, and thus the adhesive elements may contact the wall more securely. Second, and perhaps more importantly, the misalignment will cause the patch to have an additional moment because some force will be required to keep the patch aligned. This will tend to reduce the force that the patch can sustain. Smaller values of κ and k_ψ will cause the misalignment to have a smaller moment. In adhesion, though, stiffer values of k_ψ perform better. So reducing κ may be the best way to permit initial angular misalignments.

In general, the situation is more complicated than this analysis has discussed. When the patch rotates, d_z may actually increase in response to the changing forces on the patch, due to behavior of the adhesive elements. This will require the ball joint stiffness k_ψ to be higher than would be indicated by these calculations. Furthermore, the stiffnesses of the adhesive elements will likely be nonlinear, so it may further behave differently. However, the same trends and method of analysis described here will apply.

5.3.2 x-y plane

The problem of suspension design in the x-y plane to accomodate rotations in the ϕ direction shares many similarities with that in the x-z plane to accomodate rotations in the ψ direction. In both cases, moments from the suspension ball joint and adhesive patch are required to counter misalignment of the forces on the patch and on the ball joint. The primary difference stems from the fact that both the F_{normal} and F_{shear} loads are in the x-y plane, whereas only the F_{normal} force is in the x-z plane. With both F_{normal} and F_{shear}, the magnitude and direction of the applied force will now vary, instead of just the magnitude. With the assumed limit curve of the adhesive elements, forces can vary in magnitude up to F^*, and can vary in angle from being in pure shear to an angle of θ_{max} away from the surface. Figure 5.6 shows the setup for the x-y plane, with a patch connected to a rigid ball joint. The forces on the face of the patch are not uniform, leading to a misalignment between the force on the face of the patch, F_{patch}, and the force on the ball joint F_{joint}.

The x-z plane discussed previously is an unstable system: misalignments between the force on the ball joint and the force on the patch will always lead to rotations which, if unchecked, will lead to the patch disengaging. We must apply stiffness at the ball joint or have a large value of x_j to keep the patch on the wall.

We can perform a similar analysis on the x-y plane, to determine the required stiffness at the ball joint in order to keep the patch on the wall. If we were to perform such an analysis, we could again assume the patch was initially aligned parallel to the wall, and compute the stiffnesses required to mitigate rotations leading to disengagement.

However, in the x-y plane we do have control over another degree of freedom—the initial pitch of the patch—which can be exploited to improve the behavior of the system. Whereas with the x-z plane the patch will always be able to rotate in either direction at perfect alignment with the maximum possible adhesion, with the x-y plane we can alter the initial rotation of the patch and the location of the ball joint to alter the behavior.

We briefly consider the moments on the patch to determine its rotational behavior.

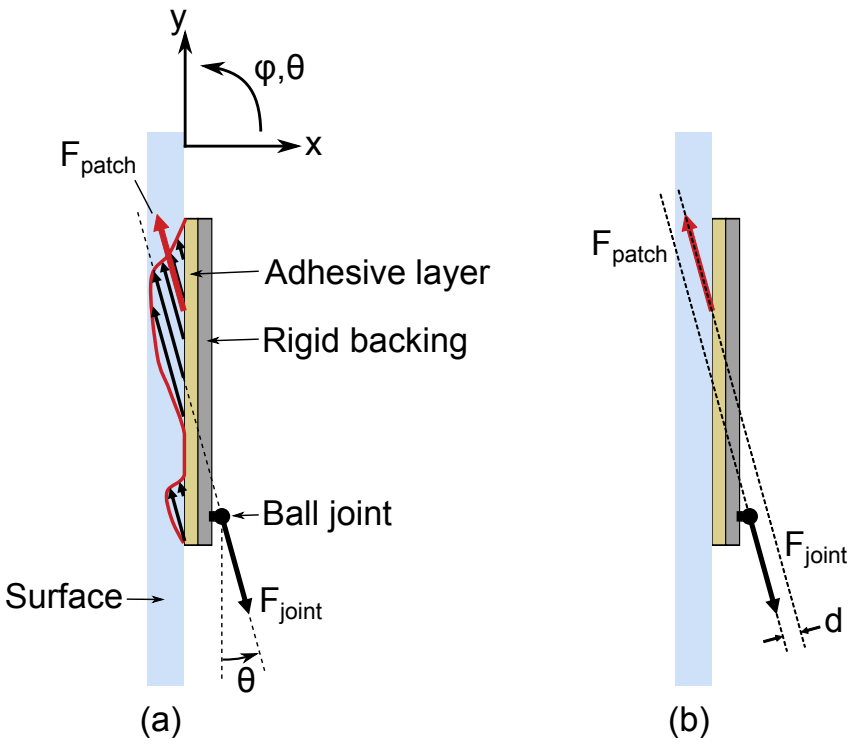

Figure 5.6: Diagram of setup for patch moments analysis in the x-y plane. (a), forces on the patch are not uniform. Loads can be at an angle $\theta < \theta_{max}$. The patch is at an angle ϕ with respect to vertical (here drawn as $\phi = 0$) and the loads are at an angle θ. (b), the nonuniform load often leads to an offset of d between the force on the face of the patch, F_{patch}, and the force on the ball joint F_{joint}.

We know that the loads on the patch will fall between $\theta = 0$, in pure shear, and $\theta = \theta_{max}$, the maximum angle at which we can pull away from the surface without the adhesive elements failing. There are two cases to consider. First, if the ball joint is located below a line drawn at an angle θ_{max} from the location of F_{patch} on the patch face, then the patch may rotate either direction, depending on the direction of force. This is because the F_{shear} component of the force will cause clockwise rotations (for $x_j > 0$), but the F_{normal} component will cause counter-clockwise rotations. The patch can rotate in either direction depending on which component dominates. However, if the ball joint is above a line drawn at an angle θ_{max} from the location of F_{patch} on the patch face, then the patch will always rotate clockwise, because the F_{shear} component will always be larger than the F_{normal} component. This second case is illustrated in

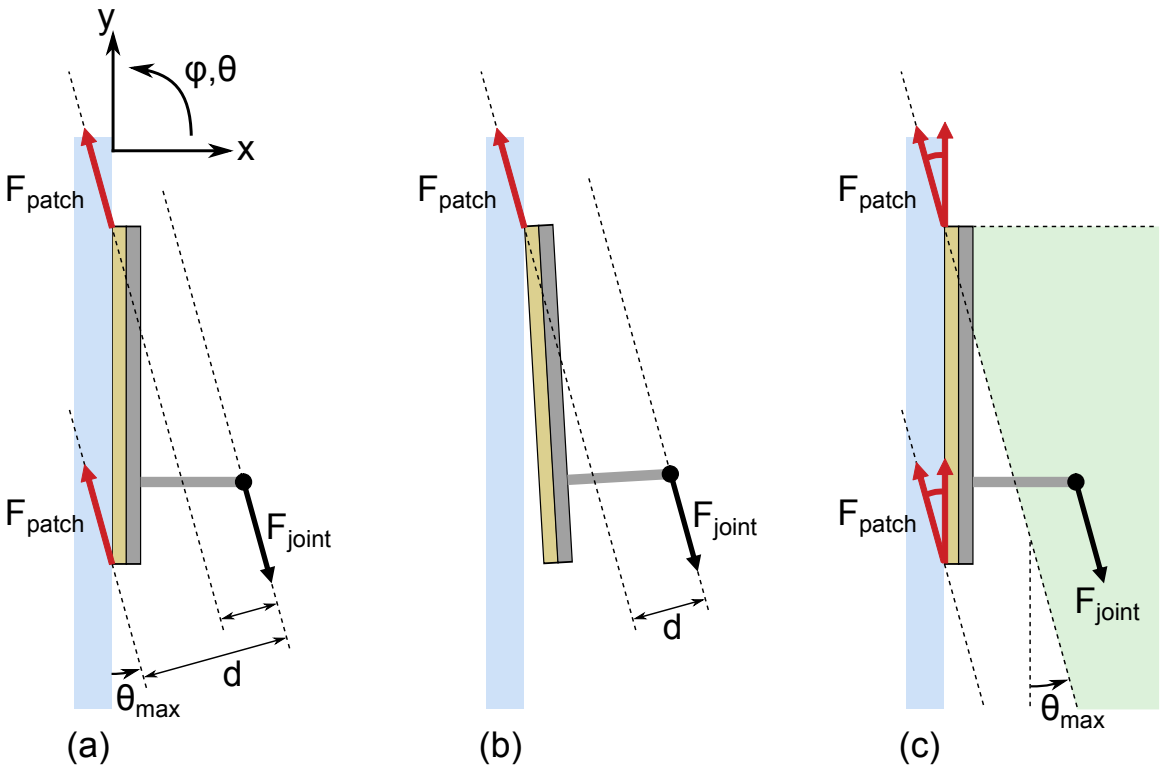

Figure 5.7: (a), the patch will always rotate clockwise independent of the loading direction and magnitude if it is above a line at an angle θ_{max} measured from the location of F_{patch} on the patch face. F_{patch} must lie somewhere on the patch face, so a conservative location is at the very top of the patch face. (b), angling the patch so the top contacts the wall first is the first component of stable engagement. (c), the green "stable" region indicates locations where the ball joint can be located and achieve stable engagement. It must be located below F_{patch} in the y-direction, and above the line at θ_{max} originating at the location of F_{patch}. The closer the ball joint is to the lower boundary of the region, the smaller the moment will be.

figure 5.7(a).

We would like the patch engagement with the wall to be stable, if possible. That is, when forces are applied and the patch rotates in response to those forces (and to the misalignment between F_{patch} and F_{joint}), we would like more of the patch to come into contact with the surface or d_z to decrease. In both cases, the patch will have better adhesion after the rotation than before the rotation. One way of making the patch engagement stable is the following:

- Tilt the patch foward slightly so the top of the patch always engages first. This is illustrated in figure 5.7(b).
- Place the ball joint such that the patch always rotates clockwise in response to applied loads, independent of the direction of those loads. Thus, as the patch rotates, the patch will become better-aligned with the surface, causing the adhesion to become more secure.

A few details about this scheme must be discussed. First, the ball joint cannot be too high or the system will be unstable: the ball joint needs to be located in the y-direction below the location of F_{patch} on the patch face. With the ball joint located below F_{patch}, the ball joint will approach the wall as the patch is loaded. This is illustrated in figure 5.7(c).

Second, the ball joint must be located further away from the wall than the line at angle θ_{max} extending from the location of F_{patch}. As discussed previously, this will always cause the patch to rotate clockwise for loads between $\theta = 0$ and $\theta = \theta_{max}$. If the top of the patch engages first, then F_{patch} will start close to the top of the patch. Then, as the patch becomes more aligned with the surface, F_{patch} will move down the wall. The ball joint must remain above the θ_{max} line at all times, even as the location of the ball joint changes as the patch rotates (due to the offset x_j of the ball joint from the wall). This is also illustrated in figure 5.7(c).

Third, it is still desirable to minimize the ball joint spring constant k_ϕ. To minimize it, the ball joint should be set to be close to the θ_{max} line. Having the ball joint further from this line will increase the distance between F_{patch} and F_{joint}, which will increase the moment needing to be canceled by the adhesive and the ball joint spring.

Finally, the stiffness of the ball joint spring should be set so that when the patch is at its maximum rotation, it is perfectly aligned with the wall. This assumes that the patch will have maximum adhesion when it is perfectly aligned. If it also has acceptably large adhesion when rotated slightly past parallel to the substrate, then that angle can be used as the maximum rotation, to permit a larger angular change. The maximum rotation will occur when the forces on the ball joint are the maximum possible, F^*, and the direction is such that the moment is largest. This direction

is in pure shear, with $\theta = 0$. With the ball joint above the θ_{max} line, any F_{normal} component will cause a counter-clockwise moment, which will decrease the rotation of the patch.

On the whole, this scheme will lead to a more secure engagement of the patch than a scheme of keeping the patch initially parallel to the wall and then putting the ball joint in a location where the patch can rotate in either direction. Of note, this scheme is how the microwedges at the surface of the adhesive patches in figure 5.1 behave. Although these structures are flexible and not supported by a rigid backing with a ball joint, the overall behavior is the same. The faces of these adhesives are initially at a large angle with respect to the surface, and only the very tip touches. As loads are applied, more and more of the face comes into contact with the surface.

We can also determine trends in the variables of the system to optimize performance of the system. As with the x-z plane, a softer adhesive patch will permit larger angular misalignments for the same moment. With this scheme, a larger permitted angular misalignment will allow the patch to move through a larger angular change as it is loaded, from being initially pitched forward to being parallel to the wall at the maximum load. A larger angular change will permit the ball joint spring k_ϕ to be smaller for the same resulting moment.

It is unclear if making the patch length w_y larger will be beneficial or not without further analysis. At first glance a smaller patch seems to be preferable. A larger patch will require a smaller angular misalignment with the wall to be fully in contact. Making the patch length smaller, for a given height range h over which the adhesive can attach effectively, will permit larger angular misalignments. Furthermore, with the attachment scheme, the location of F_{patch} is more controlled than in the x-z case, so a larger patch length may not be helpful.

Similarly, a larger length for x_j may not be of use either. For a constant load angle, for example $theta_{max}$, a longer x_j will cause the forces to become aligned more easily, which is beneficial. But if the direction of load is altered (e.g., it changes to be in pure shear), then a larger x_j will cause a larger moment on the patch which will need to be resisted by the ball joint spring. Therefore, it appears that to make k_ϕ as

small as possible, x_j should be shortened as much as possible.

As in the x-z case, a stiffer k_ϕ will cause less rotation, but we are interested in optimizing the suspension to minimize k_ϕ. Further analysis will be required to determine how k_ϕ varies relative to the other terms.

It is also useful discussing briefly the case where the patch is initially misaligned with the wall. In this case, the patch should be pitched forward sufficiently so that the top will continue to always attach first. Misalignment will require that the patch move through a smaller percentage of its maximum possible angular rotation under the maximum load; the remaining angular rotation can be used to accomodate the misalignment. Making the adhesive patch stiffness softer will be useful in increasing the maximum possible angular rotation, as discussed in section 5.3.1.

In summary, a scheme to tilt the patch foward is useful because the engagement will be more secure and more tolerant of variation in the direction of loading. Further analysis is required to fully understand this system.

5.4 Summary

We have analyzed an adhesive patch backed by a rigid backing and connected to a supporting structure through a ball joint. Moments causing the patch to rotate and detach from the surface must be countered by forces from the adhesive, moments from the ball joint springs, or motion of the ball joint. This is a useful structure for analysis, because many adhesives are used in patches with rigid backings exactly in this manner.

There are a number of areas of future work. The analysis should be extended to deal with non-linear adhesive stiffnesses and the actual behavior of patches as they are misaligned with surfaces. The analysis should also be extended to deal with non-rigid backings. Detailed analysis of the compliance of structures such as the microwedges is needed to gain a deeper understanding of how such structures should be made to maximize their adhesive performance.

Chapter 6

Conclusion and future work

In conclusion, we have developed a system for using spines to attach to rough surfaces. We found that the details of the spine/surface interaction depend on the local geometry, rather than typical roughness measures. The spines/asperity contacts can sustain forces within a certain limit curve, in which adhesive loads can be applied up to some angle away from the surface. We established constraints on the spine suspensions for them to be used effectively. Finally, we constructed arrays of spines and tested their linkage properties and their performance on surfaces. Spines were used effectively on both robot and human climbers to scale a variety of surfaces.

Spines are a robust and effective solution for adhesion, used by many types of animals in nature. Our system enables robots to climb surfaces that are too smooth for animals of comparable weight, due to the greater number of spines on our system than on an animal's foot. Our spines are useful in dirty and wet environments, similar to how animals gain reliable adhesion in a variety of adverse conditions.

Future work includes making the spine suspensions more compact in width and length so as to have increased spine density. Decreasing the height may also make integration onto robots or human climbing paddles easier. Different suspension designs can be used, so long as they follow the stiffness requirements laid out in chapter 3. Furthermore, it was found that the weight of the human climbing system was significant; lighter designs, including lighter materials, would be beneficial.

Smaller spines for grabbing onto smaller asperities will be useful as well, but will require increased numbers of spines. Suspensions on a larger scale for small groups of spines will probably be required, so the small spines can conform to the gross geometry of the surface. Improved suspensions for multiple rows of spines is another area of improvement. As discussed in chapter 5, proper compliance of the supporting structure is vital to ensuring that a large patch of spines or dry adhesives stays attached to the wall. There are many opportunities for future exploration in this area, including investigating flexible suspensions and varying the lengths of spines and dry adhesive stalks across the patch.

Finally, the constraints on spines interacting with surfaces can be used to gain insight into dry adhesive systems. Dry adhesives function differently than spines in that they are able to attach to most locations on a surface instead of just asperities. But many synthetic dry adhesives will be manufactured in rows and thus will be subject to constraints analogous to those for spines to achieve optimal load-sharing. In the future, we look forward to large arrays of spines combined with patches of dry adhesives to form an effective climbing system able to attach to most surfaces.

Appendix A

Appendices

A.1 Spine Failure Modes

We have observed that the spine/asperity contacts have three primary failure modes.

1. The spine fails plastically at its base due to tensile stress from bending.
2. The spine deflects elastically such that it slips off the asperity.
3. The asperity fails, typically as a particle becomes unbonded from the surrounding matrix.

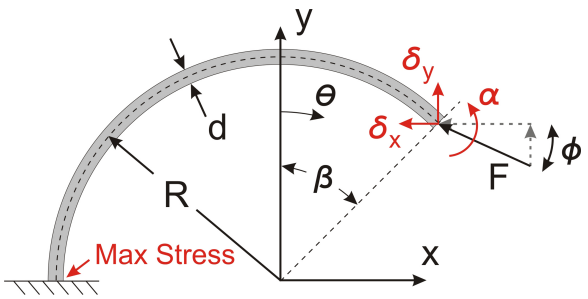

Figure A.1: Curved beam with variables used in spine failure mode analysis.

The first mode of failure is due to the tensile stress at the base of the spine. For a long curved spine, the maximum stress is essentially the same as it would be for a

straight cantilever beam [96]:

$$\sigma_{max} = \frac{Mc}{I} = \frac{32fld}{\pi d^4} \propto \frac{1}{d^2} \quad (if \quad \frac{l}{d} = const)$$

where

M = moment on base = fl

c = distance from neutral axis to edge = $d/2$

I = moment of inertia, which for a circular beam = $\pi c^4/4$

f = force exerted on tip of the spine

d = diameter of cross section of spine

l = equivalent beam length.

The second mode of failure is excessive tip rotation. Here we can apply Castigliano's Theorem to solve for the tip deflections and rotations for a curved spine [96]. Applying a dummy end moment, M, and solving for the end rotation, α, we obtain:

$$\begin{aligned} \alpha &= \partial U/\partial M \\ &= \frac{R^2}{2EI}[-2F_y + (2F_x + F_y(\pi + 2\beta))cos(\beta) \\ &\quad +(-2F_y + F_x\pi + 2F_x\beta)sin(\beta)] \qquad \propto \frac{1}{d^2} \\ &(if \quad \frac{R}{d} = const. \quad at \ \ given \ \ \beta, \ F_x \ \ and \ \ F_y) \end{aligned} \tag{A.1}$$

(see figure A.1).

The third mode of failure is that the asperity itself may break off. The literature on surface failure or erosion (e.g. [71, 94]) for cementitious materials such as concrete, or rock with hard crystals in a weaker matrix, generally starts with the Hertz stress

distribution at the contact [48]. The maximum pressure is at the center of the contact patch:

$$p_{max} = 3f/2\pi a^2 = (6fE^2/\pi^3 R^2)^{1/3}$$

where

$$a = (3fR/4E)^{1/3}$$
$$E = (1-\mu_s^2)/E_s + (1-\mu_a^2)/E_a$$
$$(1/R = 1/r_s + 1/r_a)$$

and the subscripts s and a refer to the spine tip and asperity, respectively.

The worst case tensile stress is at the periphery of the contact patch:

$$\sigma_T = ((1-2\mu_2)p_{max})/3$$

The actual failure will depend on the local stress state, number of cracks and fracture toughness of the material. However, it will be a function of the maximum tensile stress. Therefore we can write that

$$f_{max} = [(\pi\sigma_{max}/(1-2\mu_2))^3(1/2E^2)]R^2$$

The quantity in square brackets is a constant depending on the materials so that, in the end, the maximum sustainable load is expected to vary as the square of the radii of curvature of the spine tip and asperity.

A.2 Detailed calculations of beam bending using Mathematica

The following worksheet calculates the end rotation and deflection of a curved beam resulting from the application of a force, F, at the tip of the beam. The approach is to apply Castigliano's 2nd Theorum, decomposing the applied force along orthogonal

axes directions and applying a dummy moment at the tip of the beam to solve for tip deflections and rotations, respectively.

William Provancher
December 7, 2004

$$\mathbf{Forces:=\{Fx \to F * Sin[\phi], Fy \to F * Cos[\phi]\}}$$

$$\mathbf{geometry1:=\{\beta \to \pi/4, \phi \to \pi/36\}}$$

$$\mathbf{geometry2:=\{xF \to R * Cos[\beta], yF \to R * Sin[\beta]\}}$$

$$\mathbf{geometry3:=\left\{Emod \to 200 * 10^9, Izz \to \frac{\pi * d^4}{64}\right\}}$$

$$\mathbf{geometry4:=\{d \to 0.0002, R \to 0.005\}}$$

$$\mathbf{moment:=\{Mb \to Md + Fy * (xF - R * Cos[\theta]) + Fx * (yF - R * Sin[\theta])\}}$$

Formulating the energy stored in the beam.

$$\mathbf{U = \frac{1}{2 * Izz * Emod} \int_{-\frac{\pi}{2}}^{\beta} \left(Mb^2/.moment/.geometry2\right) R d\theta //Simplify}$$

$$\begin{aligned}
\Rightarrow \frac{1}{8\mathrm{Emod}\mathrm{Izz}} \big(R \big(&2\mathrm{Md}^2\pi - 8\mathrm{Fy}\mathrm{Md}R - 2\mathrm{Fx}\mathrm{Fy}R^2 + 2\mathrm{Fx}^2\pi R^2 \\
&+ 2\mathrm{Fy}^2\pi R^2 + 4\mathrm{Md}^2\beta + 4\mathrm{Fx}^2R^2\beta + 4\mathrm{Fy}^2R^2\beta \\
&+ 4R(2\mathrm{Fx}\mathrm{Md} + \mathrm{Fy}(\mathrm{Md}\pi - 2\mathrm{Fy}R + 2\mathrm{Md}\beta))\mathrm{Cos}[\beta] \\
&- R^2\left(-6\mathrm{Fx}\mathrm{Fy} + \mathrm{Fx}^2(\pi + 2\beta) - \mathrm{Fy}^2(\pi + 2\beta)\right)\mathrm{Cos}[2\beta] \\
&- 8\mathrm{Fy}\mathrm{Md}R\mathrm{Sin}[\beta] + 4\mathrm{Fx}\mathrm{Md}\pi R\mathrm{Sin}[\beta] - 8\mathrm{Fx}\mathrm{Fy}R^2\mathrm{Sin}[\beta] \\
&+ 8\mathrm{Fx}\mathrm{Md}R\beta\mathrm{Sin}[\beta] + 3\mathrm{Fx}^2R^2\mathrm{Sin}[2\beta] - 3\mathrm{Fy}^2R^2\mathrm{Sin}[2\beta] \\
&+ 2\mathrm{Fx}\mathrm{Fy}\pi R^2\mathrm{Sin}[2\beta] + 4\mathrm{Fx}\mathrm{Fy}R^2\beta\mathrm{Sin}[2\beta]\big)\big)
\end{aligned}$$

The beam tip rotation, α, is

$$\boldsymbol{\alpha = (\partial_{Md} U)\,/.Md \to 0//Simplify}$$

$$\Rightarrow \frac{1}{2\text{EmodIzz}} R^2(-2\text{Fy} + (2\text{Fx} + \text{Fy}(\pi + 2\beta))\text{Cos}[\beta] + (-2\text{Fy} + \text{Fx}\pi + 2\text{Fx}\beta)\text{Sin}[\beta])$$

In specifying beam geometry $\{\beta \to \pi/4,\ \phi \to \pi/36\}$

α/.Forces/.geometry1//N//Simplify

$$\Rightarrow \frac{0.165967FR^2}{\text{EmodIzz}}$$

Assuming the geometry and material properties to be

$\left\{\text{Emod} \to 200 * 10^9, \text{Izz} \to \frac{\pi * d^4}{64}, d \to 0.0002, R \to 0.005\right\}$

results in the following rotation (in Radians) (Force specified in Newtons)

α/.Forces/.geometry1 /.geometry3/.geometry4//N//Simplify

$$\Rightarrow 0.264145F$$

The beam tip deflection in the x-direction, δx, is

δx = ($\partial_{\text{Fx}} U$) /.Md $\to$ 0//Simplify

$$\Rightarrow \frac{1}{4\text{EmodIzz}} R^3(-\text{Fy} + 2\text{Fx}\pi + 4\text{Fx}\beta + (3\text{Fy} - \text{Fx}(\pi + 2\beta))\text{Cos}[2\beta] - 4\text{FySin}[\beta] + 3\text{FxSin}[2\beta] + \text{Fy}\pi\text{Sin}[2\beta] + 2\text{Fy}\beta\text{Sin}[2\beta])$$

In specifying beam geometry $\{\beta \to \pi/4,\ \phi \to \pi/36\}$

δx/.Forces/.geometry1 //N//Simplify

$$\Rightarrow \frac{0.490872FR^3}{\text{EmodIzz}}$$

Assuming the geometry and material properties to be

$\left\{\text{Emod} \to 200 * 10^9, \text{Izz} \to \frac{\pi * d^4}{64}, d \to 0.0002, R \to 0.005\right\}$

results in the following rotation (in Radians) (Force specified in Newtons)

$\boldsymbol{\delta x/.Forces/.geometry1/.geometry3/.geometry4//N}$

$$\Rightarrow\ 0.00390624F$$

The beam tip deflection in the y-direction, δy, is

$\boldsymbol{\delta y = (\partial_{Fy} U)\ /.Md \to 0}$

$$\Rightarrow \frac{1}{8\text{EmodIzz}}\left(R\left(-2\text{Fx}R^2 + 4\text{Fy}\pi R^2 + 8\text{Fy}R^2\beta - 16\text{Fy}R^2\text{Cos}[\beta]\right.\right.$$
$$- R^2(-6\text{Fx} - 2\text{Fy}(\pi + 2\beta))\text{Cos}[2\beta] - 8\text{Fx}R^2\text{Sin}[\beta]$$
$$\left.\left.-6\text{Fy}R^2\text{Sin}[2\beta] + 2\text{Fx}\pi R^2\text{Sin}[2\beta] + 4\text{Fx}R^2\beta\text{Sin}[2\beta]\right)\right)$$

$\boldsymbol{\delta y/.Forces/.geometry1\ //N//Simplify}$

$$\Rightarrow \frac{0.210511FR^3}{\text{EmodIzz}}$$

Assuming the geometry and material properties to be

$$\left\{\text{Emod} \to 200 * 10^9, \text{Izz} \to \tfrac{\pi * d^4}{64}, d \to 0.0002, R \to 0.005\right\}$$

results in the following rotation (in Radians) (Force specified in Newtons)

$\boldsymbol{\delta y/.Forces/.geometry1/.geometry3/.geometry4//N}$

$$\Rightarrow\ 0.00167519F$$

To check this versus what's shown in Shigley & Mischke's Mechanical Engineering Design (5th Ed) p. 119, make $\beta = \pi/2$ and look at δy

$\boldsymbol{\text{geometry1:=}\{\beta \to \pi/2\}}$

$\boldsymbol{U = \frac{1}{2*\text{Izz}*\text{Emod}} \int_{-\frac{\pi}{2}}^{\beta} \left(\text{Mb}^2/.\text{moment}/.\text{geometry2}\ /.\text{geometry1}\right)}$
$\boldsymbol{Rd\theta/.Md \to 0\ /.Fx \to 0//Simplify}$

$$\Rightarrow \frac{\text{Fy}^2R^3(\pi + 2\beta + \text{Sin}[2\beta])}{8\text{EmodIzz}}$$

$\boldsymbol{\delta y = (\partial_{Fy} U)\ /.Fx \to 0/.geometry1//Simplify//N}$

$$\Rightarrow \frac{1.5708\text{Fy}R^3}{\text{EmodIzz}}$$

Which matches the formula given by Shigley & Mischke.

A.3 R_a and R_q Calculation

The linear roughness R_a was calculated by

$$R_a = \frac{1}{N}\sum_{i=1}^{N} abs(x[i] - \bar{x})$$

and RMS roughness R_q was calculated by

$$R_q = \sqrt{\sum_{i=1}^{N}(x[i] - \bar{x})^2},$$

where $x[i]$ is the height of point i in the profile, $\bar{x}$ is the average height of the profile, and N is the number of points in the profile.

A.4 Effects of varying stalk model parameters

Plots are shown varying the parameters of k_{ext}, k_θ, θ_0, and $\theta_{preload}$ so that their effects on the linkage characteristic can be observed.

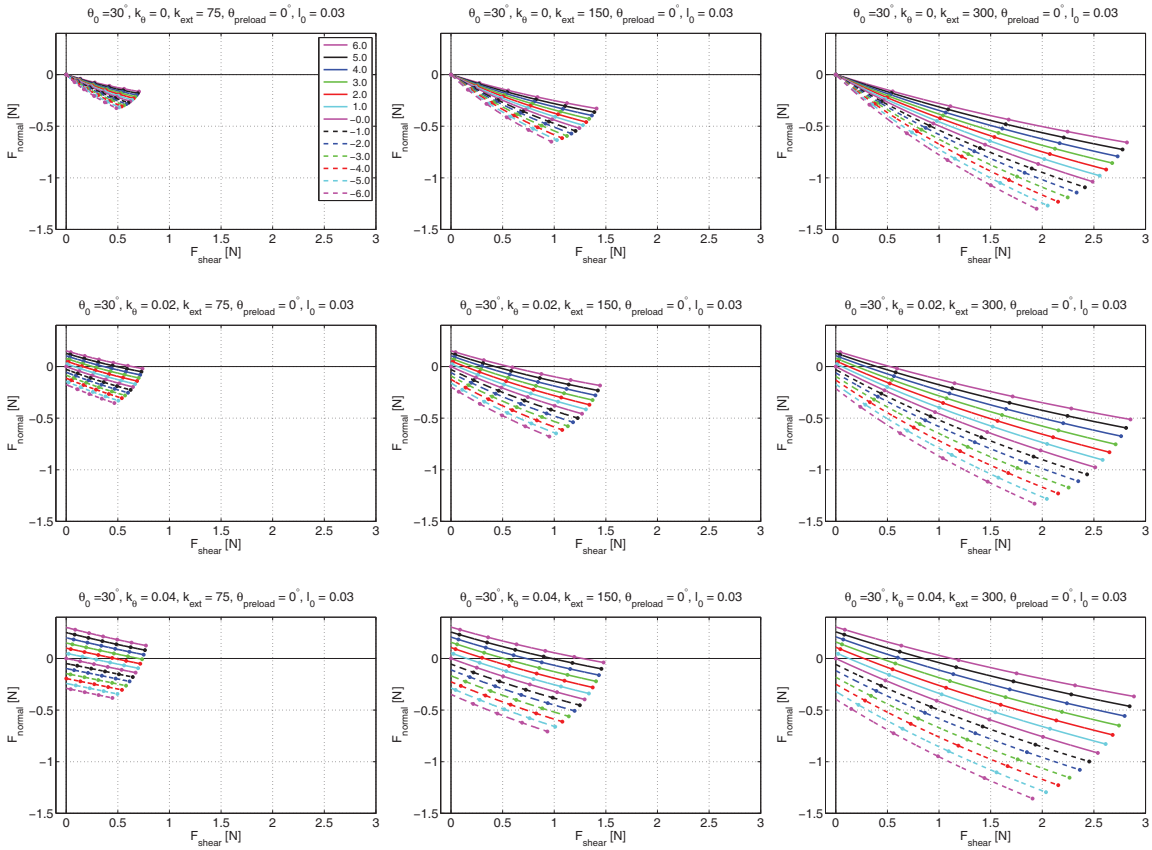

Figure A.2: Results of simulations using the stalk model and varying k_θ and k_{ext}. From top to bottom, the rows have $k_\theta = \{0, 0.02, 0.04\}$ [N m/radian]. From left to right, the columns have $k_{ext} = \{75, 150, 300\}$ [N m]. The stalk model was set to have an initial length l_0 of 3cm. Preloads from 6mm to -6mm were applied, (negative preloads, with dashed lines, showing the effects of adhesive loads), and the spine base was displaced 1cm down the surface.

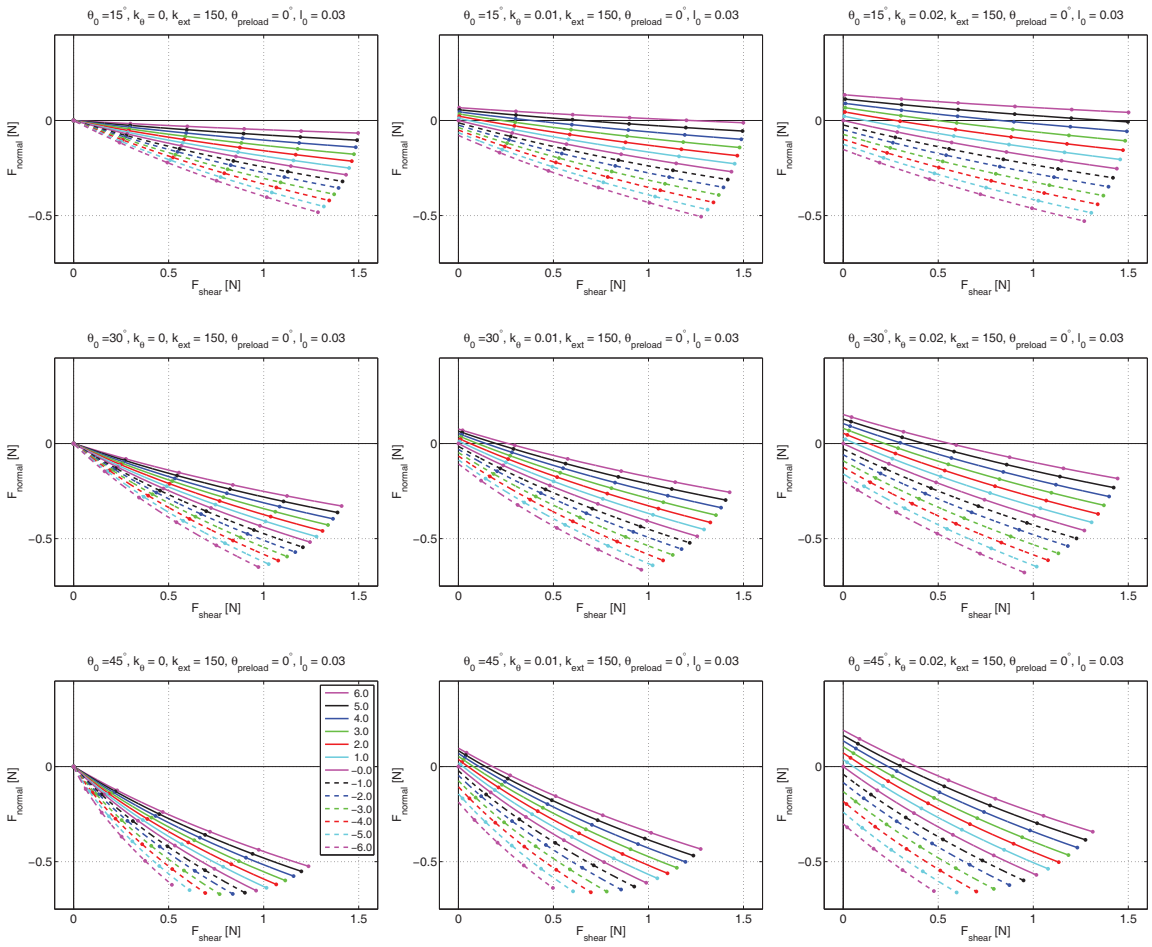

Figure A.3: Results of simulations using the stalk model and varying θ_0 and k_θ. From top to bottom, the rows have $\theta_0 = \{15°, 30°, 45°\}$. From left to right, the columns have $k_\theta = \{0, 0.01, 0.02\}$ [N m/radian]. The stalk model was set to have an initial length l_0 of 3cm. Preloads from 6mm to -6mm were applied, (negative preloads, with dashed lines, showing the effects of adhesive loads), and the spine base was displaced 1cm down the surface.

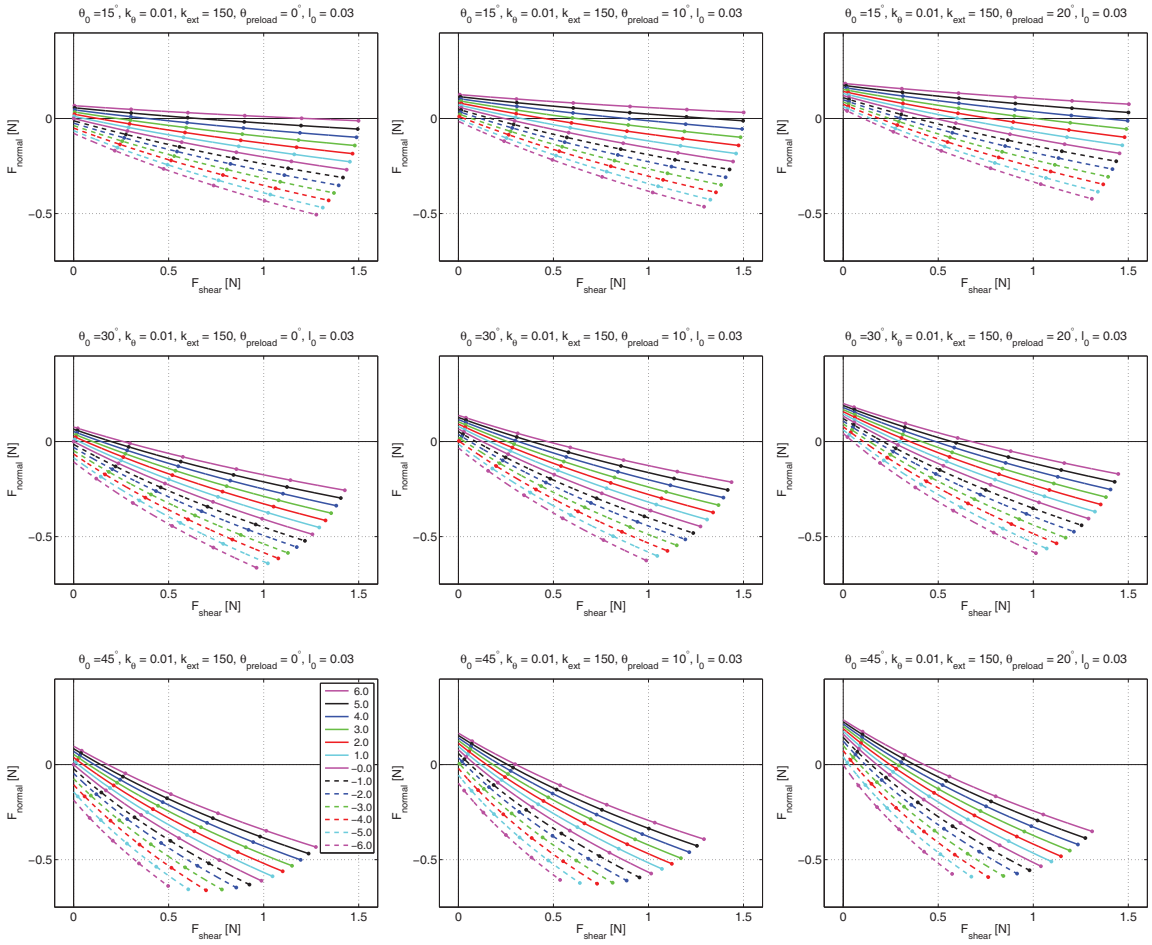

Figure A.4: Results of simulations using the stalk model and varying θ_0 and $\theta_{preload}$. From top to bottom, the rows have $\theta_0 = \{15°, 30°, 45°\}$. From left to right, the columns have $\theta_{preload} = \{0°, 10°, 20°\}$. The stalk model was set to have an initial length l_0 of 3cm. Preloads from 6mm to -6mm were applied, (negative preloads, with dashed lines, showing the effects of adhesive loads), and the spine base was displaced 1cm down the surface.

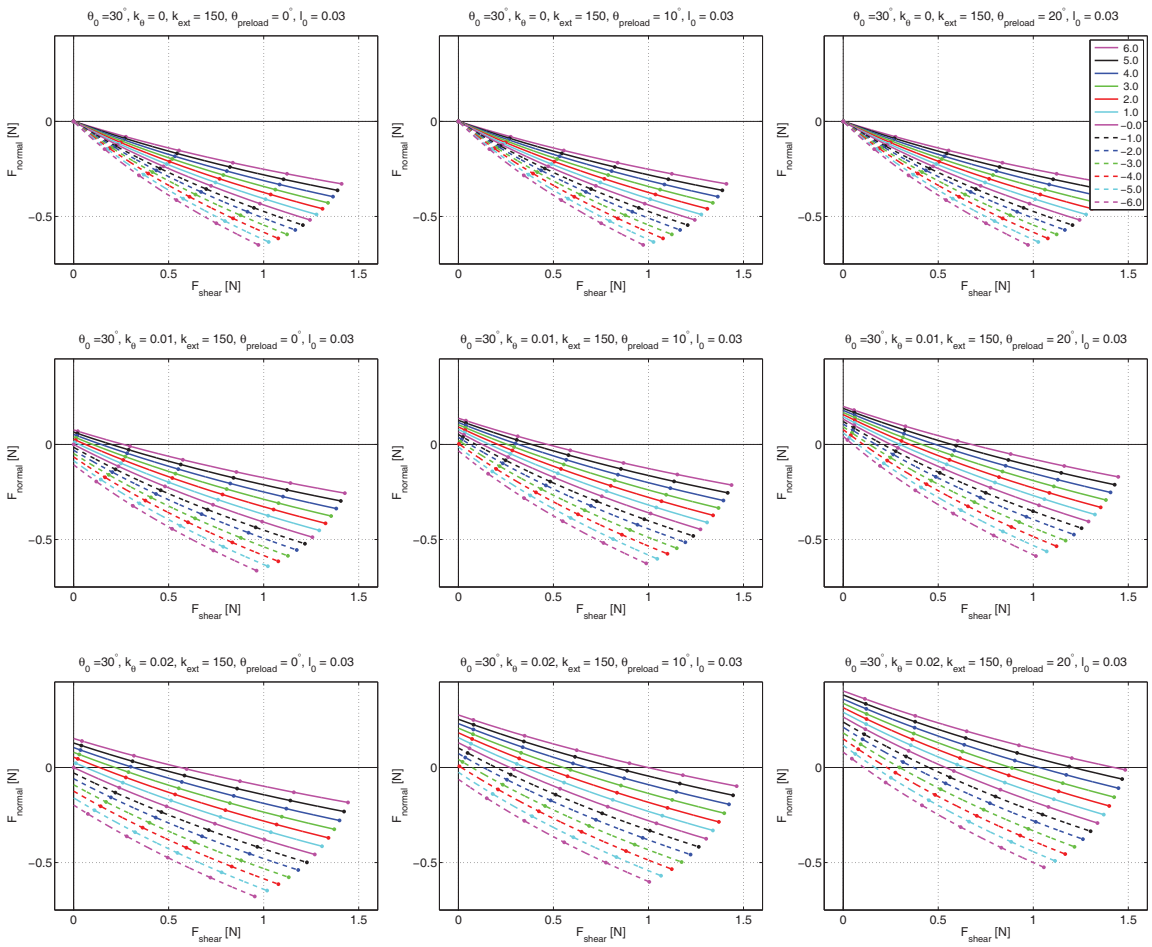

Figure A.5: Results of simulations using the stalk model and varying k_θ and $\theta_{preload}$. From top to bottom, the rows have $k_\theta = \{0, 0.01, 0.02\}$ [N m/radian]. From left to right, the columns have $\theta_{preload} = \{0°, 10°, 20°\}$. The stalk model was set to have an initial length l_0 of 3cm. Preloads from 6mm to -6mm were applied, (negative preloads, with dashed lines, showing the effects of adhesive loads), and the spine base was displaced 1cm down the surface.

Bibliography

[1] Eduard Arzt, Stanislav Gorb, and Ralph Spolenak. From micro to nano contacts in biological attachment devices. In *Proceedings of National Academy of Sciences*, volume 100, pages 10603–10606, 2003.

[2] Alan Asbeck, Sanjay Dastoor, Aaron Parness, Laurel Fullerton, Noe Esparza, Daniel Soto, Barrett Heyneman, and Mark Cutkosky. Climbing rough vertical surfaces with hierarchical directional adhesion. *IEEE ICRA*, pages 1–6, Mar 2009.

[3] Alan Asbeck, Sangbae Kim, M.R Cutkosky, William R Provancher, and Michele Lanzetta. Scaling hard vertical surfaces with compliant microspine arrays. *International Journal of Robotics Research*, 25(12):14, Sep 2006.

[4] A.T. Asbeck, S. Kim, W.R. Provancher, M.R. Cutkosky, and M. Lanzetta. Scaling hard vertical surfaces with compliant microspine arrays. In *Proceedings, Robotics: Science and Systems Conference*. Boston, MA, June 2005.

[5] K Autumn. Properties, principles, and parameters of the gecko adhesive system. pages 225–256. 2006.

[6] K Autumn, A Dittmore, D Santos, M Spenko, and M Cutkosky. Frictional adhesion: a new angle on gecko attachment. *Journal of Experimental Biology*, 209(18):3569–3579, 2006.

[7] K Autumn, Y A Liang, S T Hsieh, W Zesch, W P Chan, T W Kenny, R Fearing, and R J Full. Adhesive force of a single gecko foot-hair. *Nature*, 405(6787):681–5, 2000.

[8] K. Autumn, Y.A. Liang, S.T. Hsieh, W. Zesch, W.P. Chan, T. Kenny, F. Fearing, and R.J. Full. Adhesive force of a single gecko foot-hair. *Nature*, 405(6787):681–685, June 2000.

[9] K. Autumn and A. Peattie. Mechanisms of adhesion in geckos. *Integrative and Comparative Biology*, 42(6):1081–1090, 2002.

[10] Kellar Autumn, Metin Sitti, Yiching A Liang, Anne M Peattie, Wendy R Hansen, Simon Sponberg, Thomas W Kenny, Ronald Fearing, Jacob N Israelachvili, and Robert J Full. Evidence for van der waals adhesion in gecko setae. *Proc Natl Acad Sci USA*, 99(19):12252–6, 2002.

[11] C. Balaguer, A. Gimenez, J.M. Pastor, V.M. Padron, and C. Abderrahim. A climbing autonomous robot for inspection applications in 3d complex environments. *Robotica*, 18:287–297, 2000.

[12] D. Bevly, S. Dubowsky, and C. Mavroidis. A simplified cartesian-computed torque controller for highly geared systems and its application to an experimental climbing robot. *Transactions of the ASME. Journal of Dynamic Systems, Measurement and Control*, 122(1):27–32, 2000.

[13] WJ Bock and WD Miller. The scansorial foot of the woodpeckers, with comments on the evolution of perching and climbing feet in birds. *Amer. Mus. Novitates*, 1931:1–45, 1959.

[14] T. Bretl, S. Rock, and J.C. Latombe. Motion planning for a three-limbed climbing robot in vertical natural terrain. In *Proceedings of the IEEE International Conference on Robotics and Automation*, volume 205, pages 2946 – 2953. Piscataway, NJ, USA : IEEE, 2003.

[15] M. Catmill. Climbing. In M. Hildebrand, D.M. Bramble, K.F. Liem, and D.B. Wake, editors, *Functional Vertebrate Morphology*, pages 73–88. The Belknap Press, Cambridge, 1985.

[16] J. G. Cham, S. A. Bailey, J. E. Clark, R. J. Full, and M. R. Cutkosky. Fast and robust: Hexapedal robots via shape deposition manufacturing. *The International Journal of Robotics Research*, 21(10):869–882, 2002.

[17] M. A. Costa and M. R. Cutkosky. Roughness perception of haptically displayed fractal surfaces. In *Proceedings of the ASME Dynamic Systems and Control Division*, volume 69-2, pages 1073–1079, 2000.

[18] MR Cutkosky and I. Kao. Computing and controlling compliance of a robotic hand. *IEEE Transactions on Robotics and Automation*, 5(2):151–165, 1989.

[19] Z.D. Dai, S.N. Gorb, and U. Schwarz. Roughness-dependent friction force of the tarsal claw system in the beetle *Pachnoda marginata* (coleoptera, scarabaeidae). *Journal Of Experimental Biology*, 205(16):2479–2488, 2002.

[20] K Daltorio, S Gorb, A Peressadko, A Horchler, R Ritzmann, and R Quinn. A robot that climbs walls using micro-structured polymer feet. pages 131–138, 2005.

[21] K.A. Daltorio, S. Gorb, A. Peressadko, A.D. Horchler, R.E. Ritzmann, and R.D. Quinn. A robot that climbs walls using micro-structured polymer feet. In *International Conference on Climbing and Walking Robots (CLAWAR)*, pages 131–138, 2005.

[22] K.A. Daltorio, A.D. Horchler, S. Gorb, R.E. Ritzmann, and R.D. Quinn. A small wall-walking robot with compliant, adhesive feet. In *Int. Conf. on Intelligent Robots and Systems (IROS)*, pages 4018–4023, 2005.

[23] K.A Daltorio, A.D Horchler, S Gorb, R.E Ritzmann, and R.D Quinn. A small wall-walking robot with compliant, adhesive feet. *Proceedings IEEE IRS*, 2005.

[24] Kathryn A. Daltorio, Terence E. Wei, Andrew D. Horchler, Lori Southard, Gregory D. Wile, Roger D. Quinn, Stanislav N. Gorb, and Roy E. Ritzmann. Mini-Whegs TM Climbs Steep Surfaces Using Insect-inspired Attachment Mechanisms. *The International Journal of Robotics Research*, 28(2):285–302, 2009.

[25] W. D'Arcy Thompson. On growth and form. *Cambridge University Press, Cambridge*, 1942.

[26] B. Earl. Going squirrelly? *Pest Control Technology Magazine*, Sept. 2007.

[27] S.B. Emerson and D. Diehl. Toe pad morphology and mechanisms of sticking in frogs. *Biological Journal of the Linnean Society*, 13(3):199–216, 1980.

[28] W. Federle, M. Riehle, A.S.G. Curtis, and R.J. Full. An integrative study of insect adhesion: mechanics and wet adhesion of pretarsal pads in ants. *Integrative and Comparative Biology*, 42(6):1100–1106, 2002.

[29] SF Frazier, GS Larsen, D. Neff, L. Quimby, M. Carney, RA DiCaprio, and SN Zill. Elasticity and movements of the cockroach tarsus in walking. *Journal of Comparative Physiology A: Neuroethology, Sensory, Neural, and Behavioral Physiology*, 185(2):157–172, 1999.

[30] Yasuhiro Fukuoka, Hiroshi Kimura, and Avis H. Cohen. Adaptive dynamic walking of a quadruped robot on irregular terrain based on biological concepts. *Int. Journal of Robotics Research*, 22(3-4):187–202, 2003.

[31] Liehui Ge, Sunny Sethi, Lijie Ci, Pulickel M Ajayan, and Ali Dhinojwala. Carbon nanotube-based synthetic gecko tapes. *Proc Natl Acad Sci USA*, 104(26):10792–5, 2007.

[32] A. K Geim, S. V Dubonos, I. V Grigorieva, K. S Novoselov, A. A Zhukov, and S. Yu Shapoval. Microfabricated adhesive mimicking gecko foot-hair. *Nat Mater*, 2(7):461–463, 2003.

[33] S Gorb, M Varenberg, A Peressadko, and J Tuma. Biomimetic mushroom-shaped fibrillar adhesive microstructure. *Journal of The Royal Society Interface*, 4(13):271–275, Oct 2006.

[34] S.N. Gorb, R.G. Beutel, E.V. Gorb, Y. Jiao, V. Kastner, S. Niederegger, V.L. Popov, M. Scherge, U. Schwarz, and W. Votsch. Structural design and biomechanics of friction-based releasable attachment devices in insects. *Integrative and Comparative Biology*, 42(6):1127, 2002.

[35] N Gravish, M Wilkinson, S Sponberg, A Parness, N Esparza, D Soto, T Yamaguchi, M Broide, M Cutkosky, C Creton, and K Autumn. Rate-dependent frictional adhesion in natural and synthetic gecko setae. *Journal of The Royal Society Interface*, Jan 2009.

[36] Nick Gravish, Matt Wilkinson, and Kellar Autumn. Frictional and elastic energy in gecko adhesive detachment. *Journal of The Royal Society Interface*, 5(20):339–348, 2007.

[37] J. A. Greenwood. Contact of rough surfaces. In I. L. Singer and H. M. Pollock, editors, *Fundamental of Friction: Macroscopic and Microscopic Processes*, pages 37–56. Kluwer Academic Publishers, Dordrecht, The Netherlands, 1992.

[38] J. A. Greenwood. Problem with surface roughness. In I. L. Singer and H. M. Pollock, editors, *Fundamental of Friction: Macroscopic and Microscopic Processes*, page 5776. Kluwer Academic Publishers, Dordrecht, The Netherlands, 1992.

[39] J. Grieco, M. Prieto, M. Armada, and P. Gonzalez de Santos. A six-legged climbing robot for high payloads. *Control Applications*, Jan 1998.

[40] L Guo, K Rogers, and R Kirkham. A climbing robot with continuous motion. *1994 IEEE International Conference on Robotics and Automation*, Jan 1994.

[41] WR Hansen and K Autumn. Evidence for self-cleaning in gecko setae. *Proceedings of the National Academy of Sciences*, 102(2):385–389, 2005.

[42] G.C. Haynes, A. Khripin, G. Lynch, J. Amory, A. Saunders, A.A. Rizzi, and D.E. Koditschek. Rapid Pole Climbing with a Quadrupedal Robot. *Departmental Papers (ESE)*, page 479, 2009.

[43] S Hirose and H Tsutsumitake. Disk rover: A wall-climbing robot using permanent. *Intelligent Robots and Systems*, Jan 1992.

[44] G Huber, H Mantz, R Spolenak, K Mecke, and K Jacobs. Evidence for capillarity contributions to gecko adhesion from single spatula nanomechanical measurements. *Proceedings of the National Academy of Sciences*, 2005.

[45] S Jensen-Segal, S Virost, and W Provancher. Rocr: Dynamic vertical wall climbing with a pendular two-link mass-shifting robot. *Robotics and Automation*, Jan 2008.

[46] H Jeong, S Lee, P Kim, and K Suh. Stretched polymer nanohairs by nanodrawing. *Nano Lett*, 2006.

[47] Hoon Eui Jeong, Jin-Kwan Lee, Hong Nam Kim, Sang Heup Moon, and Kahp Y Suh. A nontransferring dry adhesive with hierarchical polymer nanohairs. *Proc Natl Acad Sci USA*, 106(14):5639–44, 2009.

[48] K.L. Johnson. In *Contact Mechanics*, pages 72–94. Cambridge University Press, 1985.

[49] KL Johnson, K Kendall, and AD Roberts. Surface energy and the contact of elastic solids. *Proc. R. Soc. Lond. A.*, 324(1558):301–313, 1971.

[50] L.P. Kalra and J. Gu. An autonomous self contained wall climbing robot for non-destructive inspection of above-ground storage tanks. *Industrial Robot: An International Journal*, 34(2):122–7, 2007.

[51] I. Kao, MR Cutkosky, and RS Johansson. Robotic stiffness control and calibration as applied to humangrasping tasks. *IEEE Transactions on Robotics and Automation*, 13(4):557–566, 1997.

[52] K Kendall. Thin-film peeling - elastic term. *J Phys D Appl Phys*, 8(13):1449–1452, 1975.

[53] A. B. Kesel, A. Martin, and T. Seidl. Adhesion measurements on the attachment devices of the jumping spider evarcha arcuata. *The Journal of Experimental Biology*, 206:2733–2738, 2003.

[54] S Kim, M Spenko, S Trujillo, B Heyneman, V Mattoli, and M.R Cutkosky. Whole body adhesion: hierarchical, directional and distributed control of adhesive forces for a climbing robot. *Robotics and Automation, 2007 IEEE International Conference on*, pages 1268–1273, 2007.

[55] Sangbae Kim, Alan Asbeck, Mark Cutkosky, and William Provancher. SpinybotII: climbing hard walls with compliant microspines. *Advanced Robotics, 2005. ICAR '05. Proceedings., 12th International Conference on*, pages 601 – 606, Jun 2005.

[56] Sangbae Kim, M Spenko, S Trujillo, B Heyneman, D Santos, and M Cutkosky. Smooth vertical surface climbing with directional adhesion. *Robotics, IEEE Transactions on*, 24(1):65 – 74, 2008.

[57] Seok Kim and Metin Sitti. Biologically inspired polymer microfibers with spatulate tips as repeatable fibrillar adhesives. *Appl. Phys. Lett.*, 89(26):261911, 2006.

[58] J. Kövecses and J. Angeles. The stiffness matrix in elastically articulated rigid-body systems. *Multibody System Dynamics*, 18(2):169–184, 2007.

[59] G. La Rosa, M. Messina, G. Muscato, and R. Sinatra. A low-cost lightweight climbing robot for the inspection of vertical surfaces. *Mechatronics*, 12(1):71–96, 2002.

[60] R. Lal Tummala, R. Mukherjee, N. Xi, D. Aslam, H. Dulimarta, Jizhong Xiao, M. Minor, and G. Dang. Climbing the walls [robots]. *IEEE Robotics and Automation Magazine*, 9(4):10–19, 2002.

[61] G.S. Larsen, S.F. Frazier, and S.N. Zill. The tarso-pretarsal chordotonal organ as an element in cockroach walking. *Journal of Comparative Physiology A: Neuroethology, Sensory, Neural, and Behavioral Physiology*, 180(6):683–700, 1997.

[62] J Lee, B Bush, R Maboudian, R Fearing, and 2009. Gecko-inspired combined lamellar and nanofibrillar array for adhesion on nonplanar surface. *LANGMUIR*, 25(21):12449–12453, 2009.

[63] J Lee, R Fearing, and K Komvopoulos. Directional adhesion of gecko-inspired angled microfiber arrays. *Applied Physics Letters*, 2008.

[64] J. Loncaric. Normal forms of stiffness and compliance matrices. *Robotics and Automation, IEEE Journal of [legacy, pre-1988]*, 3(6):567–572, 1987.

[65] L.W. Macior. Insect adaptation and behavior in Asclepias pollination. *Bulletin of the Torrey Botanical Club*, 92(2):114–126, 1965.

[66] B.C. Mahendra. Contributions to the bionomics, anatomy, reproduction and development of the Indian house-gecko, *Hemidactylus flaviviridis* rüppel. Part II. The problem of locomotion. *Proceedings: Plant Sciences*, 13(5):288–306, 1941.

[67] C Majidi, R. E Groff, Y Maeno, B Schubert, S Baek, B Bush, R Maboudian, N Gravish, M Wilkinson, K Autumn, and R. S Fearing. High friction from a stiff polymer using microfiber arrays. *Phys. Rev. Lett.*, 97(7):4, 2006.

[68] A. Majumdar and B. Bhushan. Role of fractal geometry in roughness characterization and contact mechanics of surfaces. *Journal of Tribology*, 112:205, 1990.

[69] C. Mattheck and S. Reuss. The claw of the tiger: An assessment of its mechanical shape optimization. *Journal of Theoretical Biology*, 150(3):323–328, 1991.

[70] C. Menon, M. Murphy, and M. Sitti. Gecko inspired surface climbing robots. Proceedings of the IEEE International Conference on Robotics and Biomimetics (ROBIO), 2004.

[71] A. W. Momber. Damage to rocks and cementitious materials from solid impact. *Rock Mechanics and Rock Engineering*, 37(1):57–82, 2004.

[72] M Murphy, S Kim, and M Sitti. Enhanced adhesion by gecko-inspired hierarchical fibrillar adhesives. *ACS Applied Materials & Interfaces*, 1(4):849–855, 2009.

[73] M. Murphy and M. Sitti. Waalbot: an agile small-scale wall climbing robot utilizing pressure sensitive adhesives. *IEEE/ASME Trans. on Mechatronics*, 12(3):330–338, 2007.

[74] M.P Murphy, B Aksak, and M Sitti. Adhesion and anisotropic friction enhancements of angled heterogeneous micro-fiber arrays with spherical and spatular tips. *J. Adhesion Sci. Technol*, 21(12-13):1281–1296, 2007.

[75] W. Nachtigall. *Biological mechanisms of attachment*. Springer Berlin, 1974.

[76] P Niewiarowski, S Lopez, L Ge, and E Hagan. Sticky gecko feet: The role of temperature and humidity. *PLoS ONE*, 2008.

[77] Michael T Northen and Kimberly L Turner. A batch fabricated biomimetic dry adhesive. *Nanotechnology*, 16(8):1159–1166, May 2005.

[78] N. E. Odling. Natural fracture profiles, fractal dimension and joint roughness coefficients. *Rock Mechanics and Rock Engineering*, 27(3):135–153, 1994.

[79] A.M. Okamura and M.R. Cutkosky. Feature detection for haptic exploration with robotic fingers. *The International Journal of Robotics Research*, 20(12):925, 2001.

[80] A Parness, D Soto, N Esparza, N Gravish, M Wilkinson, K Autumn, and M Cutkosky. A microfabricated wedge-shaped adhesive array displaying gecko-like dynamic adhesion, directionality and long lifetime. *Journal of the Royal Society, Interface*, Mar 2009.

[81] Aaron Parness. Micro-structured adhesives for climbing applications. *Stanford PhD Thesis*, pages 1–148, January 2010.

[82] W.L. Power and T.E. Tullis. Euclidean and fractal models for the description of rock surface roughness. *Journal of Geophysical Research*, 96(B1), 1991.

[83] H Prahlad, R Pelrine, S Stanford, and J Marlow. Electroadhesive robots—wall climbing robots enabled by a novel, robust, and electrically controllable adhesion technology. *IEEE Robotics and Automation*, 2008.

[84] L Qu, L Dai, M Stone, Z Xia, and Z Wang. Carbon nanotube arrays with strong shear binding-on and easy normal lifting-off. *Science*, 2008.

[85] R. D. Quinn, G.M. Nelson, R.J. Bachmann, D.A. Kingsley, J. Offi, and R. E. Ritzmann. Insect designs for improved robot mobility. In *Proc. of Climbing and Walking Robots Conference (CLAWAR01)*, pages 69–76. Berns and Dillmann eds., Prof. Eng., 2001.

[86] N.W Rizzo, K.H Gardner, D.J Walls, N.M Keiper-Hrynko, T.S Ganzke, and D.L Hallahan. Characterization of the structure and composition of gecko adhesive setae. *Journal of The Royal Society Interface*, 3(8):441–451, 2005.

[87] L.L. Rogers and E.L. Lindquist. Supercanopy white pine and wildlife. In *White Pine Symposium Proceedings*, 1992.

[88] J.R. Rossignac and A.A.G. Requicha. Offsetting operations in solid modelling. *Computer Aided Geometric Design*, 3:129–148, 1986.

[89] L.M. Roth and E.R. Willis. Tarsal structure and climbing ability of cockroaches. *J. Exp. Zool*, 119:483–517, 1952.

[90] D Santos, S Kim, M Spenko, A Parness, and M Cutkosky. Directional adhesive structures for controlled climbing on smooth vertical surfaces. *IEEE ICRA*, 2007.

[91] Daniel Santos, Matthew Spenko, Aaron Parness, Sangbae Kim, and Mark Cutkosky. Directional adhesion for climbing: theoretical and practical considerations. *Journal of Adhesion Science and Technology*, 21(12-13):1317–1341, 2007.

[92] U. Saranli, M. Buehler, and D.E. Koditschek. Rhex: A simple and highly mobile hexapod robot. *Int. Journal of Robotics Research*, 20:616–631, 2001.

[93] Bryan Schubert, Jongho Lee, Carmel Majidi, and Ronald S Fearing. Sliding-induced adhesion of stiff polymer microfibre arrays. ii. microscale behaviour. *Journal of The Royal Society Interface*, 5(25):845–853, 2008.

[94] G.L. Sheldon and I. Finnie. The mechanism of material removal in the erosive cutting of brittle materials. *ASME Journal of Engineering for Industry*, 88B:393–400, 1966.

[95] W Shen, J Gu, and Y Shen. Permanent magnetic system design for the wall-climbing robot. *Applied Bionics and Biomechanics*, Jan 2006.

[96] C.R. Shigley, J.E.; Mischke. In *Standard Handbook of Machine Design (2nd Edition)*. McGraw-Hill, 1996.

[97] Smooth-On. Vytaflex series liquid urethane rubbers technical bulletin. 2010.

[98] JC Spagna, DI Goldman, PC Lin, DE Koditschek, and RJ Full. Distributed mechanical feedback in arthropods and robots simplifies control of rapid running on challenging terrain. *Bioinspiration and Biomimetics*, 2(1):9, 2007.

[99] M.J Spenko, G.C Haynes, J.A Saunders, M.R Cutkosky, A.A Rizzi, and R.J Full. Biologically inspired climbing with a hexapedal robot. *Journal of Field Robotics*, Feb 2008.

[100] MJ Spenko, GC Haynes, JA Saunders, MR Cutkosky, A.A. Rizzi, RJ Full, and DE Koditschek. Biologically inspired climbing with a hexapedal robot. *Journal of Field Robotics*, 25(4):223–242, 2008.

[101] W Sun, P Neuzil, T Kustandi, and S Oh. The nature of the gecko lizard adhesive force. *Biophysical journal*, 2005.

[102] O Unver and M Sitti. A miniature ceiling walking robot with flat tacky elastomeric footpads. *IEEE ICRA*, pages 1–6, Mar 2009.

[103] O Unver and M Sitti. Tankbot: A miniature, peeling based climber on rough and smooth surfaces. *IEEE ICRA*, pages 1–6, Mar 2009.

[104] Vortex VRAM. http://www.vortexhc.com/vmrp.html. 2006.

[105] Inc. Wolfram Research. Mathematica edition: Version 7.0. 2008.

[106] J Xiao, W Morris, N Chakravarthy, and A Calle. City climber: a new generation of mobile robot with wall-climbing capability. *Proceedings of SPIE*, Jan 2006.

[107] J Xiao and A Sadegh. City-climber: A new generation wall-climbing robots. *ars.i-techonline.com*, 2007.

[108] Z Xu and P Ma. A wall-climbing robot for labelling scale of oil tank's volume. *Robotica*, Jan 2002.

[109] Z.L. Xu and P.S. Ma. A wall-climbing robot for labelling scale of oil tank's volume. *Robotica*, 20:209–212, 2002.

[110] E Yoon, R Singh, H Kong, B Kim, D Kim, and H Jeong K Suh. Tribological properties of bio-mimetic nano-patterned polymeric surfaces on silicon wafer. *Tribology Letters*, 2006.

[111] P.A. Zani. The comparative evolution of lizard claw and toe morphology and clinging performance. *Journal of Evolutionary Biology*, 13:316–325, 2000.

[112] Y Zhao, T Tong, L Delzeit, A Kashani, and M Meyyappan. Interfacial energy and strength of multiwalled-carbon-nanotube-based dry adhesive. *Journal of Vacuum Science & Technology B: Microelectronics*, Jan 2006.

[113] J. Zhu, D. Sun, and S.K. Tso. Development of a tracked climbing robot. *Journal Of Intelligent And Robotic Systems*, 35(4):427–444, 2002.